# Solar Energy-Driven Photothermal Catalytic $CO_2$ Hydrogenation over Nanometals/Oxides Catalysts

（ナノ金属/酸化物触媒を用いた光誘起熱触媒反応による二酸化炭素の水素化に関する研究）

Bowen Deng

*Graduate School of Chemical Sciences and Engineering*

*Hokkaido University*

*2023*

# Contents

# Abstract

Solar energy driven photothermal catalytic $CO_2$ hydrogenation to valuable fuels and chemicals is a promising technology to alleviate the gradually deteriorative environment and energy problems simultaneously. Cu- or $In_2O_3$-based catalysts, featuring good catalytic activity for $CO_2$ conversion and low price, are considered as promising candidates for photothermal catalytic $CO_2$ hydrogenation. With the plausible design of the nanostructures, catalysts can exhibit a remarkable performance via the synergetic effects of light-to-heat conversion and photo-induced hot charge-carrier-mediated activation of the reactants. However, although many efforts have been taken to investigate the photothermal catalysis over the past few years, it still remains challenging to develop catalysts with high efficiency, good stability and desired product selectivity for photothermal $CO_2$ hydrogenation, and also to clarify the mechanism of photo-driven $CO_2$ conversion and illustrate the influence of metal-support interaction on the process. Thus, this thesis focuses on the rational design of Cu-based and $In_2O_3$-based catalysts for efficient and stable photothermal catalytic $CO_2$ hydrogenation at mild conditions by coupling solar heating effect and photo-induced activation of the reactants via hot carriers, as well as selectively generating highly valuable solar methanol under ambient pressure.

In chapter 1, a general background about photothermal $CO_2$ hydrogenation reaction and the fundamentals of photothermal processes are introduced. Then, the recent development of $CO_2$ conversion reaction driven or promoted by solar energy is summarized.

In chapter 2, a Ga-Cu/$CeO_2$ catalyst was synthesized by direct pyrolysis of the Ga and Cu-containing Ce-metal-organic frameworks for efficient photothermal catalytic $CO_2$ hydrogenation to CO via RWGS reaction. Due to the highly dispersed Ga and Cu species in $CeO_2$, the optimized catalyst 10Cu5Ga/$CeO_2$ (10 wt% Cu and 5 wt% Ga) achieved a CO production rate of 111.2 $mmol \cdot g^{-1} \cdot h^{-1}$ with nearly 100% selectivity under full solar spectrum irradiation, which is superior to most reported Cu and other earth-

abundant metals-based photothermal catalysts. Mechanism studies demonstrated that the synergy of photothermal heating and light-promotion contributed to the substantially increased CO production. In situ DRIFTS results revealed that the introduction of Ga enhanced the formation of formate species, the key intermediates in $CO_2$ hydrogenation, and light-induced hot carriers facilitated the decomposition of formate species to carbonyl, thus enhancing CO production.

In chapter 3, to enhance the long-term stability of catalysts in the photothermal catalysis, which is an important factor for further application, a joint strategy was utilized to fabricate an efficient metal-oxide ($ZrO_2$) modified Cu/MgO-$Al_2O_3$ photothermal catalyst via the pyrolysis of LDH precursors followed by the loading of $ZrO_2$. Due to the highly dispersed Cu and the stabilization by the addition of metal oxide ($ZrO_2$), the modified catalysts exhibited not only efficient activity of CO production but also remarkably improved long-term stability. After 12 h reaction process, the CO yield was still remaining 93% as that on fresh catalyst. Detailed study suggested that the addition of metal oxide stabilized the architecture of Cu nanoparticles and prevented the aggregation of active Cu, thus preserving the active sites of catalysts during the reaction process.

In chapter 4, in order to achieve efficient solar methanol ($CH_3OH$) production, a much more valuable product than CO, a Ru/$In_2O_3$ catalyst was synthesized by a facile method for effective photothermal methanol production from $CO_2$ hydrogenation under atmosphere pressure. With the light irradiation, the Ru/$In_2O_3$ catalyst could effectively catalyze methanol synthesis and achieved a remarkable and stable solar methanol production of 280.4 μmol $g^{-1}$ $h^{-1}$, which was ~50 times higher than that of $In_2O_3$ under the same conditions and surpassed by far reported $In_2O_3$-based photothermal catalysts. Detailed studies demonstrated that Ru modulated the electronic structure of $In_2O_3$ and promoted the formation of oxygen vacancies ($V_o$). The synergy of photothermal heating effect and hot-carriers-induced reactants activation on Ru together with the interaction between Ru and $In_2O_3$ enhanced the conversion of $CO_2$ and $H_2$ on the catalyst surface, thereby contributing to the efficient solar methanol production.

In chapter 5, an overall summary of this dissertation was presented. This thesis carried out a systematic study on photothermal catalytic $CO_2$ hydrogenation over Cu-based and $In_2O_3$-based catalysts, including photothermal RWGS reaction and solar methanol production under atmosphere pressure. Highly efficient $CO_2$ conversion to CO and lower apparent activation energy were achieved in photothermal catalysis over Cu-based catalysts with the coupling of solar heating and light-induced hot carrier-mediated activation of reactants, and the modulation of catalysts succeeded in an excellent stability. In atmosphere pressure, solar methanol was considerably generated with the assistance of hot carriers and the interaction between Ru and $In_2O_3$. The findings in this study strengthened the understanding of the interaction between light-induced hot carriers and surface reactants, and provided a potential strategy for realizing efficient and stable $CO_2$ hydrogenation with desired product selectivity for industrial application through the rational design of Cu-based and $In_2O_3$-based catalysts.

# Chapter 1 Introduction

## 1.1 General introduction of photothermal catalytic $CO_2$ conversion

Carbon dioxide ($CO_2$), an important component of the atmosphere, plays a key role in the natural carbon cycle.[1, 2] On one hand, it is the terminal of variable activities to obtain energy from carbon species, including respiration and burning of fuels. On the other hand, $CO_2$ is the feedstock for photosynthesis, which converts enormous solar energy into chemical energy and establishes the foundation of the earth ecology. Due to the greenhouse effect of $CO_2$, its concentration in the atmosphere shows a great influence on global climate.[3-5] Nowadays, with the development of modern society, $CO_2$ emission has quickly increased. According to International Energy Agency, the global $CO_2$ emission in 2021 reached a record high amount of 36.3 Gt, increased almost by 60% than that in 1990 (20.5 Gt) (Figure 1.1a).[6] As a result, the $CO_2$ concentration is gradually increasing over the last century, and has exceeded 415 ppm in 2022, roughly 25% above the average level in the 1980s (Figure 1.1b).[7] This aggravates global climate problems, such as global warming and subsequent extreme weather. As the worldwide energy consumption still mainly relies on fossil fuels, it is expected that $CO_2$ concentration will continuously ascend to ~550 ppm by 2050 if no measures are adopted.[8] Therefore, it is urgent to develop efficient technologies to control the $CO_2$ amount in atmosphere.[9, 10]

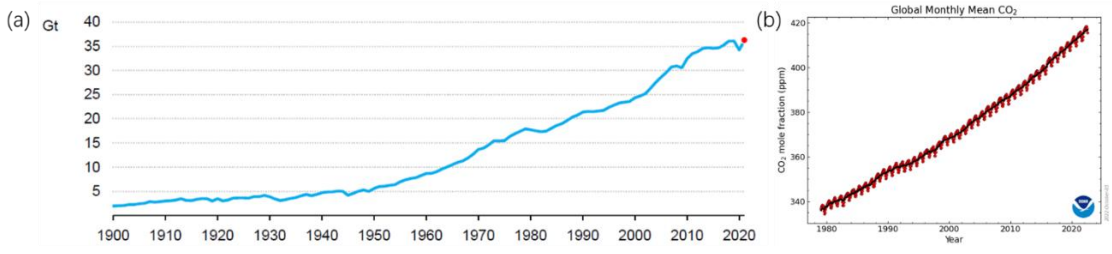


**Figure 1.1** (a) Worldwide annual $CO_2$ emission with history data during 1900 – 2021.[6] (b) Atmospheric $CO_2$ concentration during 1960 – 2022.[7]

In general, the strategies to reduce $CO_2$ amount in the atmosphere could be summarized as Carbon Capture, Utilization and Storage (CCUS), suggesting two

different parallel directions, utilization and storage of $CO_2$.[11-14] Recently, the technical state-of-the-art of carbon capture and storage (CCS) by geologic storage process has been discussed by some comprehensive reviews, which seems to be a potential method but still faces some challenges in the meantime, such as high costs for capture and separation of $CO_2$, low efficiency of capture and sequestration of $CO_2$, and the long-term reliability of underground storage.[15-18] Meanwhile, the utilization of $CO_2$ is also a promising route, since it could not only reduce the $CO_2$ concentration in atmosphere, but also produce value-added fuels or chemicals for industrial application.[11, 19, 20] Nowadays, many efforts have been taken to develop the possible routines for utilization of $CO_2$, and Figure 1.2 demonstrates the potential technologies for $CO_2$ conversion.[3, 21] From this perspective, $CO_2$ is considered as an industrial feedstock instead of waste gas, similar to its role in natural photosynthesis, and the reuse of $CO_2$ could help accomplish the global carbon cycle and realize the sustainable society in the future.[22]

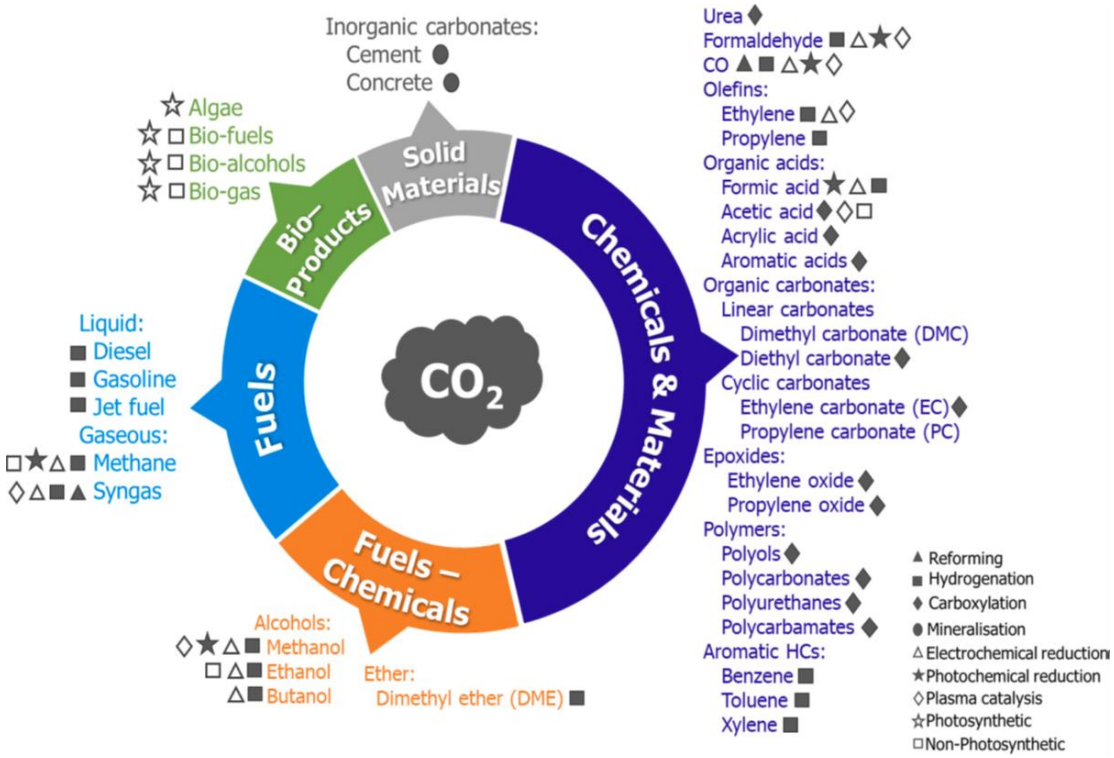


**Figure 1.2** Possible technologies and products for $CO_2$ utilization.[21]

$CO_2$ is a thermodynamically stable molecule because of the structure, whose symmetrical line configuration composed of two strong C=O bonds (799 $kJ \cdot mol^{-1}$)

implies the difficulty to activate and decompose the $CO_2$ without the assistance of immense input energy.[23] In order to obtain a competitive conversion efficiency of $CO_2$, high temperatures as well as high pressures are widely applied in the catalytic $CO_2$ conversion reactions, especially the traditional thermal catalytic processes, which results in the excess energy consumption and carbon dioxide emission.[24] Therefore, alternative and sustainable technologies to efficiently convert $CO_2$ under mild conditions should be developed to simultaneously alleviate the energy shortage and environmental issues.

Up till now, various technologies have been reported to realize the conversion of $CO_2$ in relatively moderate conditions, including photocatalysis, electrochemical catalysis, plasma catalysis, photothermal catalysis and so on.[25-28] Among these technical routes, solar energy-driven catalytic $CO_2$ conversion has attracted universal research interests recently, because the most abundant clean energy source, solar energy, can be efficiently utilized and converted into chemical energy in products, which can be easily integrated with the modern industrial framework.[29] Photocatalysis is the most straightforward way to exploit solar light to reduce $CO_2$ and generate solar fuels, and the process demands photoactive semiconductor materials which can generate photoexcited electron-hole pairs with high energy to trigger reactions.[30] Notably, sunlight is mostly composed of infrared (IR) and visible light (96% together in energy share), and the remaining 4% is ultraviolet (UV) light. In conventional photocatalytic process, only UV and partial visible light can be utilized and the large amount of solar energy in IR light is ignored. Together with the kinetic limitations of multi-electrons-transfer processes and poor reaction rates for $CO_2$ conversion, these challenges hinder photocatalysis for large-scale application.[31]

In order to enhance the utilization efficiency of light energy and improve the conversion activity, photothermal catalysis is proposed for highly efficient $CO_2$ reduction via the synergy of light-to-heat effect and photo-induced hot carrier-mediated activation of reactants, which paves a promising routine for the massive utilization of solar power.[32, 33] The wide range of light to be utilized in photothermal process enables

higher $CO_2$ conversion efficiencies than that in photocatalytic systems.[34] In addition, the synergetic effect between the light-induced heating and hot-carrier-mediated activation of reactants can decrease the reaction temperature and even modulate the process pathway compared with thermal catalysis.[29, 35] Therefore, photothermal catalytic $CO_2$ reduction shows a promising prospect for the production of solar fuels from $CO_2$ feedstocks.

## 1.2 The principles of photothermal catalysis

For the recent studies about the coupling of solar-heating and light-induced hot carrier-mediated activation of reactants, there are several similar terms with different contents appearing in literatures, such as photo-thermal, photothermal and photo-thermochemical reactions, which may lead to confusion among researchers and obstruct the academic communications.[36-40] Therefore, before the introduction of detailed mechanism for solar energy-driven photothermal catalysis, it is necessary to distinguish the different types of systems according to the driving forces by light irradiation in these processes. In general, based on the main effect of solar energy in the process, photothermal catalysis can be classified into photo-driven thermocatalysis and photo-thermal synergetic catalysis, where the former relies merely on light-to-heat conversion (thermal effect) and the latter is promoted by the coupling of solar-heating and hot carrier-mediated activation of reactants (non-thermal effect).[31, 32]

Most photothermal catalysts for $CO_2$ reduction involve nanometals/oxides nanostructures, due to their intrinsic physical and chemical properties for efficient light absorption, significant hot carrier generation, excellent light-to-heat conversion and outstanding catalytic activity for $CO_2$ conversion.[29, 35, 41] Hence, the discussion about the mechanism of photothermal catalysis in this part will mainly focus on the nanometals/oxides catalysts for $CO_2$ conversion.

### 1.2.1 Reaction mechanism of photo-driven thermocatalysis

One kind of photothermal process is photo-driven thermocatalysis, which sorely

relies on the light-to-heat conversion. In this type of reaction system, the input solar energy is fully converted into thermal energy on photothermal conversion materials with a broad light absorption to trigger the conversion process, and the reaction mechanism is almost the same with conventional thermal catalysis.[42]

In order to thoroughly understand the effect of light in the photothermal process, I would like to briefly introduce the process of light absorption in materials, especially plasmonic nanometals and semiconductors, which are commonly utilized in photothermal catalysis. Basically, metals are characterized by half-filled electronic bands at ground state (T = 0 K), meaning that electrons can move freely with an external energy input. In addition, semiconductors are featured by a filled electronic band, called the valence band (VB), and an empty electronic band, called the conduction band (CB), both of which are separated in energy by a band gap $E_g$.[43] Upon light irradiation on semiconductors, the electrons at ground state will be excited from the VB to CB and generate photoinduced electron-hole pairs, also called photoinduced charge carriers, if the incident photons have greater energy than the bandgap. In comparison with semiconductors, plasmonic nanometals exhibit different optical responses due to their electronic structures. Upon the incidence of light, the free electrons in metals can absorb the energy of photons and generate excited energetic electrons. Typically, if the intrinsic frequency of the free electrons oscillating in metals is corresponding to the frequency of incident photons, surface plasmon resonance (SPR) will occur, which can be interpreted as the resonant photon-induced collective oscillation of valence electrons.[39] The properties of SPR are determined by many factors, including the nature of the metal, the size and shape of the metallic architectures. When the plasmonic nanometals is in nanoscale size, the localized restriction effect, with the photon absorption and energy transfer limited within nanoscale spaces, could further enhance the intensity of light absorption near the intrinsic resonance frequency, also called localized surface plasmon resonance (LSPR) effect (Figure 1.3).[35] This localized resonance can excite the charge carriers into “hot carriers”, which possess much higher energy than those carriers excited by thermal energy input.[44]

Although these photoinduced electrons or hot carriers are highly energetic, their unstable properties lead to the short lifetimes, which restricts the efficiency of the direct utilization in catalytic processes, as shown in Figure 1.3b, c and d.[35] Upon the excitation by light irradiation, the relaxation of photoinduced charge carriers will shortly take place, through radiative and/or nonradiative decay. In radiative decay process, the relaxation of excited carriers is accompanied by the emission of photons, which is known as photoluminescence. As for the nonradiative decay process, the electron-electron scattering will occur followed by electron-phonon scattering, and finally the energy of the excited carriers will dissipate into the internal energy, resulting in thermal heating. From the quantum perspective, the light-to-heat conversion is the process of energy transformation from photon to phonon, thereby intensifying the lattice vibration and macroscopically elevating the temperature of system. Localized thermal heating by the above mechanism is usually more significant in plasmonic nanometals. As shown in Figure 1.3, the lifetimes of hot carriers in plasmonic materials are generally in the scale of femtoseconds, shorter than those of semiconductors (on the order of picoseconds to microseconds).[35] Additionally, the light absorption via LSPR effect in plasmonic nanostructures usually falls into visible light range, the major part of solar light. Therefore, it has attracted much research interest to utilize plasmonic nanomaterials in solar-to-heat conversion process for light-driven thermocatalysis.[45]

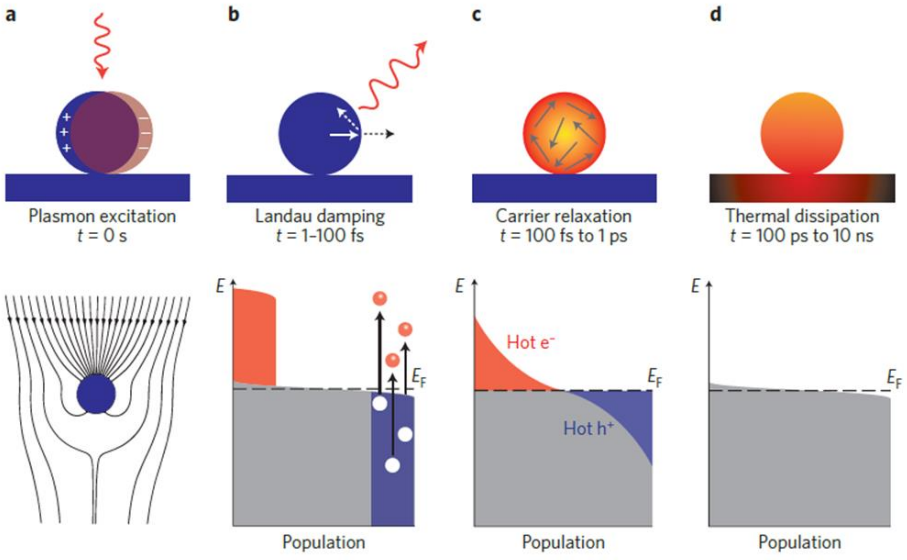


**Figure 1.3** Photo-induced excitation and subsequent relaxation processes of charge

carriers in metal nanoparticles. (a) Excitation process via the localized surface plasmon resonance (LSPR). (b) In the initial 100 fs period, the athermal distribution of hot charge carriers, following Landau damping, undergoes decay through either re-emission as photons or electron-electron interaction-induced carrier multiplication. (c) Electron-electron scattering processes occur within a timescale ranging from 100 fs to 1 ps, leading to the redistribution of the hot carriers' energy. (d) Heat is transferred from the metallic structure to its surroundings via thermal conduction on a longer timescale ranging from 100 ps to 10 ns.[35]

### 1.2.2 Reaction mechanism of photo-thermal synergetic catalysis

Another kind of photothermal process is photo-thermal synergetic catalysis, which is promoted by the coupling of solar-heating and light-induced hot carrier-mediated activation of reactants. In this system, the role of light irradiation cannot be simply described as the energy input to elevate the reaction temperature through the photo-to-heat effect as described above, and the introduction of light incidence could lead to different results of catalytic reactions even though the system temperature remains the same, thereby suggesting a different reaction routine with thermal catalysis.

With the excitation by photons, the generated hot carriers via LSPR effect in nanometals are highly energetic and those with suitable energy level can transfer to the surface active sites and interplay with absorbed reactants or reaction intermediates through accessible orbitals, thereby driving the redox reactions, which is called indirect energy transfer mechanism (Figure 1.4a).[46] In this reaction process, the position of the absorbent state relative to the Fermi level of nanometal will significantly influence the migration of energetic charge carriers. Due to the distribution of photoinduced hot carriers follows the Fermi-Dirac distribution, close to the Fermi level, the transfer of hot carriers are more expected to proceed with the adsorbate states closer to the Fermi level. In comparison with process driven by thermal energy, this reaction mechanism might trigger some unique conversion process. However, the complicated carrier migration hinders the significant control of the transfer process (that is, transfer to designed orbitals of reactants), restricting the ability to control product selectivity.

In addition to the indirect energy transfer process, plasmonic nanomaterials can also activate the reactants via chemical interface damping of plasmons, called direct energy transfer (Figure 1.4b).[44] The interplays between nanometals and absorbents result in the transformation of interfacial electronic states, providing another pathway for the dissipation of energy converted from photons via LSPR effect, in which the electrons in absorbents are directly excited and the reactants are activated. Generally, metallic materials, especially coinage nanometals (Cu, Ag, and Au), are featured by relatively high concentration of carriers and exhibit strong LSPR effect, which are regarded as specific plasmonic materials.

Moreover, semiconductors, especially metal oxides, have also been utilized for the photothermal synergetic catalysis. Similar to the mechanism of photocatalysis, the photo-induced electrons in CB are capable to transfer to the absorbed reactant molecules or intermediate groups, thereby enhancing the reaction process together with the solar-heating effect. However, due to the elevated temperature in semiconductors, the excited charge carriers will act more disorderly and are easier to recombination than that in photocatalysis at low temperature. Therefore, it is necessary to extend the photon absorption range to excite more energetic carriers and also to prolong the lifetime of charge carriers in catalysts through the rational design of materials.

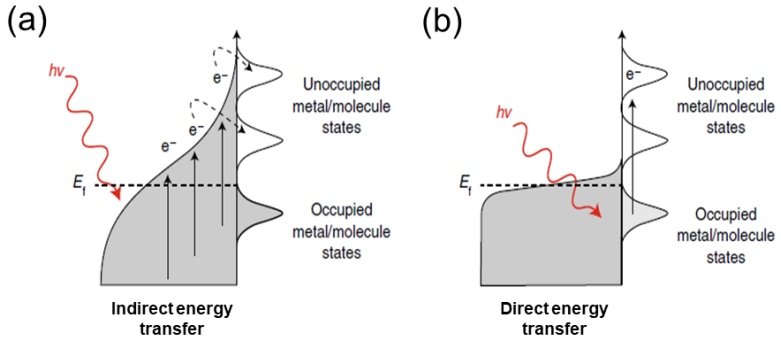


**Figure 1.4** Mechanism of light-induced hot carrier-mediated activation of reactants. (a) Indirect energy transfer mechanism. Plasmonic resonance generates excited electrons with high energy, and the charge carriers with suitable energy may mitigate into the interfacial metal-adsorbent states. (b) Direct energy transfer mechanism. Plasmon relaxation leads to the direct excitation of electrons in the absorbent at the interface.[47]

It should be pointed out that the above situations are simplified cases for understanding, and the practical situation is much more complicated. Despite of the demand to explore the principle of photothermal catalysis, there are several undoubtable advantages of this technology. First, it will effectively alleviate the energy crisis and environmental issues to exploit the abundant and renewable solar energy and produce solar fuels. Second, the synergy of solar heating and photo-induced hot carrier-mediated activation of reactants will address the problems of low activity in photocatalysis and harsh conditions in thermal catalysis. Third, the reaction routines could be altered by the energetic hot carriers, thereby providing alternatives for the modulation of product selectivity.

## 1.3 Recent research on photothermal catalytic $CO_2$ hydrogenation

The utilization of $CO_2$ is usually conducted with other reducing agents, such as $H_2$, $CH_4$ and $H_2O$, through catalytic processes requiring sufficient energy input.[24] Among the multiple techniques, photothermal catalytic $CO_2$ hydrogenation with renewable $H_2$ has attracted enormous interests due to its high conversion efficiency and various products which could be regulated by the catalysts and reaction conditions.[34] Due to the complexity of the possible reaction pathways of $CO_2$ hydrogenation (Figure 1.5), a variety of products could be obtained under proper conditions.[48] It could be recognized that the production of $CO_2$ conversion can be divided into several aspects: (1) C1 molecular including CO, $CH_4$, (2) $C_{2+}$ hydrocarbons including alkanes, olefins and alkynes, and (3) valuable oxygenates such as alcohols and carboxylic acids. This part will mainly focus on the recent research progress in the field of photothermal catalytic $CO_2$ hydrogenation.

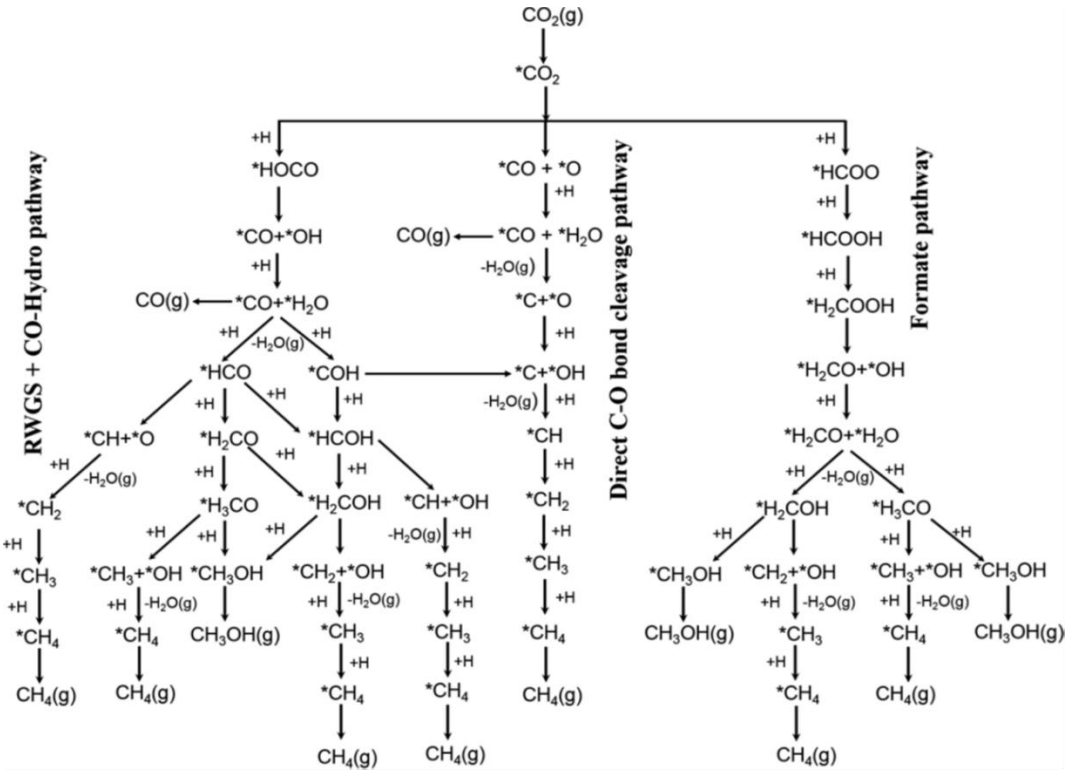


**Figure 1.5** Proposed reaction routines for $CO_2$ hydrogenation process with carbon monoxide (CO), methane ($CH_4$) and methanol ($CH_3OH$) as products. $^*$(X) suggests adsorbed species.[48]

### 1.3.1 Reversible water gas shift (RWGS) reaction

Carbon monoxide (CO) is not only a kind of widely used gaseous fuel, but also a valuable feedstock in modern chemical industries, such as methanol synthesis and hydrocarbon production via Fisher-Tropsch synthesis.[49] Therefore, the production of CO via the RWGS reaction ($CO_2 + H_2 \rightarrow CO + H_2O$, $\Delta H°_{298K}$ = +41.2 kJ $mol^{-1}$) is regarded to be one of the important routes in $CO_2$ utilization system. With the moderate ratio of $CO_2/H_2$, syngas ($CO/H_2$) can be produced via the photothermal catalytic RWGS reaction and transformed to subsequent synthesis process for value-added chemicals. In general, metal oxides and supported metal nanoparticles, including noble metal (Pd, Au) and non-noble metal (Cu, Fe, Co), have been applied for photothermal catalytic RWGS reaction.

Ozin's group has reported a series of studies about $In_2O_3$-based photothermal catalyst

for RWGS reaction.[50-52] The $In_2O_{3-x}(OH)_y$ nanostructures derived from the annealing treatment of $In(OH)_3$ precursors exhibited an enhanced photothermal $CO_2$ conversion rate of 150 μmol $g^{-1}$ $h^{-1}$ under 1 sun irradiation (0.1 W $cm^{-2}$) at 190 °C, four times higher than that without light irradiation. In situ spectroscopic and kinetic analysis, together with theoretical calculations, demonstrated the frustrated Lewis pair (FLP) chemistry-related mechanism, in which the synergy between surface active sites and oxygen vacancies of $In_2O_{3-x}(OH)_y$ promoted the adsorption and decomposition of hydrogen and subsequently enhanced the activation and conversion of $CO_2$, thereby enhancing the CO production. Afterwards, in order to improve light-harvesting efficiency, the $In_2O_{3-x}(OH)_y$ was deposited on vertically aligned Si nanowires (SiNW), which could absorb ~80% of the solar light due to the low bandgap of Si (1.1 eV) (Figure 1.6a).[51] Using light irradiation (2.0 W $cm^{-2}$) as the only energy input, the $In_2O_{3-x}(OH)_y$/SiNW film was heated up to 150 °C and showed the highest CO production of 22.0 mmol $g^{-1}$ $h^{-1}$, 6 times higher than that on the $In_2O_{3-x}(OH)_y$/glass film, which could be attributed to the efficient light-to-heat conversion within the SiNW support by absorbing the photons with energy less than the band gap (2.9 eV) of $In_2O_{3-x}(OH)_y$. In contrast, the $In_2O_{3-x}(OH)_y$ /glass film was unable to absorb and utilize these photons, suggesting the significance of designing nanomaterial structures to utilize the full solar spectrum.

Qi et al fabricated a novel 2D black $In_2O_{3-x}$ nanosheets with photoinduced-defective sites (Figure 1.6b).[53] Upon the irradiation of a 300 W Xe lamp, the temperature on catalyst surface reached 340 °C and a remarkable CO production of 103.2 mmol $g^{-1}$ $h^{-1}$ was achieved with near-unity selectivity towards CO. Detailed studies and theoretical calculations demonstrated that the bifunctional oxygen vacancies in the 2D black $In_2O_{3-x}$ nanosheets host enhanced light utilization and provided absorption sites for $CO_2$ molecules, therefore improved the conversion from $CO_2$ to CO.

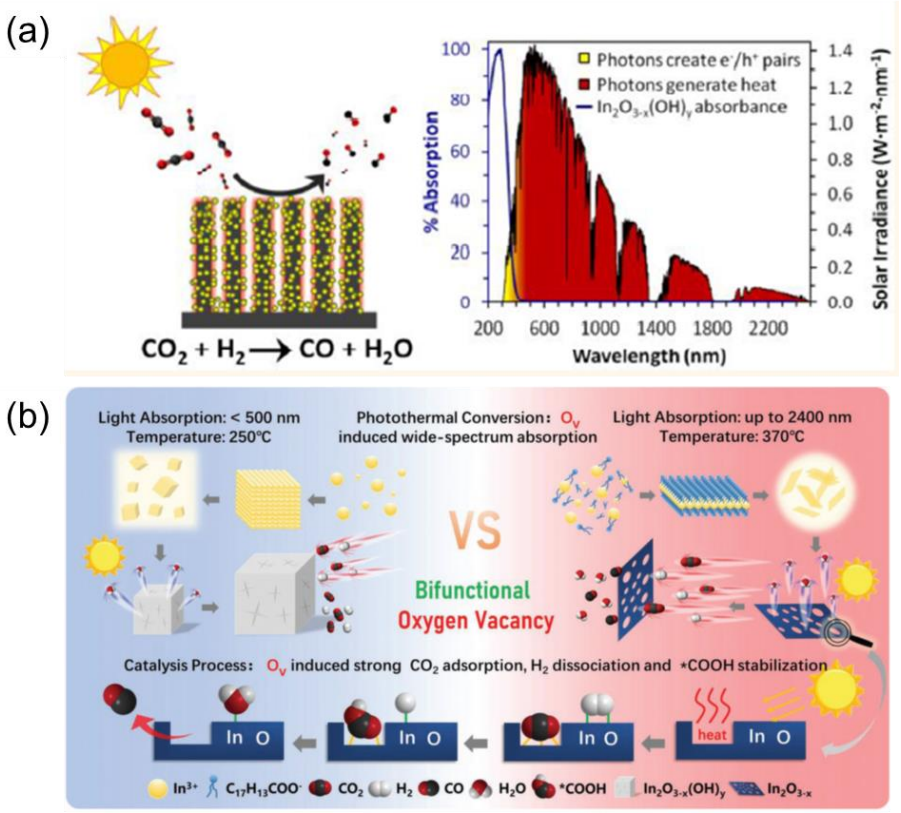


**Figure 1.6** Photothermal catalytic RWGS reaction. (a) Schematic illustration of nanostructures of $In_2O_{3-x}(OH)_y$/SiNW film and the utilization of photons with different energies.[51] (b) Schematic illustration of the bulk $In_2O_3$ and 2D black $In_2O_{3-x}$ nanosheets with bifunctional photoinduced oxygen vacancies.[53]

In addition to metal oxides, supported metal nanoparticles are considered to be promising catalysts for photothermal catalytic RWGS.[54-56] Among the various active metals in catalytic reactions, a series of plasmonic metals (Cu, Al, Ru, Fe and Co) have been utilized to promote $CO_2$ activation by photo-induced hot carriers.[55, 57-61] In a typical work, $CuPd/H_yWO_{3-x}$ nanocomposite was designed and utilized for photothermal RWGS reaction, and the introduction of 0.2 at% Cu onto $WO_3$ surface remarkably enhanced the $CO_2$ conversion to CO process compared with $Pd/H_yWO_{3-x}$.[62] The in situ diffuse reflectance infrared Fourier transform spectroscopy (DRIFTS) revealed that the formation of surface carboxylate species from $CO_2$ was promoted by Cu, leading to a 3 - 5 times enhancement in CO production. In addition, cuprous oxide ($Cu_2O$) nanocubes were also reported to efficiently convert $CO_2$ to CO in the photothermal process.[63] Under the irradiation of visible light (50 suns) and pressure of

4 bar, 139.6 mmol $g^{-1}$ $h^{-1}$ CO production rate was obtained on CF-$Cu_2O$ catalyst. The excellent reaction activity was attributed to the various copper sites with mixed chemical states of Cu (0, +1, +2), hydroxyl OH groups and oxygen vacancies on the $Cu_2O$ nanocubes, which enabled the adsorption of $CO_2$ and decomposition of $H_2$ under mild conditions, thereby promoting the photothermal RWGS process.

Halas group has reported a plasmonic Al@$Cu_2O$ antenna-reactor heterostructure for photothermal catalytic RWGS reaction (Figure 1.7).[59] The catalyst was fabricated via growing a $Cu_2O$ shell (~15 nm in thickness) around the aluminum core (~100 nm in diameter), separated by a 2 ~ 4 nm thick $Al_2O_3$ layer. Upon the 10 W $cm^{-2}$ visible light irradiation (100 suns), the surface temperature of the catalysts was elevated to 175 ºC. Compared with the pure thermal RWGS reaction, the $CO_2$ conversion process was significantly promoted and CO was selectively generated in the photothermal process, implying a unique reaction pathway with the assistance of light. Experimental and theoretical analyses demonstrated that due to the energy band alignment between Al and $Cu_2O$, hot carriers were generated through LSPR damping in the Al core or the near-field excitation in the $Cu_2O$ shell. The energetic charge carriers were quickly transferred into the unoccupied states of absorbed carbon dioxide on $Cu_2O$ shell surface, following by the dissociation of C-O bond and enhancement of CO production.

Fe nanoparticles with certain size were also reported to exhibit LSPR effect under light irradiation, and the light-induce hot carriers could facilitate the activation of $CO_2$ in the photothermal catalytic RWGS process.[60] The plasmonic Fe@C catalyst was characterized by Fe nanoparticles (less than 10 nm in diameter) encapsulated by ultrathin carbon layers (1 ~ 3 layers), derived from the two-step calcination of a Fe-containing metal-organic-framework (MOF). The synergy of the photo-heating induced by visible and IR light and the hot carriers generated by UV light via LSPR effect contributed to the solar-driven CO production through RWGS reaction.

Au is a widely recognized plasmonic metal and also a potential active metal for RWGS reaction. Lu et al has reported an Au/$CeO_2$ catalyst for photothermal RWGS reaction with much better performance under photothermal process than thermal

process.[64] The visible light irradiation excited abundant hot carriers in Au nanoparticles, which accelerated the $H_2$ dissociation and the formation of Au–H species on Au/$CeO_2$, subsequently facilitating the activation of $CO_2$. Therefore, the production rate of CO was significantly enhanced by ~10 times higher than that in the thermocatalytic process under the same condition.

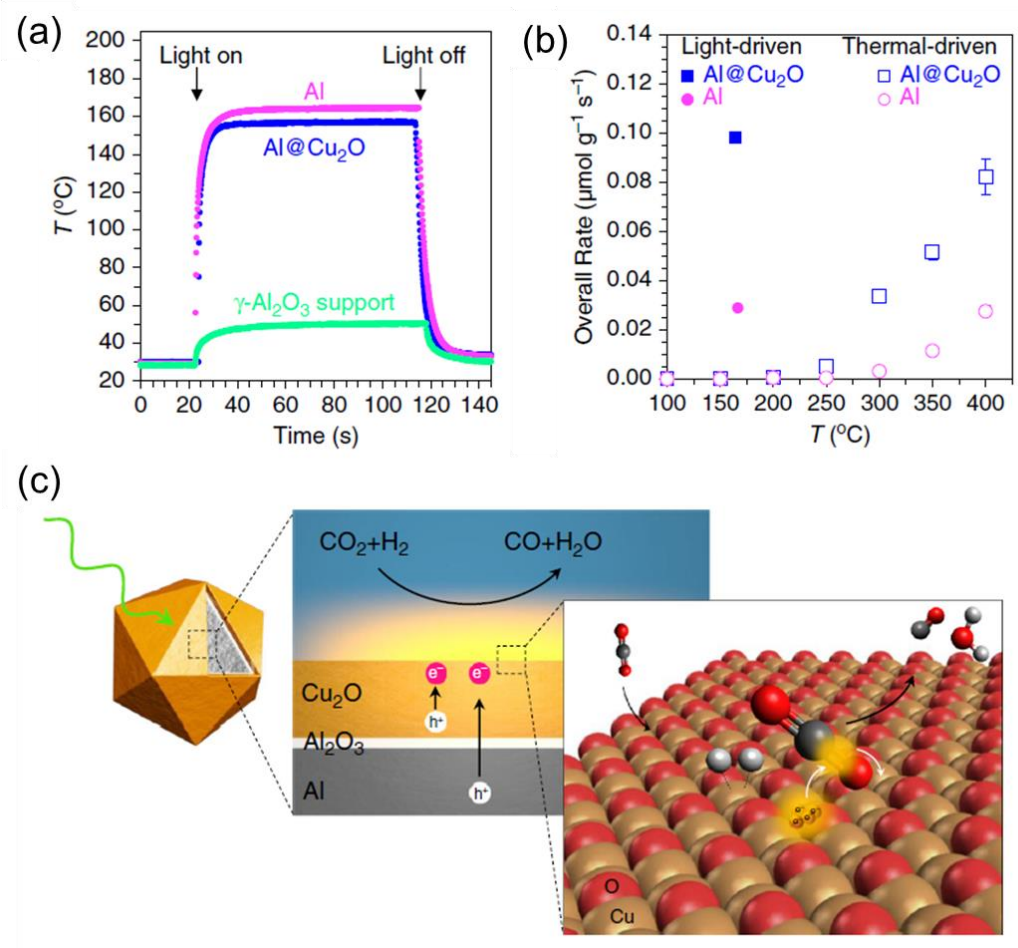


**Figure 1.7** Light-driven $CO_2$ reduction on Al@$Cu_2O$. (a) Time-resolved monitoring of surface temperature for oxide supported plasmonic Al@$Cu_2O$ nanostructures and pure $Al_2O_3$ support with and without light incidence in air. (b) The overall reaction rate on Al@$Cu_2O$ and Al NCs in pure thermocatalytic process at different temperatures (unfilled data points), and light-driven RWGS process (filled data points). (c) Schematic illustration of photothermal RWGS reaction over plasmonic Al@$Cu_2O$ nanostructure.[59]

### 1.3.2 Methanation

Methane ($CH_4$), the predominant composition of nature gas, is widely used as a clean and environmental-friendly energy source and chemical feedstock. $CO_2$ methanation reaction is also called Sabatier reaction ($CO_2 + 4H_2 \rightarrow CH_4 + 2H_2O$, $\Delta H°_{298K}$ = -165.1 kJ $mol^{-1}$). Because the conversion from $CO_2$ to $CH_4$ is a reduction process of eight electrons, the methanation reaction is kinetically unfavorable and usually occurs at a relatively high temperature (> 300 ºC), despite of its exothermic properties.[34] It has attracted extensive research interest to develop efficient photothermal catalysts for the high energy-consumption $CO_2$ methanation reaction using renewable solar energy.[40] Generally, group VIII metals and their oxides, especially Ru and Ni, are among the most active catalysts.[65]

Since the pioneering work by Meng et al in 2014, Group VIII metals (Ru, Rh, Fe, Co, Ni, Pt and Pd) supported on $Al_2O_3$ substrate were featured by their excellent ability to elevate the system temperature to ~400 ºC by photothermal heating under a 300 W xenon lamp for photothermal $CO_2$ methanation.[40] Layer double hydroxide (LDH) has been reported to act as a platform to synthesize well dispersed metal/oxide nanocomposites, due to its versatile chemical composition and orderly structural architecture.[66, 67] Lately, Ren et al reported that Ru nanoparticles supported on ultrathin Mg-Al LDH (denoted as Ru@FL-LDHs) showed considerable methane production activities from $CO_2$ hydrogenation with irradiation of around 10 suns (Figure 1.8a and b).[68] In the flow-type reaction, the $CH_4$ yield rate reached 277 mmol $g^{-1}$ $h^{-1}$ over Ru@FL-LDHs, while the pure FL-LDHs exhibited almost no activity for $CO_2$ conversion. The temperature of Ru@FL-LDHs catalyst was about 350 ºC under light irradiation, much higher than the 67 ºC of FL-LDHs in the process. The temperature-dependent activity suggested that the light-to-heat effect on Ru NPs contributed to the efficient $CO_2$ methanation over Ru@FL-LDHs.

Additionally, Zhang et al developed a variety of catalysts for $CO_2$ hydrogenation via the annealing of multiple-component LDH precursors.[69, 70] The LDH-derived CoFe alloyed NPs on amorphous $Al_2O_3$ support produced $CH_4$ with a selectivity of ~60% under UV-visible light irradiation.[69] Another work by their group reported a Ni/$Al_2O_3$

catalyst derived from $H_2$ reduction of LDHs at different temperatures (300 – 600 °C) for photothermal methanation of $CO_2$.[70] Without external heating sources, the highest $CH_4$ production was obtained over the sample prepared at 600 °C under UV-vis-IR light irradiation. The activity and selectivity of solar-driven $CO_2$ hydrogenation and controlled thermocatalytic reaction were quite similar at all temperatures, implying that the methanation process was driven by the photothermal heating of Ni NPs.

The plasmonic nanostructures with abundant photo-induced hot carriers have also been applied for photothermal $CO_2$ methanation process.[73-75] The highly energetic charge carriers generated by the LSPR decay in plasmonic metals could be transferred into the absorbed reactants to participate in the reaction process or dissipate to heat the environment. Therefore, such synergetic effects of plasmonic metals could enhance the $CO_2$ hydrogenation to methane reaction. Typically, Ag and Au-based nanocomposites are well-known for their strong LSPR response to visible light, implying their potential in photothermal catalysis.[39, 76] Jin et al synthesized well-designed $Ag_{25}$ clusters consisted of an $Ag_{13}$ core and an incomplete $Ag_{12}$ exterior shell (Figure 1.8c and d).[71] The $Ag_{25}$ clusters exhibited competitive catalytic activity for solar-driven $CO_2$ methanation with an almost 100% methane selectivity at a relatively mild condition (100 °C). The study demonstrated that the strong absorption by LSPR effect together with the abundant active sites contributed to the competitive methanation activity.

In addition, Halas and colleagues have proposed a “heterometallic antenna-reactor” system composed of plasmonic metal and catalytically active metal, which could offer a novel pathway to break through the limitations of single plasmonic metal in sluggish reaction, such as $CO_2$ methanation.[46, 77] Inspired by such concept, the plasmonic nanostructures of bimetals have been investigated for $CH_4$ production from $CO_2$ hydrogenation recently.[78, 79] Stanley et al developed the silica ($SiO_2$) supported Ni-Au catalyst for photothermal methanation reaction via the deposition-precipitation method.[80] Under laser light irradiation of 520 nm, $CO_2$ conversion for Ni-Au/$SiO_2$ was increased by 79%, which could be attributed to the plasmon-mediated hot electron charge transfer from Au to Ni and adjacent reactants. Fu et al developed another

nanoantenna system of Rh/Al for photothermal catalysis.[81] An unprecedented $CH_4$ production of 550 mmol $g^{-1}$ $h^{-1}$ with almost 100% selectivity was achieved under the concentrated simulated solar irradiation (11.3 W $cm^{-2}$). The excellent performance of catalyst was due to the coupling of photoheating effect by the wide-spectrum absorption and hot carrier-mediated activation of reactants induced by the LSPR and nanoantenna effect of Rh/Al nanostructure. Zhang et al also reported a novel plasmonic bimetal–semiconductor heterostructure Au@AuRu/g-$C_3N_4$ for photothermal catalytic methanation of $CO_2$ (Figure 1.8e).[72] Under light irradiation at 150 °C, a remarkable $CH_4$ production of 103 μmol $g^{-1}$ $h^{-1}$ with 98.4% selectivity was achieved, which was eleven times higher than that under dark, and 2.6 and 12 times higher than that of Au@Ru/g-$C_3N_4$ and Au/g-$C_3N_4$, respectively. The detailed study revealed that the synergy between the metal-semiconductor heterojunction and the surface structure extended the life of hot electrons to promote catalytic reaction.

Lately, synthesizing well-dispersed metal-based catalysts from the calcination of metal-organic frameworks (MOFs) precursors has emerged as an effective strategy to develop efficient and stable catalysts due to the well-separated metal ions by the organic linkers.[25, 82-84] Relative studies have demonstrated that MOF-derived metal oxide catalysts exhibit enhanced metal-support interactions and physicochemical properties, as well as promoted performance in various catalysis.[58, 85] Chen et al utilized the MOFs-templated approach to synthesize a series of Co/$Al_2O_3$ catalysts, using $Al_2O_3$@Co-ZIF-67 as the precursor.[58] The optimized 21% Co/$Al_2O_3$ showed 6.04 mmol $g^{-1}$ $h^{-1}$ production of $CH_4$ with 97.7% selectivity and good durability under 1.3 W $cm^{-2}$ irradiation of UV-vis-IR light in the gas-phase photothermal $CO_2$ methanation experiment. The remarkable methanation activity was ascribed to the high dispersion of Co, the strong interaction between Co and $Al_2O_3$, the strong absorption across the entire solar spectrum, and the UV-vis light induced oxygen vacancies in Co/$Al_2O_3$ catalyst.

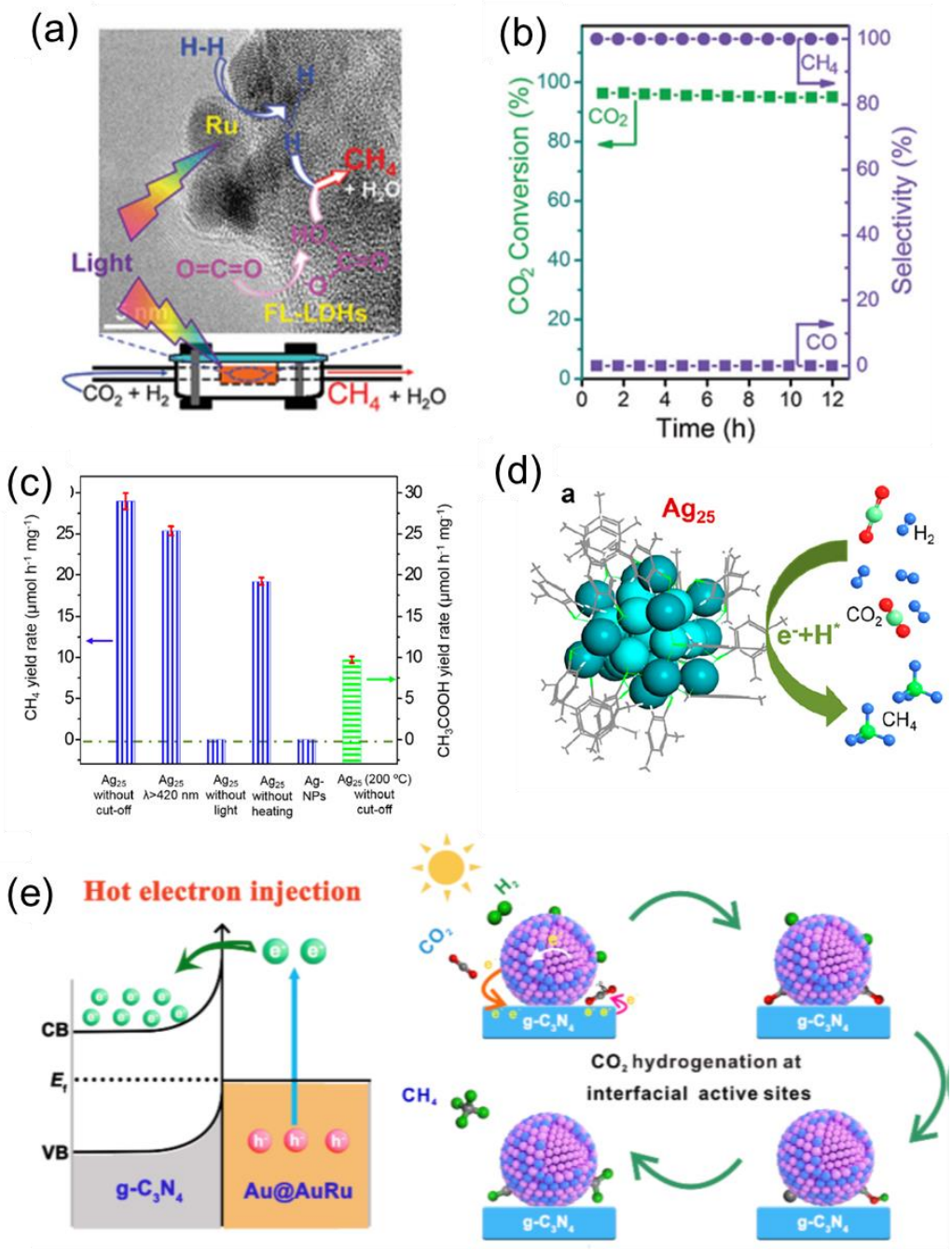


**Figure 1.8** Methane production from photothermal $CO_2$ hydrogenation. (a) Schematic for activation and conversion of $CO_2$ and $H_2$ in the photothermal catalytic $CO_2$ methanation process over Ru@FL-LDHs, and (b) stability test of $CO_2$ methanation over Ru@FL-LDHs.[68] (c) $CH_4$ and $CH_3COOH$ production rate in photo-driven catalytic $CO_2$ reduction over $Ag_{25}$ nanoclusters in different conditions, (d) Schematic exhibition of the $Ag_{25}$ nanocluster.[71] (e) Illustration of hot electron transfer mechanism and $CO_2$ hydrogenation process on Au@AuRu/g-$C_3N_4$.[72]

### 1.3.3 Methanol synthesis

Methanol ($CH_3OH$), important chemical industrial feedstocks, is also regarded to be a promising candidate for clean and renewable energy carrier because of its high volume-specific energy density.[86] George A. Olah has drawn a future prospect about "methanol economy", in which methanol acts as the medium for energy consumption and chemical industry in the near future.[87] Methanol production from photothermal catalytic $CO_2$ hydrogenation ($CO_2 + 3H_2 \rightarrow CH_3OH + H_2O$, $\Delta H°_{298K}$ = -49.5 kJ $mol^{-1}$) is considered as a sustainable and environment-friendly route and has attracted great research interests.[25, 88, 89] During the past several years, some efforts have been taken to achieve efficient methanol production by photothermal catalytic $CO_2$ hydrogenation.[90-92] However, until now, the unsatisfied activity and selectivity indicate that further improvement are necessary for efficient photothermal catalysts.

$In_2O_3$ has been regarded as a promising catalyst for catalytic $CO_2$ hydrogenation to methanol including thermal catalysis, photocatalysis and photothermal catalysis, according to recently reported studies.[93-95] Recently, Ozin's group reported a rod-like $In_2O_{3-x}(OH)_y$ nanostructures for $CH_3OH$ production by photothermal process under atmospheric pressure at 250 °C (Figure 1.9a-c).[90] Upon the simulated solar light irradiation, the photothermal production rate of $CH_3OH$ could reach 97.3 μmol $g^{-1}$ $h^{-1}$ and maintain at ~60 μmol $g^{-1}$ $h^{-1}$, with the selectivity remained above 50% at ambient pressure. The excellent performance of $In_2O_{3-x}(OH)_y$ nanostructures was attributed to the superior properties of the surface frustrated Lewis pairs (SFLP) and the prolonged lifetime of the photoinduced charge carriers within the rod-like catalysts.

Cu is also a well-known active metal for efficient methanol synthesis from $CO_2$ hydrogeneration in thermocatalysis. Considering its potential for LSPR effect in the range of visible light, Cu-based materials shows a promising prospect for photothermal $CO_2$ hydrogenation to methanol. Cu/ZnO was prepared by the co-precipitation method for photothermal $CO_2$ hydrogenation to methanol reaction.[96] At 220 °C, the Cu/ZnO catalyst with abundant Cu-ZnO interfaces exhibited a methanol production of ~84 μmol $g^{-1}$ $h^{-1}$ without light irradiation at ambient pressure. Upon the incident of visible light,

the methanol yield was improved by 54% to ~127 μmol $g^{-1}$ $h^{-1}$. The detailed studies illustrated that the plasmonic Cu nanoparticles contributed to the photo enhancement through the hot carrier activation induced by LSPR effect. Transient absorption spectra further demonstrated that the photo-induced hot electrons could be effectively transferred from Cu NPs to ZnO, which facilitated the activation of reaction intermediates and thereby promoted the methanol generation.

Recently, Xie et al utilized the $Cu/ZnO/Al_2O_3$ catalyst for photothermal catalytic $CO_2$ conversion to methanol under UV-visible light (350 nm – 800 nm) (Figure 1.9d-f).[97] At low temperature (225 °C) with light irradiation, the methanol activity was enhanced by around 40% than that without light. With the increase of reaction temperature, there was almost no enhancement by light on the production of methanol. Control experiments under different wavelengths of light demonstrated that the simultaneous excitation of ZnO and Cu is essential to enhance the methanol generation. In situ DRIFTS and DFT calculations indicated that $CO_2$ and $H_2$ were activated by the photo-excited electrons induced by ZnO excitation and Cu LSPR effect, respectively. Under the UV-vis light irradiation, the synergetic promotion by photo-induced carriers at the Cu-ZnO interface accelerated the activation and dissociation of $CO_2$ and $H_2$, which led to the enhanced photothermal catalytic methanol production.

In addition, Zhang et al developed a hybrid structure (Au&Pt@ZIF) by encapsulating Au nanocages and Pt nanocubes by a zeolite imidazolate framework (ZIF-8) for photothermal methanol generation.[98] With light irradiation, the LSPR effect of Au generated considerable hot carriers and the heat generated by the dissipation of hot electrons was enclosed within the MOFs nanocages to form localized high-temperature area, thus considerably enhancing the performance of Pt nanocubes at very low temperature (150 °C). The control experiments indicated that the Au served as the nanoheater via the LSPR effect and the MOFs were functioned as heat insulators, thereby promoting the reaction process on Pt active sites. This rational design paved a revenue for feasibly utilizing photothermal effect in nanoplasmonic catalysts.

To date, there are only a small number of studies on the production of methanol

through photothermal means at mild conditions, particularly under ambient pressure.[66, 90, 93] Among these studies, the activity and selectivity are still rather inadequate, thereby impeding the progress of photothermal methanol production via $CO_2$ hydrogenation. In addition, there is a need for further investigation and discussion to clarify the detailed mechanisms.

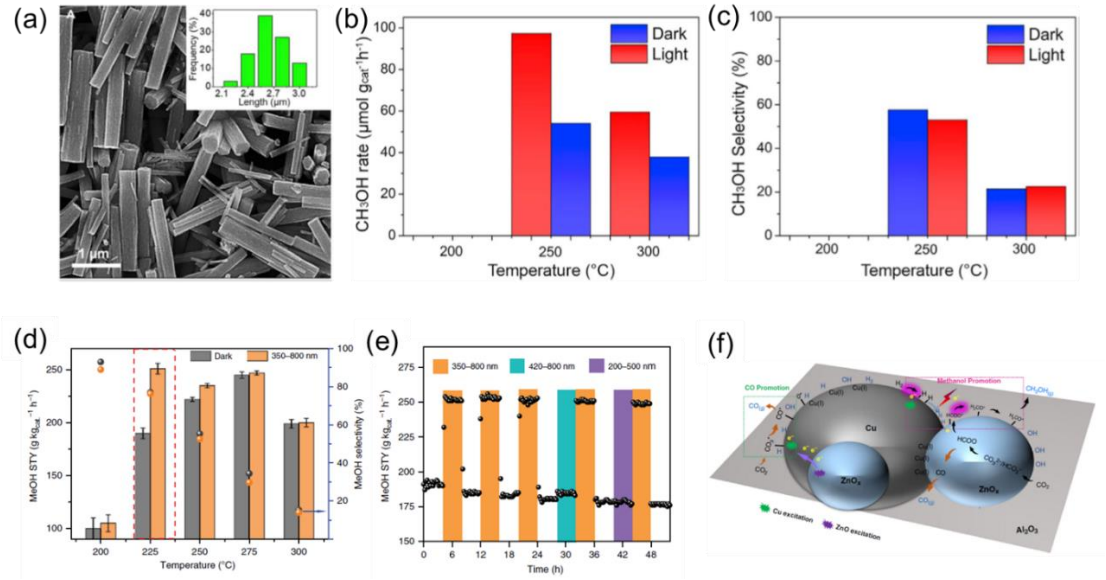


**Figure 1.9** Methanol synthesis from photothermal catalytic $CO_2$ hydrogenation. (a)-(c) Methanol production over $In_2O_{3-x}(OH)_y$ nanostructures. (a) SEM image of $In_2O_{3-x}(OH)_y$ nanostructures, (b) methanol production rate and (c) selectivity in catalytic $CO_2$ hydrogenation over $In_2O_{3-x}(OH)_y$ nanostructures at 250 ºC with and without light.[96] (d-f) Photothermal methanol synthesis over $Cu/ZnO/Al_2O_3$. (d) Methanol space time yield (STY)/selectivity at 200–300 °C without light and with 350–800 nm light irradiation, (e) time-on-stream methanol production under different light irradiation conditions (350–800 nm, 420–800 nm, and 200–500 nm at 225 °C), and (f) schematic illustration of light-assisted methanol synthesis from $CO_2$ hydrogenation over $Cu/ZnO/Al_2O_3$ catalyst.[97]

### 1.3.4 $C_{2+}$ hydrocarbon and alcohol synthesis

CO, $CH_4$ and $CH_3OH$ are valuable $C_1$ products from $CO_2$ hydrogenation and their catalysis processes have been widely studied with considerable progress. However,

considering the prospects for applications, it will be exciting if we could obtain various highly-valuable and easily marketable fuels and chemicals including $C_{2+}$ hydrocarbons and higher alcohols from direct photothermal catalytic $CO_2$ hydrogenation process.[88] To this end, Chen et al developed a series of CoFe-based catalysts via the hydrogen-reduction of CoFeAl LDH nanosheets at 300 – 700 °C for photothermal $CO_2$ hydrogenation.[69] As shown in Figure 1.10a, with the change of $H_2$ treatment temperatures, the resulted CoFe-x catalysts exhibited quite different activities and selectivities for the product distribution under UV-vis light irradiation. When the reduction temperature increased above 600 °C, the CoFe-650 catalyst exhibited a remarkable selectivity towards $C_{2+}$ hydrocarbons (60% $CH_4$, 35% $C_{2+}$) with the assistance of photoheating effect. The CoFe alloy nanostructure facilitated the C-C coupling process and demonstrated a novel way for $CO_2$ hydrogenation to highly-valuable products by solar energy.

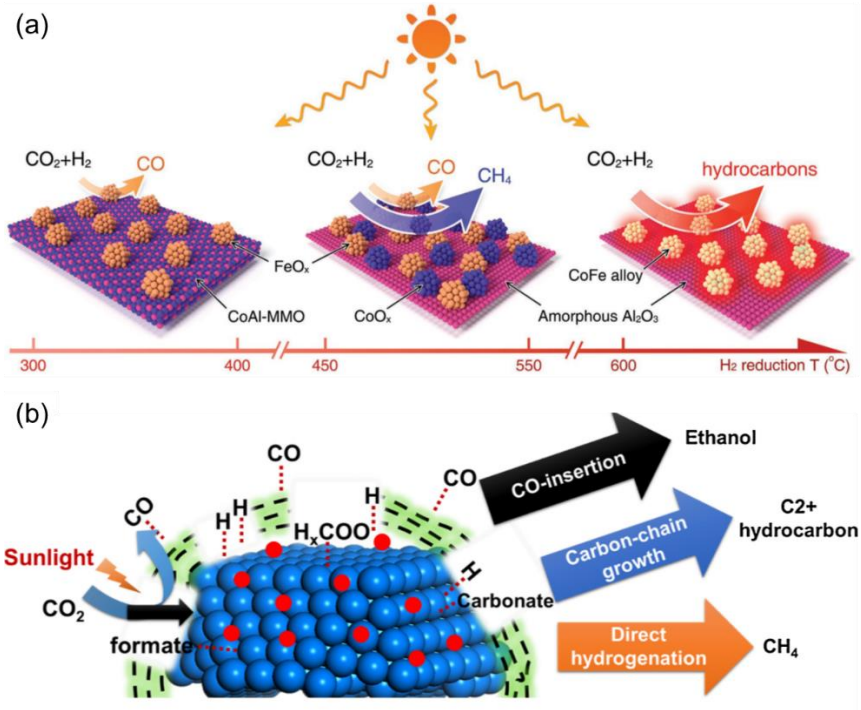


**Figure 1.10** $C_{2+}$ hydrogenation and alcohols synthesis from photothermal catalytic $CO_2$ hydrogenation. (a) Schematic illustration of the different CoFe-x alloys derived from the $H_2$ reduction of CoFeAl-LDH precursors at different temperatures.[69] (b) Schematic exhibition of the $CO_2$ hydrogenation process with light irradiation over Na-Co@C. Na

is displayed with red circles.[99]

Additionally, Liu et al reported a sodium promoted Co@C catalyst for photothermal $CO_2$ hydrogenation into $C_{2+}$ hydrocarbons and ethanol, as shown in Figure 1.10b.[99] The photothermal $CO_2$ hydrogenation was carried out at 2.8 bar and 235 ºC under 2.4 W $cm^{-2}$ simulated sunlight from a Xe lamp. With the assistance of light irradiation, the Na-promoted Co@C catalyst exhibited almost 100% selectivity towards hydrocarbons, including 16.5% $C_{2+}$ and 12.5% $C_{3+}$. The detailed investigation implied that the UV-vis light excited the Co@C nanoparticles and generated hot carriers, which participated in the catalytic process of $CO_2$ activation. Moreover, the carbon layer stabilized the intermediate CO on the catalyst surface and facilitated the formation of ethanol via a CO insertion mechanism.

## 1.4 Research motivation and thesis organization

Solar energy-driven photothermal catalytic $CO_2$ hydrogenation to valuable fuels and chemicals is a promising technology to alleviate the gradually deteriorative environment and energy problems simultaneously, compared with the conventional thermocatalytic $CO_2$ hydrogenation which heavily relies on the consumption of fossil fuels. On the base of the above overview, nanometals/oxides catalysts, featuring good catalytic activity for $CO_2$ activation and conversion, are considered as promising candidates for photothermal catalytic $CO_2$ hydrogenation. With the plausible design of nanostructures, nanometal-based catalysts, such as Cu- and Ru-based composites, can exhibit a remarkable performance via the synergetic effects of light-to-heat conversion and photo-induced hot carrier-mediated activation of reactants. However, although many efforts have been taken to investigate the photothermal catalysis over the past few years, it still remains challenging to develop catalysts with high efficiency, good stability and desired reaction selectivity for photothermal $CO_2$ hydrogenation, and also to clarify the mechanism of photo-driven $CO_2$ conversion and illustrate the influence of metal-support interaction on the process. Therefore, this thesis focuses on the rational design of nanometals (Cu, Ru)/oxides catalysts for highly efficient and long-term stable

photothermal catalytic $CO_2$ hydrogenation at mild conditions by coupling light-to-heat effect and photo-induced hot carrier-mediated activation of reactants, as well as selectively generating highly valuable solar methanol under ambient pressure. This dissertation is divided into five chapters. A summary of the remaining four chapters is described as below:

**Chapter 2 Metal-organic framework-derived Ga-Cu/$CeO_2$ catalyst for highly efficient photothermal catalytic $CO_2$ reduction**

Cu, the abundant and low-cost metal, is among the most catalytically active catalysts for RWGS reaction, while the high reaction temperature usually results the fast deactivation of catalysts. Recent researches have reported well-dispersed and efficient catalysts derived from metal-organic frameworks (MOFs) for various catalytic reactions, due to the improved physicochemical properties and promoted metal-support interactions. In addition, $CeO_2$ is an excellent support to stabilize and well disperse the loading metals and produce strong metal-support interactions due to its unique redox properties. Moreover, to further enhance the activity of Cu-based catalysts, several research groups have investigated the utilization of Ga as a promoter in $CO_2$ hydrogenation. Therefore, the rational design of $CeO_2$ supported highly dispersed Cu and Ga catalysts is expected as a promising approach for efficient photothermal RWGS reaction. In this chapter, a Ga-Cu/$CeO_2$ catalyst was synthesized by direct pyrolysis of the Ga and Cu-containing Ce-metal-organic frameworks for efficient photothermal catalytic CO production. It can be expected that the high dispersion of Cu and Ga on $CeO_2$ can contribute to the good performance of solar-driven RWGS reaction over the catalysts. The synergy of photoheating and reactant activation by hot carriers on the active Cu NPs may lead to a promoted CO production from RWGS reaction under light irradiation.

**Chapter 3 Metal oxide-modified Cu/MgO-$Al_2O_3$ catalyst for efficient and stable photothermal catalytic $CO_2$ conversion**

The long-term stability of catalysts is an important factor for further application. For

photothermal catalytic $CO_2$ hydrogenation process, the relatively high temperature and $H_2O$ generated in the process present a great challenge for the development of catalysts with long-term stability. One universal strategy to enhance the stability of catalyst is to fabricate metal-based catalysts with high dispersion via the modulation of the interaction between metal and oxide support, and the layer double hydroxide (LDH) has been reported to act as a platform to synthesize well dispersed metal/oxide nanocomposites with enhanced metal-support interactions. In addition, it is recently found that the hydrothermal stability of catalyst could be promoted by the addition of irreducible oxides on the surface, which inhibits the aggregation and deep oxidation of active metals in catalyst. Therefore, in this chapter, an efficient metal-oxide modified Cu/MgO-$Al_2O_3$ photothermal catalyst was synthesized with the elaborate design of the nanostructures derived from LDH and following impregnation. It is expected that the catalyst can achieve a high dispersion and stable nanostructures of Cu species, and exhibit not only efficient activity of CO production but also a long-term stability in the photothermal catalytic $CO_2$ hydrogenation.

**Chapter 4 Photothermal catalytic $CO_2$ hydrogenation to methanol over Ru/$In_2O_3$ catalysts under atmospheric pressure**

Under the mild reaction conditions, especially the ambient pressure, photothermal catalytic $CO_2$ hydrogenation usually generates CO or $CH_4$ as product. Considering the values of products, solar methanol ($CH_3OH$) production from $CO_2$ hydrogenation using renewable $H_2$ is considered to be a more efficient technique for $CO_2$ utilization. However, until now, very few works have been reported on photothermal methanol production under mild conditions, especially at ambient pressure. In addition, both activity and selectivity in these reports are still relatively low, inhibiting the further application of photothermal methanol production from $CO_2$ hydrogenation, and the detailed mechanism still requires thorough investigation and discussion. In this chapter, in order to convert $CO_2$ to $CH_3OH$ at mild conditions, a series of Ru/$In_2O_3$ catalysts were synthesized for photothermal methanol production from $CO_2$ hydrogenation under atmospheric pressure. Due to the interaction between active Ru NPs and oxygen

vacancies on $In_2O_3$, it is expected that the catalyst will show a good performance for methanol generation from $CO_2$ hydrogenation. DFT calculations were conducted to investigate the mechanism of photothermal $CO_2$ conversion to methanol.

**Chapter 5 General conclusion and future prospects**

This chapter makes an overall summary of the achievements in this dissertation and depicts the prospects for future research.

## References

[1] B.M. Bhanage, M. Arai, Transformation and utilization of carbon dioxide, Springer, 2014.

[2] C. Zou, B. Xiong, H. Xue, D. Zheng, Z. Ge, Y. Wang, L. Jiang, S. Pan, S. Wu, The role of new energy in carbon neutral, Petroleum Exploration and Development, 48 (2021) 480-491.

[3] O.S. Bushuyev, P. De Luna, C.T. Dinh, L. Tao, G. Saur, J. van de Lagemaat, S.O. Kelley, E.H. Sargent, What Should We Make with $CO_2$ and How Can We Make It?, Joule, 2 (2018) 825-832.

[4] N. Mac Dowell, P.S. Fennell, N. Shah, G.C. Maitland, The role of $CO_2$ capture and utilization in mitigating climate change, Nature Climate Change, 7 (2017) 243-249.

[5] T. Terlouw, C. Bauer, L. Rosa, M. Mazzotti, Life cycle assessment of carbon dioxide removal technologies: a critical review, Energy & Environmental Science, 14 (2021) 1701-1721.

[6] IEA (2022), Global Energy Review: $CO_2$ Emissions in 2021, IEA, Paris https://www.iea.org/reports/global-energy-review-co2-emissions-in-2021-2.

[7] J.e. al., CarbonTracker CT-NRT.v2022-1 (https://gml.noaa.gov/ccgg/trends/global.html), (2022).

[8] M.R. Smith, S.S. Myers, Impact of anthropogenic $CO_2$ emissions on global human nutrition, Nature Climate Change, 8 (2018) 834-839.

[9] C. Le Quéré, M.R. Raupach, J.G. Canadell, G. Marland, L. Bopp, P. Ciais, T.J. Conway, S.C. Doney, R.A. Feely, P. Foster, Trends in the sources and sinks of carbon

dioxide, Nature Geoscience, 2 (2009) 831-836.

[10] V. Romanov, Y. Soong, C. Carney, G.E. Rush, B. Nielsen, W. O'Connor, Mineralization of carbon dioxide: a literature review, ChemBioEng Reviews, 2 (2015) 231-256.

[11] C. Hepburn, E. Adlen, J. Beddington, E.A. Carter, S. Fuss, N. Mac Dowell, J.C. Minx, P. Smith, C.K. Williams, The technological and economic prospects for $CO_2$ utilization and removal, Nature, 575 (2019) 87-97.

[12] J. Beddington, E. Williams, Dealing with Carbon Dioxide at Scale, National Academy of Sciences, 2017.

[13] F. Raganati, F. Miccio, P. Ammendola, Adsorption of carbon dioxide for post-combustion capture: a review, Energy & Fuels, 35 (2021) 12845-12868.

[14] W. Gao, S. Liang, R. Wang, Q. Jiang, Y. Zhang, Q. Zheng, B. Xie, C.Y. Toe, X. Zhu, J. Wang, Industrial carbon dioxide capture and utilization: state of the art and future challenges, Chem. Soc. Rev., 49 (2020) 8584-8686.

[15] M.D. Zoback, S.M. Gorelick, Earthquake triggering and large-scale geologic storage of carbon dioxide, Proceedings of the National Academy of Sciences, 109 (2012) 10164-10168.

[16] S.M. Benson, T. Surles, Carbon dioxide capture and storage: An overview with emphasis on capture and storage in deep geological formations, Proc. IEEE, 94 (2006) 1795-1805.

[17] H. de Coninck, S.M. Benson, Carbon dioxide capture and storage: issues and prospects, Annual review of environment and resources, 39 (2014) 243-270.

[18] M.D. Aminu, S.A. Nabavi, C.A. Rochelle, V. Manovic, A review of developments in carbon dioxide storage, Applied Energy, 208 (2017) 1389-1419.

[19] Z. Zhang, S.-Y. Pan, H. Li, J. Cai, A.G. Olabi, E.J. Anthony, V. Manovic, Recent advances in carbon dioxide utilization, Renewable and sustainable energy reviews, 125 (2020) 109799.

[20] A. Dibenedetto, F. Nocito, The future of carbon dioxide chemistry, ChemSusChem, 13 (2020) 6219-6228.

[21] A.D.N. Kamkeng, M. Wang, J. Hu, W. Du, F. Qian, Transformation technologies

for $CO_2$ utilisation: Current status, challenges and future prospects, Chem. Eng. J., 409 (2021) 128138.

[22] T.M. Gür, Carbon dioxide emissions, capture, storage and utilization: Review of materials, processes and technologies, Prog. Energy Combust. Sci., 89 (2022) 100965.

[23] O. Hakami, Thermocatalytic and solar thermochemical carbon dioxide utilization to solar fuels and chemicals: A review, International Journal of Energy Research, (2022).

[24] Z.J. Wang, H. Song, H. Liu, J. Ye, Coupling of Solar Energy and Thermal Energy for Carbon Dioxide Reduction: Status and Prospects, Angew. Chem. Int. Ed. Engl., 59 (2020) 8016-8035.

[25] X. Jiang, X. Nie, X. Guo, C. Song, J.G. Chen, Recent Advances in Carbon Dioxide Hydrogenation to Methanol via Heterogeneous Catalysis, Chem. Rev., 120 (2020) 7984-8034.

[26] H. Song, X. Meng, T.D. Dao, W. Zhou, H. Liu, L. Shi, H. Zhang, T. Nagao, T. Kako, J. Ye, Light-Enhanced Carbon Dioxide Activation and Conversion by Effective Plasmonic Coupling Effect of Pt and Au Nanoparticles, ACS Appl Mater Interfaces, 10 (2018) 408-416.

[27] A.G. Variar, M. Ramyashree, V.U. Ail, K. Sudhakar, M. Tahir, Influence of various operational parameters in enhancing photocatalytic reduction efficiency of carbon dioxide in a photoreactor: A review, Journal of Industrial and Engineering Chemistry, 99 (2021) 19-47.

[28] T.N. Nguyen, Z. Chen, A.S. Zeraati, H.S. Shiran, S.M. Sadaf, M.G. Kibria, E.H. Sargent, C.-T. Dinh, Catalyst Regeneration via Chemical Oxidation Enables Long-Term Electrochemical Carbon Dioxide Reduction, J. Am. Chem. Soc., 144 (2022) 13254-13265.

[29] M. Ghoussoub, M. Xia, P.N. Duchesne, D. Segal, G. Ozin, Principles of photothermal gas-phase heterogeneous $CO_2$ catalysis, Energy & Environmental Science, 12 (2019) 1122-1142.

[30] H. Tong, S. Ouyang, Y. Bi, N. Umezawa, M. Oshikiri, J. Ye, Nano-photocatalytic materials: possibilities and challenges, Adv. Mater., 24 (2012) 229-251.

[31] S. Luo, X. Ren, H. Lin, H. Song, J. Ye, Plasmonic photothermal catalysis for solar-to-fuel conversion: current status and prospects, Chem Sci, 12 (2021) 5701-5719.

[32] F. Zhang, Y.-H. Li, M.-Y. Qi, Y.M.A. Yamada, M. Anpo, Z.-R. Tang, Y.-J. Xu, Photothermal catalytic $CO_2$ reduction over nanomaterials, Chem Catalysis, 1 (2021) 272-297.

[33] C. Xu, X. Zhang, M.-N. Zhu, L. Zhang, P.-F. Sui, R. Feng, Y. Zhang, J.-L. Luo, Accelerating photoelectric $CO_2$ conversion with a photothermal wavelength-dependent plasmonic local field, Applied Catalysis B: Environmental, 298 (2021) 120533.

[34] S. Khan, X. Dai, T. Ali, S. Mahmood, M.u. Haq, M.S. Riaz, Y. Hu, Recent advances on photo-thermo-catalysis for carbon dioxide methanation, Int. J. Hydrogen Energy, (2022).

[35] M.L. Brongersma, N.J. Halas, P. Nordlander, Plasmon-induced hot carrier science and technology, Nat Nanotechnol, 10 (2015) 25-34.

[36] C. Xu, J. Hong, P. Sui, M. Zhu, Y. Zhang, J.-L. Luo, Standalone Solar Carbon-Based Fuel Production Based on Semiconductors, Cell Reports Physical Science, 1 (2020) 100101.

[37] C. Xu, Y. Zhang, J. Chen, J. Lin, X. Zhang, Z. Wang, J. Zhou, Enhanced mechanism of the photo-thermochemical cycle based on effective Fe-doping $TiO_2$ films and DFT calculations, Applied Catalysis B: Environmental, 204 (2017) 324-334.

[38] D. Mateo, J.L. Cerrillo, S. Durini, J. Gascon, Fundamentals and applications of photo-thermal catalysis, Chem. Soc. Rev., 50 (2021) 2173-2210.

[39] P. Christopher, H. Xin, S. Linic, Visible-light-enhanced catalytic oxidation reactions on plasmonic silver nanostructures, Nature Chemistry, 3 (2011) 467-472.

[40] X. Meng, T. Wang, L. Liu, S. Ouyang, P. Li, H. Hu, T. Kako, H. Iwai, A. Tanaka, J. Ye, Photothermal conversion of $CO_2$ into $CH_4$ with $H_2$ over Group VIII nanocatalysts: an alternative approach for solar fuel production, Angew. Chem. Int. Ed., 53 (2014) 11478-11482.

[41] H. Song, X. Meng, Z.-j. Wang, H. Liu, J. Ye, Solar-Energy-Mediated Methane Conversion, Joule, 3 (2019) 1606-1636.

[42] H. Villafán-Vidales, C. Arancibia-Bulnes, D. Riveros-Rosas, H. Romero-Paredes,

C. Estrada, An overview of the solar thermochemical processes for hydrogen and syngas production: Reactors, and facilities, Renewable and Sustainable Energy Reviews, 75 (2017) 894-908.

[43] E. Cortes, F.J. Wendisch, L. Sortino, A. Mancini, S. Ezendam, S. Saris, S.M.L. de, A. Tittl, H. Ren, S.A. Maier, Optical Metasurfaces for Energy Conversion, Chem. Rev., 122 (2022) 15082-15176.

[44] G. Baffou, R. Quidant, Nanoplasmonics for chemistry, Chem. Soc. Rev., 43 (2014) 3898-3907.

[45] G. Baffou, F. Cichos, R. Quidant, Applications and challenges of thermoplasmonics, Nature Materials, 19 (2020) 946-958.

[46] L. Zhou, D.F. Swearer, C. Zhang, H. Robatjazi, H. Zhao, L. Henderson, L. Dong, P. Christopher, E.A. Carter, P. Nordlander, Quantifying hot carrier and thermal contributions in plasmonic photocatalysis, Science, 362 (2018) 69-72.

[47] U. Aslam, V.G. Rao, S. Chavez, S. Linic, Catalytic conversion of solar to chemical energy on plasmonic metal nanostructures, Nature Catalysis, 1 (2018) 656-665.

[48] S. Kattel, P. Liu, J.G. Chen, Tuning Selectivity of $CO_2$ Hydrogenation Reactions at the Metal/Oxide Interface, J. Am. Chem. Soc., 139 (2017) 9739-9754.

[49] S. Ning, Y. Sun, S. Ouyang, Y. Qi, J. Ye, Solar light-induced injection of hot electrons and photocarriers for synergistically enhanced photothermocatalysis over Cu-Co/$SrTiO_3$ catalyst towards boosting CO hydrogenation into $C_2$–$C_4$ hydrocarbons, Applied Catalysis B: Environmental, 310 (2022) 121063.

[50] K.K. Ghuman, T.E. Wood, L.B. Hoch, C.A. Mims, G.A. Ozin, C.V. Singh, Illuminating $CO_2$ reduction on frustrated Lewis pair surfaces: investigating the role of surface hydroxides and oxygen vacancies on nanocrystalline $In_2O_{3-x}(OH)_y$, PCCP, 17 (2015) 14623-14635.

[51] L.B. Hoch, P.G. O'Brien, A. Jelle, A. Sandhel, D.D. Perovic, C.A. Mims, G.A. Ozin, Nanostructured Indium Oxide Coated Silicon Nanowire Arrays: A Hybrid Photothermal/Photochemical Approach to Solar Fuels, ACS Nano, 10 (2016) 9017-9025.

[52] L. He, T.E. Wood, B. Wu, Y. Dong, L.B. Hoch, L.M. Reyes, D. Wang, C. Kübel,

C. Qian, J. Jia, K. Liao, P.G. O'Brien, A. Sandhel, J.Y.Y. Loh, P. Szymanski, N.P. Kherani, T.C. Sum, C.A. Mims, G.A. Ozin, Spatial Separation of Charge Carriers in $In_2O_{3-x}(OH)_y$ Nanocrystal Superstructures for Enhanced Gas-Phase Photocatalytic Activity, ACS Nano, 10 (2016) 5578-5586.

[53] Y. Qi, L. Song, S. Ouyang, X. Liang, S. Ning, Q. Zhang, J. Ye, Photoinduced Defect Engineering: Enhanced Photothermal Catalytic Performance of 2D Black $In_2O_{3-x}$ Nanosheets with Bifunctional Oxygen Vacancies, Adv. Mater., 32 (2020) e1903915.

[54] J. Jia, P.G. O'Brien, L. He, Q. Qiao, T. Fei, L.M. Reyes, T.E. Burrow, Y. Dong, K. Liao, M. Varela, S.J. Pennycook, M. Hmadeh, A.S. Helmy, N.P. Kherani, D.D. Perovic, G.A. Ozin, Visible and Near-Infrared Photothermal Catalyzed Hydrogenation of Gaseous $CO_2$ over Nanostructured $Pd@Nb_2O_5$, Advanced Science, 3 (2016) 1600189.

[55] C. Kim, S. Hyeon, J. Lee, W.D. Kim, D.C. Lee, J. Kim, H. Lee, Energy-efficient $CO_2$ hydrogenation with fast response using photoexcitation of $CO_2$ adsorbed on metal catalysts, Nature Communications, 9 (2018) 3027.

[56] D. Vovchok, C. Zhang, S. Hwang, L. Jiao, F. Zhang, Z. Liu, S.D. Senanayake, J.A. Rodriguez, Deciphering Dynamic Structural and Mechanistic Complexity in $Cu/CeO_2$/ZSM-5 Catalysts for the Reverse Water-Gas Shift Reaction, ACS Catalysis, 10 (2020) 10216-10228.

[57] J. Guo, P.N. Duchesne, L. Wang, R. Song, M. Xia, U. Ulmer, W. Sun, Y. Dong, J.Y.Y. Loh, N.P. Kherani, J. Du, B. Zhu, W. Huang, S. Zhang, G.A. Ozin, High-Performance, Scalable, and Low-Cost Copper Hydroxyapatite for Photothermal $CO_2$ Reduction, ACS Catalysis, 10 (2020) 13668-13681.

[58] X. Chen, Q. Li, M. Zhang, J. Li, S. Cai, J. Chen, H. Jia, MOF-Templated Preparation of Highly Dispersed $Co/Al_2O_3$ Composite as the Photothermal Catalyst with High Solar-to-Fuel Efficiency for $CO_2$ Methanation, ACS Appl Mater Interfaces, 12 (2020) 39304-39317.

[59] H. Robatjazi, H. Zhao, D.F. Swearer, N.J. Hogan, L. Zhou, A. Alabastri, M.J. McClain, P. Nordlander, N.J. Halas, Plasmon-induced selective carbon dioxide conversion on earth-abundant aluminum-cuprous oxide antenna-reactor nanoparticles, Nature Communications, 8 (2017) 27.

[60] H. Zhang, T. Wang, J. Wang, H. Liu, T.D. Dao, M. Li, G. Liu, X. Meng, K. Chang, L. Shi, T. Nagao, J. Ye, Surface-Plasmon-Enhanced Photodriven $CO_2$ Reduction Catalyzed by Metal–Organic-Framework-Derived Iron Nanoparticles Encapsulated by Ultrathin Carbon Layers, Adv. Mater., 28 (2016) 3703-3710.

[61] S. Ning, H. Xu, Y. Qi, L. Song, Q. Zhang, S. Ouyang, J. Ye, Microstructure Induced Thermodynamic and Kinetic Modulation to Enhance $CO_2$ Photothermal Reduction: A Case of Atomic-Scale Dispersed Co–N Species Anchored Co@C Hybrid, ACS Catalysis, 10 (2020) 4726-4736.

[62] Y.F. Li, W. Lu, K. Chen, P. Duchesne, A. Jelle, M. Xia, T.E. Wood, U. Ulmer, G.A. Ozin, Cu Atoms on Nanowire Pd/$H_yWO_{3-x}$ Bronzes Enhance the Solar Reverse Water Gas Shift Reaction, J. Am. Chem. Soc., 141 (2019) 14991-14996.

[63] L. Wan, Q. Zhou, X. Wang, T.E. Wood, L. Wang, P.N. Duchesne, J. Guo, X. Yan, M. Xia, Y.F. Li, A.A. Jelle, U. Ulmer, J. Jia, T. Li, W. Sun, G.A. Ozin, $Cu_2O$ nanocubes with mixed oxidation-state facets for (photo)catalytic hydrogenation of carbon dioxide, Nature Catalysis, 2 (2019) 889-898.

[64] B. Lu, F. Quan, Z. Sun, F. Jia, L. Zhang, Photothermal reverse-water-gas-shift over Au/$CeO_2$ with high yield and selectivity in $CO_2$ conversion, Catal. Commun., 129 (2019) 105724.

[65] C. Wang, S. Fang, S. Xie, Y. Zheng, Y.H. Hu, Thermo-photo catalytic $CO_2$ hydrogenation over Ru/$TiO_2$, Journal of Materials Chemistry A, 8 (2020) 7390-7394.

[66] Y. Zhao, X. Jia, G.I.N. Waterhouse, L.-Z. Wu, C.-H. Tung, D. O'Hare, T. Zhang, Layered Double Hydroxide Nanostructured Photocatalysts for Renewable Energy Production, Advanced Energy Materials, 6 (2016) 1501974.

[67] Z. Yuan, L. Wang, J. Wang, S. Xia, P. Chen, Z. Hou, X. Zheng, Hydrogenolysis of glycerol over homogenously dispersed copper on solid base catalysts, Applied Catalysis B: Environmental, 101 (2011) 431-440.

[68] J. Ren, S. Ouyang, H. Xu, X. Meng, T. Wang, D. Wang, J. Ye, Targeting Activation of $CO_2$ and $H_2$ over Ru-Loaded Ultrathin Layered Double Hydroxides to Achieve Efficient Photothermal $CO_2$ Methanation in Flow-Type System, Advanced Energy Materials, 7 (2017) 1601657.

[69] G. Chen, R. Gao, Y. Zhao, Z. Li, G.I.N. Waterhouse, R. Shi, J. Zhao, M. Zhang, L. Shang, G. Sheng, X. Zhang, X. Wen, L.-Z. Wu, C.-H. Tung, T. Zhang, Alumina-Supported CoFe Alloy Catalysts Derived from Layered-Double-Hydroxide Nanosheets for Efficient Photothermal $CO_2$ Hydrogenation to Hydrocarbons, Advanced Materials, 30 (2018) 1704663.

[70] Z. Li, R. Shi, J. Zhao, T. Zhang, Ni-based catalysts derived from layered-double-hydroxide nanosheets for efficient photothermal $CO_2$ reduction under flow-type system, Nano Research, 14 (2021) 4828-4832.

[71] Y. Xiong, H. Chen, Y. Hu, S. Yang, X. Xue, L. He, X. Liu, J. Ma, Z. Jin, Photodriven Catalytic Hydrogenation of $CO_2$ to $CH_4$ with Nearly 100% Selectivity over $Ag_{25}$ Clusters, Nano Lett., 21 (2021) 8693-8700.

[72] X. Zhang, H. Liu, Y. Wang, S. Yang, Q. Chen, Z. Zhao, Y. Yang, Q. Kuang, Z. Xie, Hot-electron-induced $CO_2$ hydrogenation on Au@AuRu/g-$C_3N_4$ plasmonic bimetal–semiconductor heterostructure, Chem. Eng. J., 443 (2022) 136482.

[73] R. Tang, H. Sun, Z. Zhang, L. Liu, F. Meng, X. Zhang, W. Yang, Z. Li, Z. Zhao, R. Zheng, J. Huang, Incorporating plasmonic Au-nanoparticles into three-dimensionally ordered macroporous perovskite frameworks for efficient photocatalytic $CO_2$ reduction, Chem. Eng. J., 429 (2022) 132137.

[74] Z. Zhang, Z. Wang, S.-W. Cao, C. Xue, Au/Pt Nanoparticle-Decorated $TiO_2$ Nanofibers with Plasmon-Enhanced Photocatalytic Activities for Solar-to-Fuel Conversion, The Journal of Physical Chemistry C, 117 (2013) 25939-25947.

[75] M. Tahir, B. Tahir, N.A.S. Amin, Synergistic effect in plasmonic Au/Ag alloy NPs co-coated $TiO_2$ NWs toward visible-light enhanced $CO_2$ photoreduction to fuels, Applied Catalysis B: Environmental, 204 (2017) 548-560.

[76] G. Baffou, R. Quidant, Thermo-plasmonics: using metallic nanostructures as nano-sources of heat, Laser & Photonics Reviews, 7 (2013) 171-187.

[77] M.W. Knight, L. Liu, Y. Wang, L. Brown, S. Mukherjee, N.S. King, H.O. Everitt, P. Nordlander, N.J. Halas, Aluminum plasmonic nanoantennas, Nano Lett., 12 (2012) 6000-6004.

[78] P. Martínez Molina, N. Meulendijks, M. Xu, M.A. Verheijen, T. den Hartog, P.

Buskens, F. Sastre, Low Temperature Sunlight-Powered Reduction of $CO_2$ to CO Using a Plasmonic Au/$TiO_2$ Nanocatalyst, ChemCatChem, 13 (2021) 4507-4513.

[79] P. Qiao, B. Sun, H. Li, K. Pan, G. Tian, L. Wang, W. Zhou, Surface Plasmon Resonance-Enhanced Visible-NIR-Driven Photocatalytic and Photothermal Catalytic Performance by Ag/Mesoporous Black $TiO_2$ Nanotube Heterojunctions, Chemistry – An Asian Journal, 14 (2019) 177-186.

[80] J.N.G. Stanley, I. García-García, T. Perfrement, E.C. Lovell, T.W. Schmidt, J. Scott, R. Amal, Plasmonic effects on $CO_2$ reduction over bimetallic Ni-Au catalysts, Chem. Eng. Sci., 194 (2019) 94-104.

[81] G. Fu, M. Jiang, J. Liu, K. Zhang, Y. Hu, Y. Xiong, A. Tao, Z. Tie, Z. Jin, Rh/Al Nanoantenna Photothermal Catalyst for Wide-Spectrum Solar-Driven $CO_2$ Methanation with Nearly 100% Selectivity, Nano Lett., 21 (2021) 8824-8830.

[82] B. An, J. Zhang, K. Cheng, P. Ji, C. Wang, W. Lin, Confinement of Ultrasmall Cu/ZnOx Nanoparticles in Metal-Organic Frameworks for Selective Methanol Synthesis from Catalytic Hydrogenation of $CO_2$, J. Am. Chem. Soc., 139 (2017) 3834-3840.

[83] G. Wang, C.T. He, R. Huang, J. Mao, D. Wang, Y. Li, Photoinduction of Cu Single Atoms Decorated on UiO-66-$NH_2$ for Enhanced Photocatalytic Reduction of $CO_2$ to Liquid Fuels, J. Am. Chem. Soc., 142 (2020) 19339-19345.

[84] W.-G. Cui, G.-Y. Zhang, T.-L. Hu, X.-H. Bu, Metal-organic framework-based heterogeneous catalysts for the conversion of C1 chemistry: CO, $CO_2$ and $CH_4$, Coord. Chem. Rev., 387 (2019) 79-120.

[85] F. Wang, J. Tian, M. Li, W. Li, L. Chen, X. Liu, J. Li, A. Muhetaer, Q. Li, Y. Wang, L. Gu, D. Ma, D. Xu, A Photoactivated Cu-$CeO_2$ Catalyst with Cu-[O]-Ce Active Species Designed through MOF Crystal Engineering, Angew. Chem. Int. Ed. Engl., 59 (2020) 8203-8209.

[86] A. Dhabi., Innovation Outlook: Renewable Methanol, IRENA AND METHANOL INSTITUTE, (2021).

[87] G.A. Olah, Beyond Oil and Gas: The Methanol Economy, Angew. Chem. Int. Ed., 44 (2005) 2636-2639.

[88] N. Podrojková, V. Sans, A. Oriňak, R. Oriňaková, Recent Developments in the Modelling of Heterogeneous Catalysts for $CO_2$ Conversion to Chemicals, ChemCatChem, 12 (2020) 1802-1825.

[89] J.W. Ager, A.A. Lapkin, Chemical storage of renewable energy, Science, 360 (2018) 707.

[90] L. Wang, M. Ghoussoub, H. Wang, Y. Shao, W. Sun, A.A. Tountas, T.E. Wood, H. Li, J.Y.Y. Loh, Y. Dong, M. Xia, Y. Li, S. Wang, J. Jia, C. Qiu, C. Qian, N.P. Kherani, L. He, X. Zhang, G.A. Ozin, Photocatalytic Hydrogenation of Carbon Dioxide with High Selectivity to Methanol at Atmospheric Pressure, Joule, 2 (2018) 1369-1381.

[91] W. Wei, Z. Wei, R. Li, Z. Li, R. Shi, S. Ouyang, Y. Qi, D.L. Philips, H. Yuan, Subsurface oxygen defects electronically interacting with active sites on $In_2O_3$ for enhanced photothermocatalytic $CO_2$ reduction, Nat Commun, 13 (2022) 3199.

[92] L. Wang, Y. Dong, T. Yan, Z. Hu, A.A. Jelle, D.M. Meira, P.N. Duchesne, J.Y.Y. Loh, C. Qiu, E.E. Storey, Y. Xu, W. Sun, M. Ghoussoub, N.P. Kherani, A.S. Helmy, G.A. Ozin, Black indium oxide a photothermal $CO_2$ hydrogenation catalyst, Nat Commun, 11 (2020) 2432.

[93] T. Yan, N. Li, L. Wang, W. Ran, P.N. Duchesne, L. Wan, N.T. Nguyen, L. Wang, M. Xia, G.A. Ozin, Bismuth atom tailoring of indium oxide surface frustrated Lewis pairs boosts heterogeneous $CO_2$ photocatalytic hydrogenation, Nat Commun, 11 (2020) 6095.

[94] J. Zhu, F. Cannizzaro, L. Liu, H. Zhang, N. Kosinov, I.A.W. Filot, J. Rabeah, A. Bruckner, E.J.M. Hensen, Ni-In Synergy in $CO_2$ Hydrogenation to Methanol, ACS Catal, 11 (2021) 11371-11384.

[95] P. Chang, Y. Wang, Y. Wang, Y. Zhu, Current trends on $In_2O_3$ based heterojunction photocatalytic systems in photocatalytic application, Chem. Eng. J., 450 (2022) 137804.

[96] Z.-j. Wang, H. Song, H. Pang, Y. Ning, T.D. Dao, Z. Wang, H. Chen, Y. Weng, Q. Fu, T. Nagao, Y. Fang, J. Ye, Photo-assisted methanol synthesis via $CO_2$ reduction under ambient pressure over plasmonic Cu/ZnO catalysts, Applied Catalysis B: Environmental, 250 (2019) 10-16.

[97] B. Xie, R.J. Wong, T.H. Tan, M. Higham, E.K. Gibson, D. Decarolis, J. Callison, K.-F. Aguey-Zinsou, M. Bowker, C.R.A. Catlow, Synergistic ultraviolet and visible light photo-activation enables intensified low-temperature methanol synthesis over copper/zinc oxide/alumina, Nature communications, 11 (2020) 1-11.

[98] W. Zhang, L. Wang, K. Wang, M.U. Khan, M. Wang, H. Li, J. Zeng, Integration of Photothermal Effect and Heat Insulation to Efficiently Reduce Reaction Temperature of $CO_2$ Hydrogenation, Small, 13 (2017) 1602583.

[99] L. Liu, A.V. Puga, J. Cored, P. Concepción, V. Pérez-Dieste, H. García, A. Corma, Sunlight-assisted hydrogenation of $CO_2$ into ethanol and C2+ hydrocarbons by sodium-promoted Co@C nanocomposites, Applied Catalysis B: Environmental, 235 (2018) 186-196.

# Chapter 2 Metal-Organic Framework-Derived Ga-Cu/$CeO_2$ catalyst for highly efficient photothermal catalytic $CO_2$ reduction

## 2.1 Introduction

Nowadays, the enormous energy demands of human society require a large-scale consumption of fossil fuels, resulting in an immense $CO_2$ emission.[1] The average concentration of $CO_2$ in the atmosphere has increased dramatically over the past several decades and reached 417 ppm in 2021, which has aroused worldwide concerns due to its foreseeable effect on global climate change.[2, 3] One of the promising approaches to mitigate the energy and environmental problems is utilizing renewable energy to produce value-added fuels and chemicals from $CO_2$ as a carbon source, paving the road towards a global carbon balance.[4-6] Solar-driven gas-phase $CO_2$ reduction to CO with renewable $H_2$, also known as reverse water gas shift reaction (RWGS, $CO_2 + H_2 \rightarrow CO + H_2O$), has attracted enormous research attention, due to the high demand for CO in the synthesis of high value-added chemical products in the modern chemical industry.[7-11] Most of solar light is made up of visible and infrared (IR) light, and ultraviolet (UV) light only accounts for 4%. In conventional photocatalysis, only UV and part of visible light could be harvested, thus wasting a lot of energy.[12, 13] To maximize the solar light utilization efficiency, photothermal catalysis mainly based on plasmonic metal catalysts such as Au, Ag and Cu has emerged as a promising way to drive catalytic reactions by utilizing the full wavelength range of the solar spectrum, especially the low-energy IR light.[14-18] The elevated surface temperatures of catalysts caused by photothermal heating and photoactivation from hot carriers play critical roles in photothermal catalytic reactions.[12, 19, 20] As a result, photothermal catalysis shows much higher performances than semiconductor-based photocatalysis and delivers identical performances under lower temperatures compared with pure thermal catalysis, which

could alleviate catalyst deactivation caused by metal aggregation at high temperatures.[21]

Cu, the abundant and low-cost metal, is among the most catalytically active catalysts for RWGS reaction at atmosphere pressure.[22, 23] However, the endothermic feature of reaction requires a relatively high temperature for significant conversion of $CO_2$ on Cu based catalysts, compared with noble metal (Pt, Pd, etc.), resulting in the fast deactivation of catalysts.[24] Previous studies show that the high dispersion of Cu could enhance catalytic activity in RWGS reaction at relatively low reaction temperature.[25-27] Recently, metal-organic frameworks (MOFs) have been employed as a platform for the synthesis of well-dispersed metal-based catalysts to avoid the aggregation of metal catalysts due to the well-separated metal ions by the organic linkers.[2, 28-30] Relative works have verified that metal oxide catalysts derived from MOF precursors show improved physicochemical properties, promoted metal-support interactions and enhanced activity in various catalysis.[31, 32] In addition, $CeO_2$ is an excellent support to stabilize and well disperse the loading metals and produce strong metal-support interactions due to its unique redox properties.[33] Moreover, to further enhance the activity of Cu-based catalysts, several research groups have investigated the utilization of Ga as a promoter in $CO_2$ hydrogenation, such as $Cu/ZnO/Ga_2O_3$, $Cu/Al_2O_3/Ga_2O_3$, $CuGa/SiO_2$.[34-36] Therefore, the rational design of $CeO_2$ supported highly dispersed Cu and Ga catalysts is expected as a promising approach for efficient photothermal RWGS, but yet remains mostly unexplored.

Herein, I employ a MOF-templated approach to prepare a series of well-dispersed $Ga\text{-}Cu/CeO_2$ catalysts and carries out photothermal gas-phase RWGS reaction over these catalysts. Due to the highly dispersed Cu and Ga as well as the synergistic effect of photothermal heating and light promoting, the obtained catalysts show greatly enhanced activity compared with the catalysts synthesized by impregnation method. The optimized catalyst gives rise to a high CO production rate of 111.2 $mmol \cdot g^{-1} \cdot h^{-1}$ with almost 100% selectivity under light irradiation, exceeding most reported Cu and

other earth-abundant metals-based catalysts for photothermal $CO_2$ reduction under similar reaction conditions.

## 2.2 Experimental section

### 2.2.1 Materials

All chemicals were used as received without further purification. Copper(II) nitrate trihydrate ($Cu(NO_3)_2 \cdot 3H_2O$), cerium(III) nitrate hexahydrate ($Ce(NO_3)_3 \cdot 6H_2O$), gallium(III) nitrate hydrate ($Ga(NO_3)_3 \cdot nH_2O$, n=7~9), zinc(II) nitrate hexahydrate ($Zn(NO_3)_2 \cdot 6H_2O$), aluminum(III) nitrate nonahydrate ($Al(NO_3)_3 \cdot 9H_2O$), sodium carbonate ($Na_2CO_3$), 1,3,5-Benzenetricarboxylic acid (BTC), methanol, ethanol were supplied by Wako Chemical Co., Ltd. Ultrapure water (18.2 MΩ cm) was used in all experiments.

### 2.2.2 Catalysts preparation

***Synthesis of Ce-BTC.*** The detailed method for the preparation of Ce-BTC is similar to previous work.[32] Briefly, 3 mmol $Ce(NO_3)_3 \cdot 6H_2O$ and 3 mmol BTC were dissolved in 120 mL methanol/ethanol (v:v=1:1). 60 mL ultrapure water was then quickly added into the above solution under vigorously stirring. After 20 min stirring, the mixture was centrifuged and washed with ethanol and dried in a vacuum oven at 70 $^oC$ overnight.

***Synthesis of Cu/Ga/Ce-BTC precursor.*** The Cu/Ga/Ce-BTC precursor was prepared via ion-exchange method. 0.2 g Ce-BTC and a certain amount of $Cu(NO_3)_2 \cdot 3H_2O$ and $Ga(NO_3)_3 \cdot nH_2O$ were dissolved in 2.88 mL and 3.66 mL methanol, respectively. Then the copper and gallium solution were added into the Ce-BTC suspension under ultrasonic conduction. The mixture formed gel-like solid and stood for 20 min after 15 s sonication. Then the suspension was centrifuged and washed with ethanol and water. The Cu/Ga/Ce-BTC was dried in a vacuum oven at 70 $^oC$ overnight.

***Synthesis of Cu/Ga/$CeO_2$ catalyst.*** The Cu/Ga/$CeO_2$ was obtained by calcinating the Cu/Ga/$CeO_2$ precursor at 500 $^oC$ in air for 2 h, and then reduced in a flow of 20% $H_2$/Ar

at 300 °C for 1 h. By adjusting the amount of copper and gallium nitrate added into the precursor, the Cu/Ga/$CeO_2$ samples with different metal contents were synthesized.

***Synthesis of reference catalysts.*** A reference catalyst was synthesized by wet-impregnation method in two steps. $CeO_2$ was obtained by calcinating Ce-BTC precursor in air at 500 °C for 2 h. Certain amount of $Cu(NO_3)_2 \cdot 3H_2O$ and $Ga(NO_3)_3 \cdot nH_2O$ was impregnated on $CeO_2$ followed by calcination in air at 500 °C for 2 h.

Another reference catalyst Cu/ZnO/$Al_2O_3$ was synthesized by coprecipitation according to the previous report.[37] Aqueous solution (50 ml) of metal nitrates [2.18 g of $Cu(NO_3)_2 \cdot 3H_2O$, 1.34 g of $Zn(NO_3)_2 \cdot 6H_2O$, and 0.56 g of $Al(NO_3)_3 \cdot 9H_2O$] and aqueous solution (60 ml) of 1.91 g of $Na_2CO_3$ as a precipitant were added dropwise (at a flow rate of 3 ml/min) to a glass reactor with a starting volume of 100 ml of deionized water under vigorous stirring at 70°C. Controlling the pH of precipitation mother liquor to 7, and aging the precipitate for 2 hours after precipitation, followed by cooling down to room temperature, filtering, and washing seven times with deionized water. The filter cake was dried at 80°C overnight and calcined at 350°C in static air for 3 hours.

### 2.2.3 Characterization

The Cu and Ga content in samples were analyzed via ICP-OES (Agilent 720-ES). The powder X-ray diffraction (XRD) patterns were recorded on a PANalytical B.V. XRD diffractometer (45 kV, 30 mA) with Cu Kα radiation (λ = 1.5406 Å). Transmission electron micrography (TEM) and high-resolution TEM (HRTEM) pictures were obtained on a JEOL JEM-F200 (HR) transmission electron microscopy operated at 200 kV. Energy-Dispersive X-ray spectroscopy (EDS) measurement was also conducted on the above TEM instrument. Information about surface area and porosity of catalysts were obtained by nitrogen adsorption at 77 K. UV-Visible diffuse reflectance spectroscopy (UV-Vis DRS) were collected by a Shimadzu UV-2500 spectrometer equipped with an integrating sphere accessory. X-ray photoelectron spectroscopy (XPS) was recorded on a Thermo Fisher ESCALAB Xi+ equipment. $H_2$-

TPR test was conducted on an AutoChem II 2920 chemisorption system. 50 mg catalyst was initially pretreated by Ar (20 mL $min^{-1}$) at 150 $^{o}$C for 1 h, followed by cooling down to 50 $^{o}$C. Then, 10%$H_2$/Ar (20 mL $min^{-1}$) was introduced to the system and the temperature increased from 50 $^{o}$C to 400 $^{o}$C with the ramping rate of 5 $^{o}$C $min^{-1}$.

### 2.2.4 Calculation of Cu dispersion by low temperature oxygen chemisorption

The dispersion of copper ($D_{Cu}$) was measured by low-temperature oxygen chemisorption method according to previous report.[38] Firstly, 50 mg catalyst was reduced by 10% $H_2$/Ar (20 mL $min^{-1}$) at 300 $^{o}$C for 1h. Then the catalyst was cooled in Ar atmosphere to 143 K for oxygen chemisorption. 1% $O_2$/Ar was employed as the pulse gas to oxidize just the surface Cu atoms into $Cu_2O$. After injecting eight times, $H_2$-TPR was carried out to reduce the freshly oxidized Cu surface and measure the quantity of surface Cu atoms. The $D_{Cu}$ was calculated by comparing the measured amount of surface Cu with the amount of bulk Cu, as measured by ICP.

### 2.2.5 Catalytic activity evaluation

Photothermal $CO_2$ reduction test was conducted in a home-made quartz reactor, and the schematic illustration is shown in Figure 2.1. The diameter of sample holder is 10 mm. A 300W Xenon arc lamp was utilized as the illuminant without any external heat input. The intensity of light was measured by a Thorlabs PM-100D optical power meter equipped with an S401C sensor. The detection range of wavelength is 190 – 20000 nm. In a typical test, 10 mg catalyst was first reduced in a flow of 20% $H_2$/Ar at 300 $^{o}$C for 1 h, and then spread on the round air-permeable quartz fiber filter in the reactor. The temperature of catalyst bed was monitored by a thermocouple located at the center of sample surface. Reaction gas mixture (volume ratio of 1:1 for $CO_2$/$H_2$) was introduced through the reactor with a flow rate of 20 mL $min^{-1}$. After 30 min purge, the lamp was turned on to start photothermal reaction. The output gas was analyzed by gas chromatography (Shimadzu GC2014) equipped with a flame ionization detector (FID) detector and two capillary columns (shincarbon-A and porapak-Q).

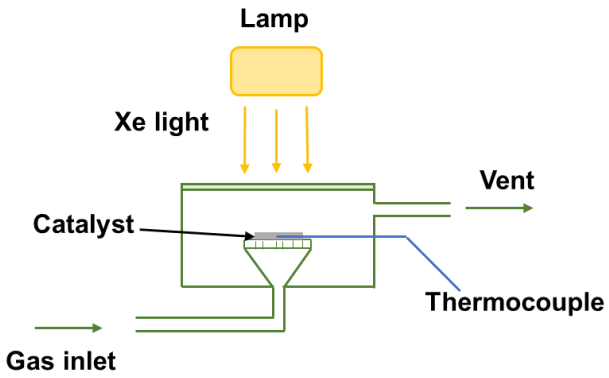


**Figure 2.1** Schematic illustration of home-made reactor for solar-driven $CO_2$ reduction.

The solar energy conversion efficiency (η) was calculated by the following formula[39]:

$$\eta = \frac{r(CO) \times \Delta_f H^0_{CO} + r(H_2O) \times \Delta_f H^0_{H_2O} - r(H_2) \times \Delta_f H^0_{H_2} - r(CO_2) \times \Delta_f H^0_{CO_2}}{P_{irradiation}} \times 100\%$$

where r(x) is the reaction rate of reactant or product x, and $\Delta_fH^0$ is relevant standard enthalpy of formation. $P_{irradiation}$ is the energy power of input light. The $\Delta_fH^0$ for CO, $H_2O$, $H_2$ and $CO_2$ are -110.6, -242, 0 and -393.8 kJ $mol^{-1}$. In this chapter, CO was the main product with almost 100% selectivity. Thus, the reaction speed of CO, $H_2O$, $H_2$ and $CO_2$ was considered to be identical for η calculation.

In order to investigate the effect of light on the catalytic activity, photo-assisted thermal $CO_2$ reduction experiment was conducted in a homemade stainless-steel flow-type reactor with external electrical heating, as shown in Figure 2.2. The sample holder was 8.5 mm in diameter. A LA-251 Xe lamp with a HA30 filter was utilized as UV-visible irradiation source. A thermocouple and temperature controller (TC-1000 JASCO) was used to maintain the catalyst temperature. Typically, 10 mg catalyst was smoothly spread onto the holder and reduced in 20% $H_2$/Ar at 300 °C for 1 h. After cooling down to room temperature, the gas was switched to 1/1 $CO_2/H_2$ gas mixture with a rate of 20 mL $min^{-1}$. Product detection was same as the photothermal $CO_2$ reduction test.

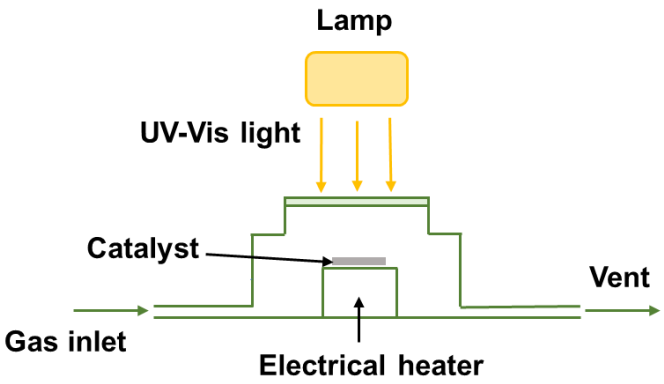


**Figure 2.2** Schematic illustration of home-made reactor for photo-assisted thermal catalytic $CO_2$ reduction.

### 2.2.6 In situ DRIFTS analysis

In situ diffuse reflectance infrared Fourier transform spectroscopy (DRIFTS) experiment was conducted on a JASCO FT-IR 6300 Spectrometers equipped with MCT detector and in situ diffuse reflectance cell. All spectra were collected with 32 scans at 4 $cm^{-1}$ resolution. Prior to experiment, 10 mg catalyst was in-situ reduced by 20%$H_2$/Ar at 300 $^oC$ for 1 h, and then cooled down to room temperature in Ar flow. After the background spectrum was obtained in 20 mL $min^{-1}$ Ar at 30 $^oC$, the gas flow was changed into 50% $CO_2$/50% $H_2$ (20 mL $min^{-1}$) and the reaction was performed under irradiation in the step heating to 100, 150, 200, 250, 300 $^oC$ with a ramping rate of 10 $^oC$ $min^{-1}$. Each temperature stage was maintained for 30 min.

To further investigate the mechanism of light enhancement in RWGS reaction, the DRIFTS spectra of reaction were recorded on the best sample both in dark and under irradiation. Typically, after the reduction of catalyst in $H_2$ atmosphere, 50% $CO_2$/50% $H_2$ (20 mL $min^{-1}$) gas mixture was introduced into the reaction cell. After the reactants were fully adsorbed on the catalyst, the gas input was closed and the infrared spectra were collected under irradiation at 250 $^oC$. In contrast, the spectra in dark were collected under the same condition without irradiation.

## 2.3 Results and discussion

### 2.3.1 Characterization of catalysts

In this chapter, Cu/Ga/$CeO_2$ catalysts were prepared based on Ce-BTC MOF with the incorporation of $Cu^{2+}$ and $Ga^{3+}$ ions. The precursors of Cu/Ga/$CeO_2$ catalysts were obtained through ion-exchange of $Cu^{2+}$ and $Ga^{3+}$ into Ce-BTC, followed by calcination in air at 500 $^oC$ and then reduced in $H_2$ at 300 $^oC$ to form Cu/Ga/$CeO_2$. The obtained catalysts were named as xCuyGa/$CeO_2$ (x, y was the designed weight percentage of Cu, Ga, respectively). In contrast, a reference sample was synthesized through wet impregnation of copper and gallium nitrate on $CeO_2$ obtained from calcination of Ce-BTC in air and was named as xCuyGa/$CeO_2$-w. According to the ICP-OES results in Table S1, the amount of Cu and Ga in the representative catalysts was similar to the designed ratio (11.2 wt% Cu and 6.6 wt% Ga in 10Cu5Ga/$CeO_2$; 10.2 wt% Cu and 5.5 wt% Ga in 10Cu5Ga/$CeO_2$-w).

As shown in Figure 2.3, the XRD patterns indicated that the Fluorite cubic $CeO_2$ ($F_{m-3m}$, JCPDS No. 34-0394) domains in all synthesized samples after $H_2$ reduction. Almost no shift of the main peak at 28.6$^o$, corresponding to (111) of $CeO_2$, was observed in pure $CeO_2$ and other catalysts, indicating that Cu and Ga were not doped into the lattice of cerium oxide. A small peak at 43.3$^o$ could be assigned to Cu (111). In addition, no peaks related to Ga species (Ga, $Ga_2O_3$ and $CuGa_2O_4$) were observed. Considering the amount of Cu (~10 wt.%) and Ga (~5 wt.%), this implied the high dispersion of both Cu and Ga species in all catalysts. $N_2$ adsorption−desorption isotherms and pore size distributions of 10Cu/$CeO_2$ and 10Cu5Ga/$CeO_2$ were investigated, as displayed in Figure 2.4 and Table 2.1. The introduction of Ga scarily changed the specific surface area and pore distribution of catalysts. HRTEM patterns showed the morphology of catalyst 10Cu5Ga/$CeO_2$, as shown in Figure 2.5a. Clear lattice fringes were measured to be 0.31 nm and 0.27 nm, which were attributed to the interplanar distance of the (111) and (200) plane of $CeO_2$.[26, 40] No lattice fringes attributed to Cu or $CuO_x$ nanoparticles were observed in the HRTEM images, mainly due to the similar contrasts of $CeO_2$ and Cu/$CuO_x$ and the expected ultrasmall size of Cu/$CuO_x$. No lattice fringes of Ga species were observed, either. The energy dispersive X-ray spectrometry (EDS) patterns in

Figure 2.5b and c showed that Cu and Ga existed and were well dispersed in the catalyst, suggesting the successful incorporation and uniform distribution of Cu and Ga species in the catalyst. Furthermore, the SEM pattern showed that catalysts remained part of the structure of MOF precursors after calcination treatment (Figure 2.6). This structure not only provided mesopore channels for accelerating the diffusion of reactants, but also increased the exposed catalytic sites to participate in the reaction, which could enhance catalytic activity.[31, 41]

**Table 2.1** Element composition and physical properties of samples

| Samples | $S_{BET}$ ($m^2/g$) | wt% of Cu | wt% of Ga | $D_{Cu}$ (%) [a] |
|---|---|---|---|---|
| 10Cu/$CeO_2$ | 55.0 | 9.8 | - | 49.2 |
| 10Cu5Ga/$CeO_2$ | 52.0 | 11.2 | 6.6 | 47.4 |
| 10Cu5Ga/$CeO_2$-w | 50.4 | 10.2 | 5.5 | 16.1 |

[a] calculated from oxygen chemisorption

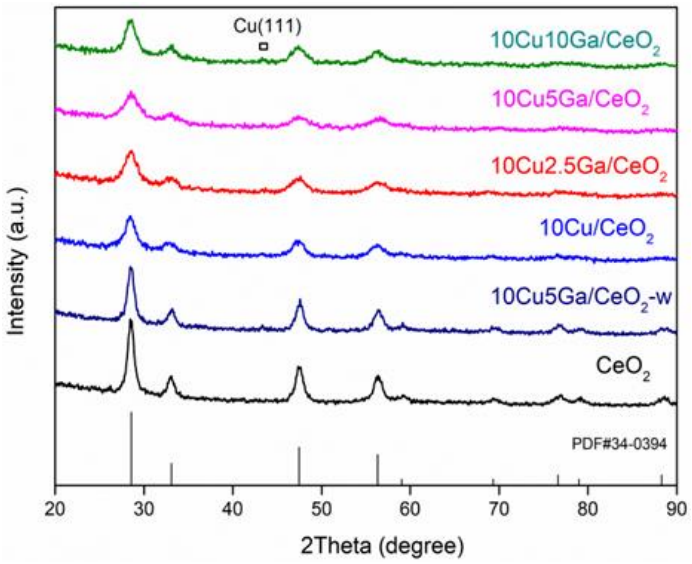


**Figure 2.3** XRD patterns of different ration of Cu/Ga on $CeO_2$ catalysts.

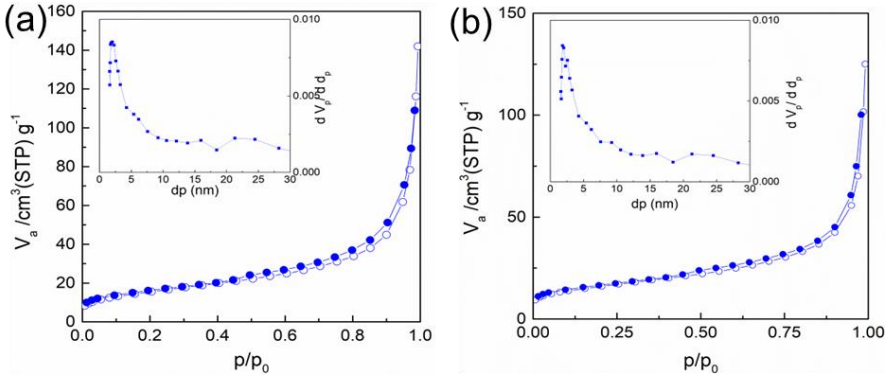


**Figure 2.4** Nitrogen adsorption−desorption isotherms and pore size distribution for (b) 10Cu/$CeO_2$ and (c) 10Cu5Ga/$CeO_2$.

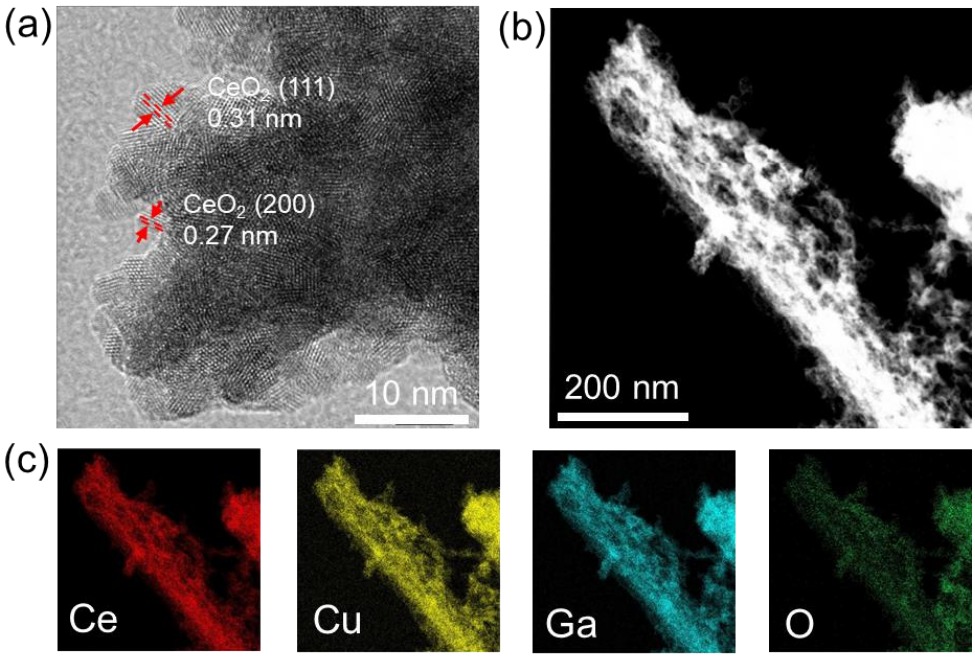


**Figure 2.5** Morphology of catalysts. (a) HRTEM image, (b and c) element mapping images of 10Cu5Ga/$CeO_2$.

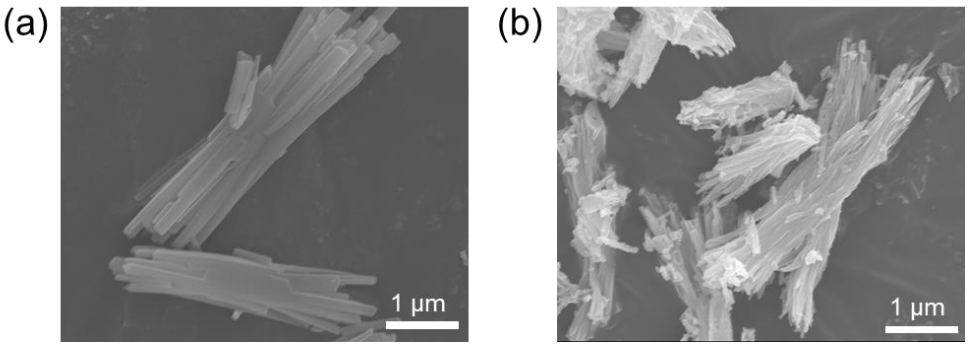

**Figure 2.6** SEM patterns of (a) 10Cu5Ga/Ce-MOF precusor and (b) 10Cu5Ga/$CeO_2$ derived from calcination of MOF precusor.

$H_2$-temperature-programmed reduction ($H_2$-TPR) experiment was conducted to study the behavior of catalysts under $H_2$ atmosphere (Figure 2.7a). In the profile of 10Cu/$CeO_2$, it displayed two distinct strong peaks centered at 132 and 162 °C, which were attributed to the two-step reduction of $Cu^{2+}$ to $Cu^{+}$ and subsequent $Cu^{+}$ to Cu respectively.[42] While in the pattern of 10Cu5Ga/$CeO_2$, three peaks centered at 145, 179 and 210 $^{o}$C were observed. The new peak at 210 $^{o}$C could be attributed to reduction of CuO strongly interacting with the support.[43] The shift of Cu reduction peaks to higher temperature suggested that the introduction of Ga enhanced the interaction between Cu and $CeO_2$ support (known as metal support interaction).[44] The results also implied that copper existed in the form of metallic Cu in the catalyst, in well agreement with ref. 26. In addition, the dispersion of Cu ($D_{Cu}$), defined as the ratio of Cu atoms exposed at the surface to total Cu atoms, was characterized by calculating the amount of $H_2$ consumed in the $H_2$-TPR analysis after low-temperature oxygen chemisorption, based on the previous reported method.[38] As shown in Table 2.1, the $D_{Cu}$ of MOF-derived 10Cu/$CeO_2$ and 10Cu5Ga/$CeO_2$ was quite similar, but was much higher than that of 10Cu5Ga/$CeO_2$-w by conventional wet impregnation method, indicating the high dispersion of Cu in the catalyst derived from in situ pyrolysis of MOF precursor, which could promote the catalytic activity. The optical properties of catalysts were analyzed by UV-vis DRS, as shown in Figure 2.7b. All catalysts containing Cu showed higher absorption in visible range, and the optical properties were not obviously changed by the incorporation of Ga. The enhanced absorption in the range of visible light was due to the metal-metal charge-transfer (MMCT) between Cu and $CeO_2$, confirming the presence of light-induced hot carriers.[32, 45] All catalysts showed excellent responses upon irradiation, and 10Cu/$CeO_2$ and 10Cu5Ga/$CeO_2$ generated higher photocurrent than pure $CeO_2$, indicating that photoinduced carriers could separate efficiently in Ga-Cu/$CeO_2$ catalysts.

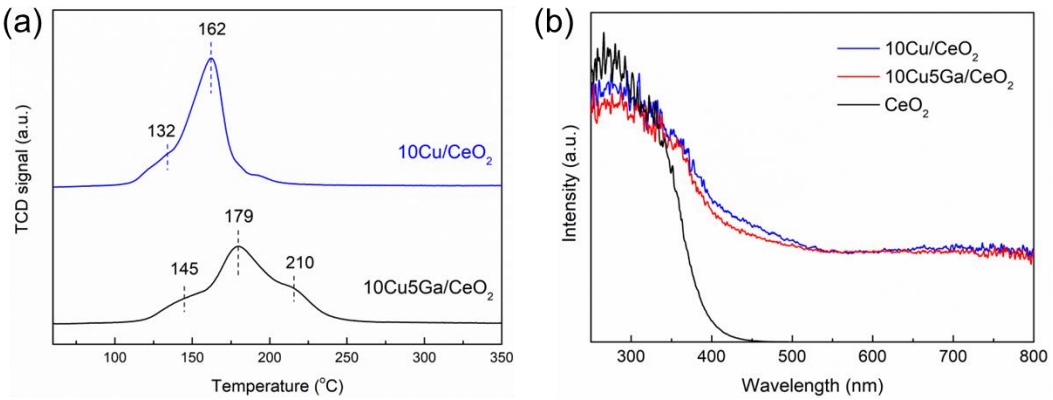


**Figure 2.7** (a) $H_2$-TPR patterns of $10Cu/CeO_2$ and $10Cu5Ga/CeO_2$, (b) UV-vis DRS spectra of pure $CeO_2$, $10Cu/CeO_2$ and $10Cu5Ga/CeO_2$.

The X-ray photoelectron spectroscopy (XPS) was employed to investigate the chemical state of elements in $10Cu/CeO_2$ and $10Cu5Ga/CeO_2$. As shown in Figure 2.8, two peaks centered at 932.2 eV and 934.1 eV were observed in the Cu 2p spectrum, which could be attributed to $Cu^0/Cu^+$ and $Cu^{2+}$ [25]. The Auger electron spectroscopy (AES) of Cu LMM in Figure 2.9 showed a peak at 569.8 eV, implying the presence of $Cu^+$ in catalysts.[10] The oxidation of metallic Cu could be ascribed to the exposing of catalysts to air before XPS experiment. As shown in Figure 2.10a, the Ga 3d pattern showed a peak at 19.8 eV, which was attributed to $Ga^{3+}$. In addition, the peak at 1117.0 eV in Ga $2p_{3/2}$ was ascribed to $Ga^{3+}$-O species (Figure 2.10b), suggesting that Ga species existed in the form of $Ga_2O_3$ in catalyst.[46] As shown in Figure 2.11, the spectra of Ce 3d were deconvoluted into several peaks, which could be attributed to $Ce^{4+}$ and $Ce^{3+}$. Through analyzing the valence of surface cerium, the amount of reduced cerium $Ce^{3+}$ of $10Cu/CeO_2$ is 10.4% calculated by $Ce^{3+}/ (Ce^{3+} + Ce^{4+})$. In contrast, much more surface Ce was reduced to $Ce^{3+}$ (16.8%) in $10Cu5Ga/CeO_2$[5, 27]. This implied that the introduction of Ga could modulate the electronic structure and enhance the reduction of $CeO_2$, therefore generating more oxygen vacancies on the surface and promoting the adsorption of $CO_2$. The difference of surface oxygen vacancies could be further confirmed by the XPS spectra of O 1s (Figure 2.8c and d). The four peaks centered at 529.3 eV, 530.5 eV, 531.5 eV and 532.5 eV could be assigned to the lattice oxygen ($O_L$), surface adsorption oxygen species at oxygen vacancy ($O_V$), surface hydroxyl

group (O-H) and the adsorbed $H_2O$ molecule ($H_2O$), respectively.[10] Obviously, 10Cu5Ga/$CeO_2$ possessed more surface oxygen vacancies than 10Cu/$CeO_2$, which was in agreement with the analysis of Ce 3d XPS spectra. To further verify the oxygen vacancies in catalysts, electron spin resonance (ESR) was conducted over 10Cu5Ga/$CeO_2$ (Figure 2.12), and the signals at $g_{\perp} = 2.035$ and $g_{\parallel} = 2.001$ were ascribed to oxygen vacancies of $CeO_2$.[47]

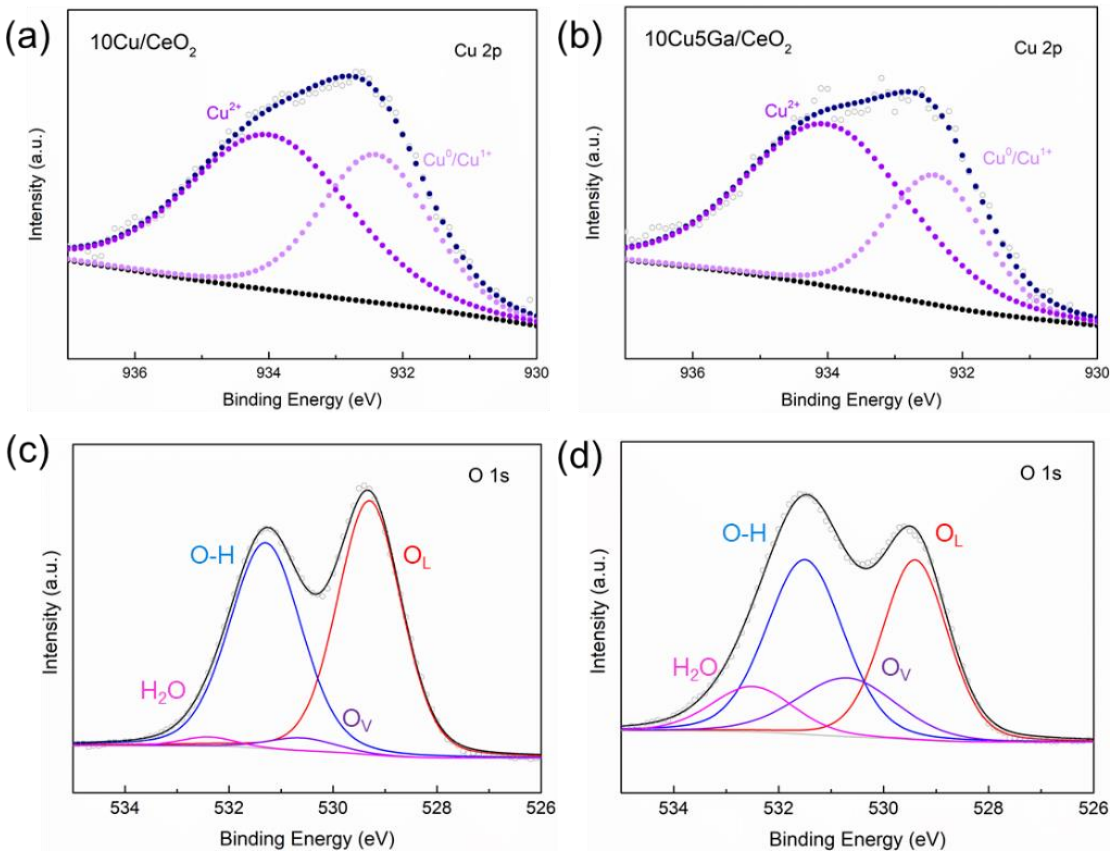


**Figure 2.8** XPS spectra of Cu 2p and O 1s for (a and c) 10Cu/$CeO_2$ and (b and d) 10Cu5Ga/$CeO_2$.

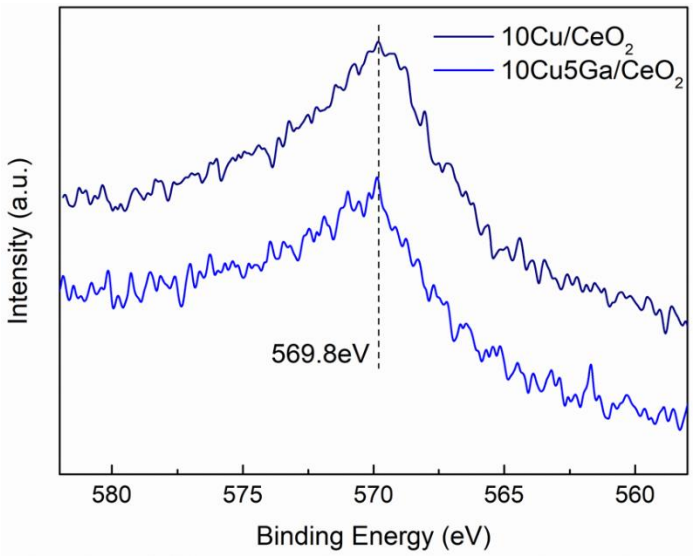


**Figure 2.9** Cu LMM Auger electron spectra of 10Cu/$CeO_2$ and 10Cu5Ga/$CeO_2$ catalysts.

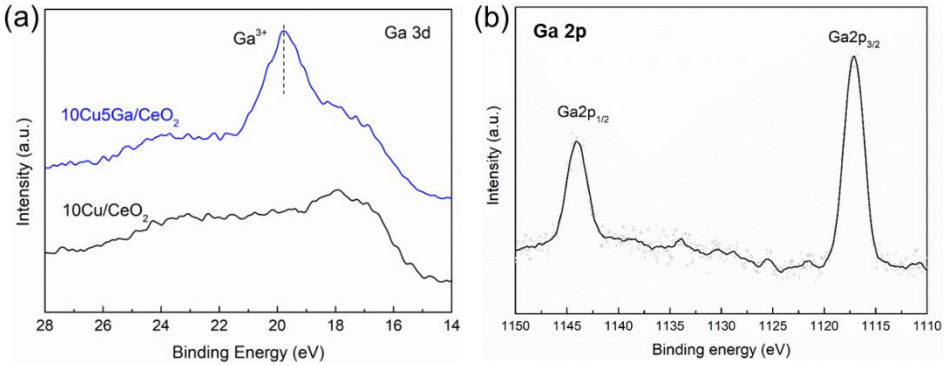


**Figure 2.10** XPS spectra of (a) Ga 3d and (b) Ga 2p for 10Cu5Ga/$CeO_2$.

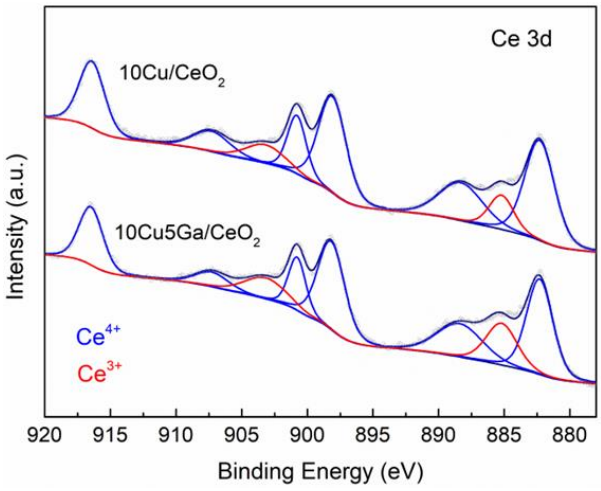


**Figure 2.11** XPS patterns Ce 3d of 10Cu/$CeO_2$ and10Cu5Ga/$CeO_2$ catalyst.

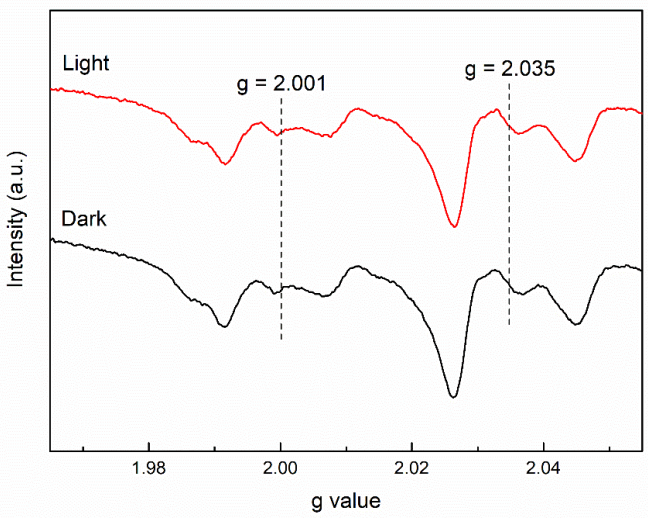


**Figure 2.12** ESR spectra of 10Cu5Ga/$CeO_2$ in dark and light at 120 K.

### 2.3.2 Solar-driven $CO_2$ reduction activity

I performed a sequence of photothermal RWGS tests over the synthesized catalysts. The 300 W Xenon lamp was used as the light source and the maximum light intensity was 1952 $mW \cdot cm^{-2}$, measured by the optical power meter. Upon irradiation, the temperature of catalysts rapidly increased to high temperature within 10 min and then maintained at the equilibrium temperature (Figure 2.13). The equilibrium temperature of catalysts increased linearly with the increase of illumination intensity, as depicted in Figure 2.14a. Catalysts loaded with Cu species showed a similar temperature, around 280 ℃ at the maximum intensity of light, while the temperatures of 5Ga/$CeO_2$ and pure $CeO_2$ could only reach 210 ℃ under the same condition, indicating that introduction of $Ga_2O_3$ has insignificant influence on the heating effect during reaction. CO was the main product in photothermal catalytic $CO_2$ reduction over all the catalysts with only a small portion of methanol (Figure 2.15). Figure 2.14b showed the CO production rates under different illumination intensity. 30.0 $mmol \cdot g^{-1} \cdot h^{-1}$ production of CO was obtained over 10Cu/$CeO_2$, under the maximum irradiation. With the introduction of Ga, all 10CuyGa/$CeO_2$ produced higher CO than 10Cu/$CeO_2$, indicating the dramatic enhancement of Ga species in catalytic activity. Typically, 10Cu5Ga/$CeO_2$ exhibited the highest production (111.2 $mmol \cdot g^{-1} \cdot h^{-1}$) at the maximum light input, which was superior to most reported Cu and other earth-abundant metals-based catalysts for

photothermal $CO_2$ reduction under similar reaction conditions (Table 1). In addition, 10Cu5Ga/$CeO_2$ exhibited much higher than the benchmark Cu/ZnO/$Al_2O_3$ catalyst (17.8 mmol·$g^{-1}$·$h^{-1}$ CO) in photothermal $CO_2$ reduction (Figure 2.16a). In contrast, almost no CO was produced on 5Ga/$CeO_2$ and pure $CeO_2$, implying that Cu species acted as the catalytic site in the process. Meanwhile, 10Cu5Ga/$CeO_2$-w produced only 24.8 mmol·$g^{-1}$·$h^{-1}$ of CO under the light irradiation of maximum intensity, much less than 10Cu5Ga/$CeO_2$ (Table 2.2). Excluding the influence of light absorption (Figure 2.16b), the high activity of 10Cu5Ga/$CeO_2$ prepared by in situ growth and pyrolysis of MOF precursors could be attributed to the high dispersion of Cu and the strong interaction between copper, gallium and cerium dioxide in MOF-derived 10Cu5Ga/$CeO_2$, as confirmed by the TPR results. The $^{13}CO_2$-isotopoe experiment showed that all the CO was produced from $CO_2$ (Figure 2.17). Figure 2.12c showed the solar energy conversion efficiency (η) of catalysts. The η of 10Cu5Ga/$CeO_2$ reached 0.83% under the irradiation intensity of 1952 mW·$cm^{-2}$. The stability test of 10Cu5Ga/$CeO_2$ was displayed in Figure 2.14d. The CO production remained ~70% of initial production after 7 h and then remained stable. The XRD pattern of used 10Cu5Ga/$CeO_2$ was almost the same as fresh sample (Figure 2.18), and the HRTEM images of used catalyst showed that the structure and morphology maintained unchanged after 10 h reaction (Figure 2.19), indicating a relatively good stability of catalyst.

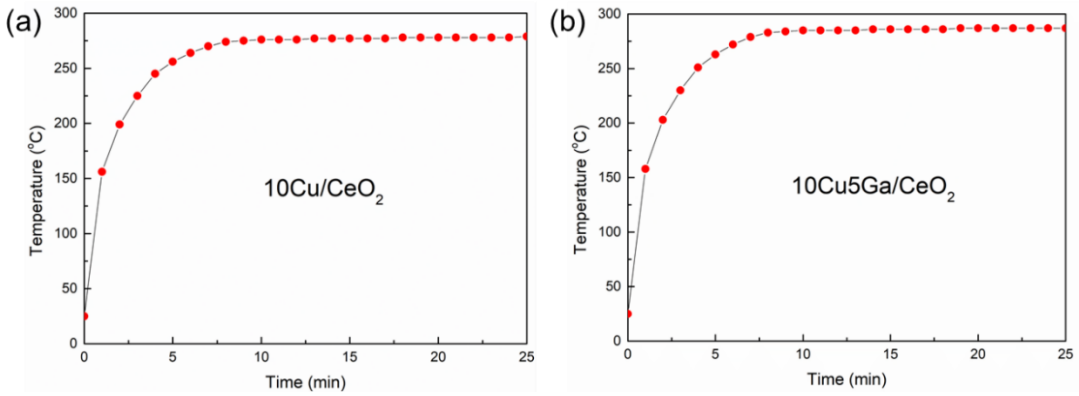


**Figure 2.13** Temporal temperature evolution over the catalysts under irradiation (1.95 W $cm^{-2}$)

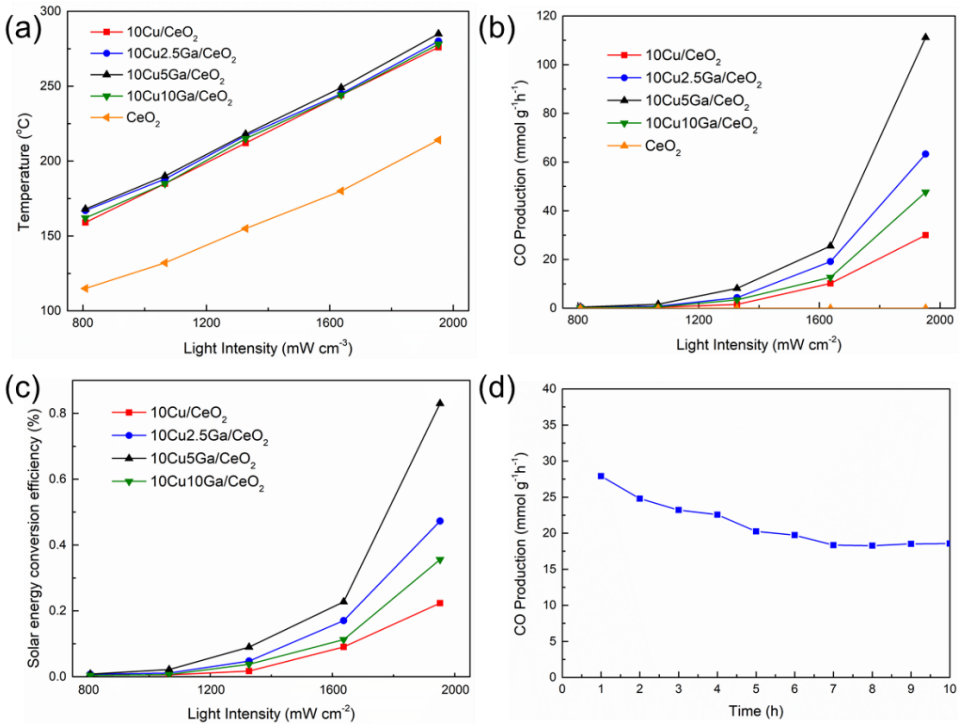


**Figure 2.14** Solar-driven $CO_2$ reduction. (a) Surface temperature of catalysts under different light intensity, (b) solar-driven CO production over CuGaCe catalysts, (c) solar energy conversion efficiency of CuGaCe catalysts, (d) durability test of 10Cu5Ga/$CeO_2$ under the irradiation of 1637 mW·$cm^{-2}$.

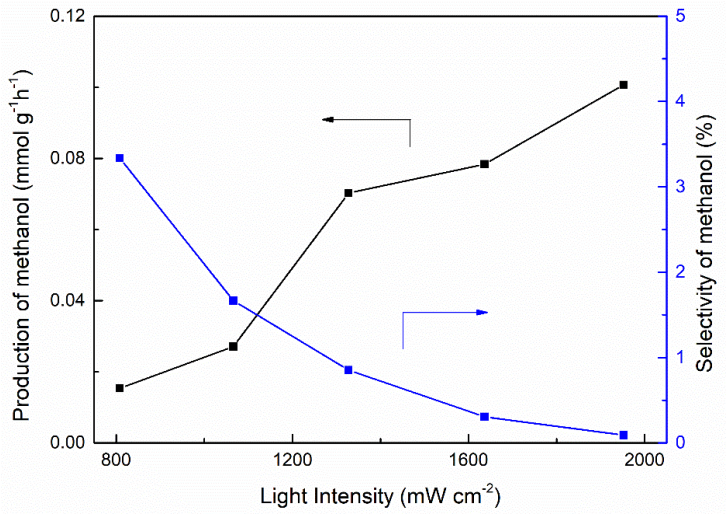


**Figure 2.15** Production and selectivity of methanol over 10Cu5Ga/$CeO_2$ under different light intensity.

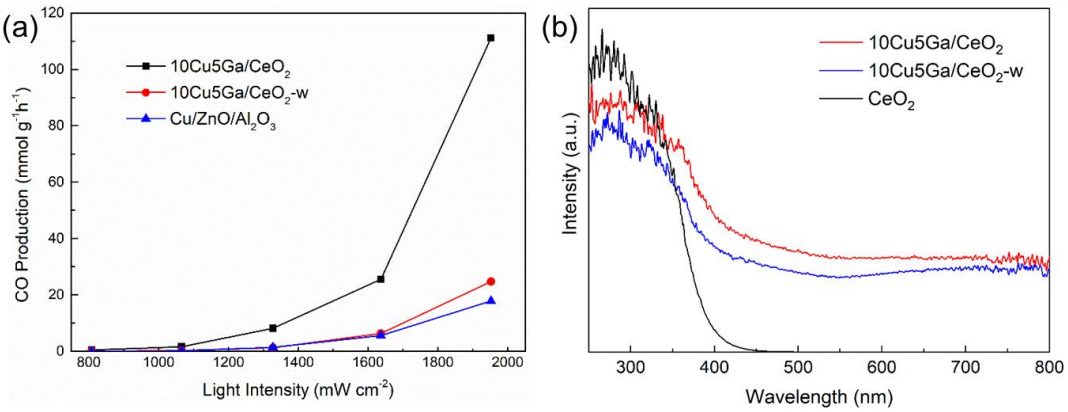


**Figure 2.16** (a) Solar-driven CO production over different catalysts under different intensity of light. (b) UV-Vis DRS for 10Cu5Ga/$CeO_2$ and 10Cu5Ga/$CeO_2$-w.

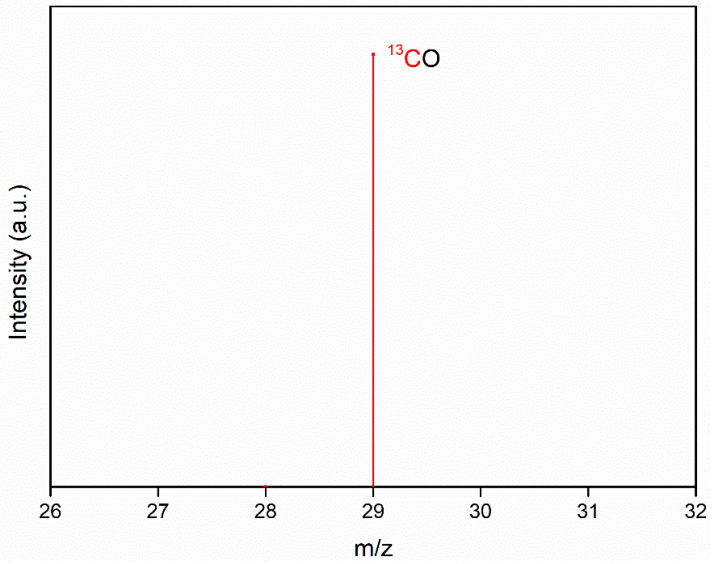


**Figure 2.17** GC-MS spectra of CO generated over 10Cu5Ga/$CeO_2$ with $^{13}CO_2$ + $H_2$.

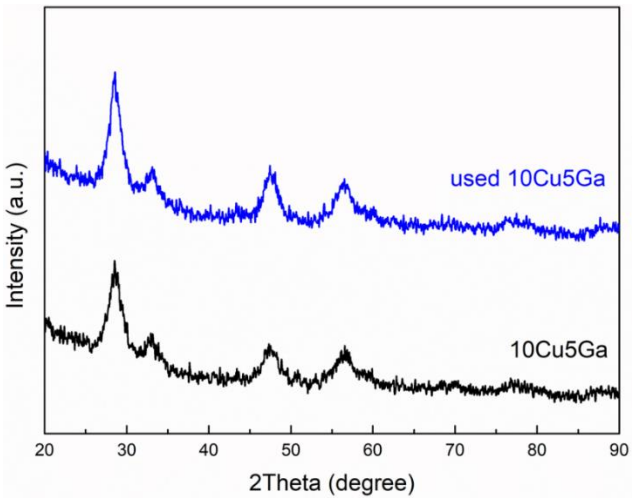


**Figure 2.18** XRD patterns of 10Cu5Ga/$CeO_2$ before and after durability test.

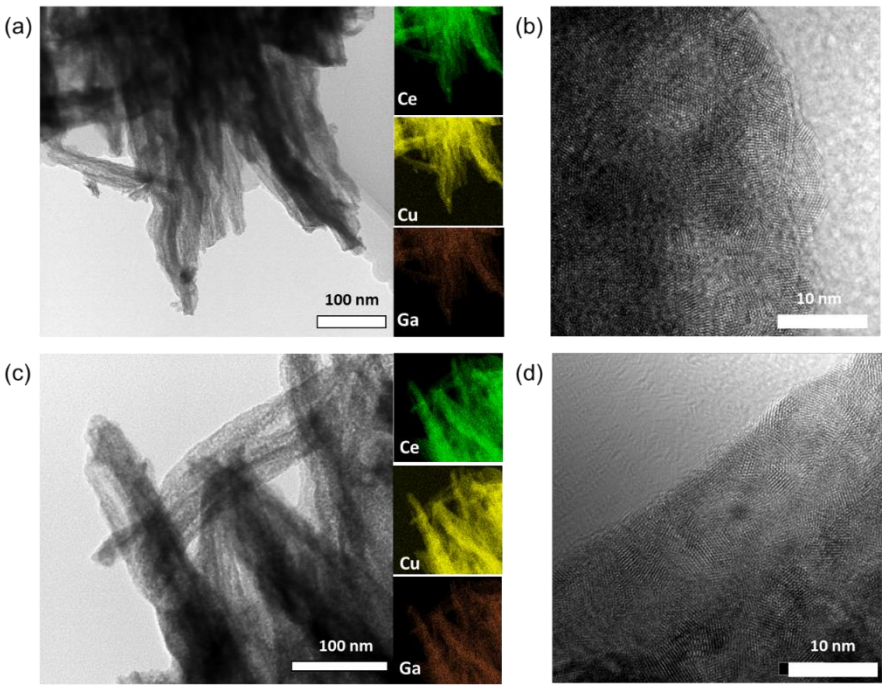


**Figure 2.19** HRTEM of (a & b) fresh and (c & d) used 10Cu5Ga/$CeO_2$ after 10 h reaction.

**Table 2.2** Comparison of CO production rates for some $CO_2$ hydrogenation catalysts

| Entry | Catalyst | Reactor | Gas composition | Catalytic condition | CO production rate | Ref. |
|---|---|---|---|---|---|---|
| 1 | 10Cu5Ga/$CeO_2$ | flow | $CO_2/H_2$ = 50/50<br>20 mL $min^{-1}$ | 300 W Xe lamp<br>(1.95 W $cm^{-2}$) | 111.2 mmol $g_{cat}^{-1}$ $h^{-1}$ | This work |
| 2 | 10Cu5Ga/$CeO_2$ | flow | $CO_2/H_2$ = 50/50<br>20 mL $min^{-1}$ | 300 W Xe lamp with concentrator (3.82 W $cm^{-2}$) | 337.2 mmol $g_{cat}^{-1}$ $h^{-1}$ | This work |
| 3 | 10Cu5Ga/$CeO_2$-w | flow | $CO_2/H_2$ = 50/50<br>20 mL $min^{-1}$ | 300 W Xe lamp<br>(1.95 W $cm^{-2}$) | 24.8 mmol $g_{cat}^{-1}$ $h^{-1}$ | This work |
| 4 | CF-$Cu_2O$ | flow | $CO_2/H_2$ = 83/17<br>43 mL $min^{-1}$ | Visible light, LED light,<br>5.0 W $cm^{-2}$, 4 bars | 139.6 mmol $g_{cat}^{-1}$ $h^{-1}$ | [10] |

| | | | | | | |
|---|---|---|---|---|---|---|
| 5 | $Cu_1Ca_9(PO_4)_6(OH)_2$ | flow | $CO_2/H_2$ = 50/50<br>2 mL $min^{-1}$ | 300 W Xe lamp<br>(2.0 W $cm^{-2}$), 300 °C | 0.84 mmol $g_{cat}^{-1}$ $h^{-1}$ | [23] |
| 6 | Al@$Cu_2O$ | flow | $CO_2/H_2$ = 50/50<br>10 mL $min^{-1}$ | supercontinuum fiber laser<br>(10 W $cm^{-2}$) | 2.03 mmol $g_{cat}^{-1}$ $h^{-1}$ | [48] |
| 7 | Cu/Pd/$H_yWO_{3-x}$ | flow | $CO_2/H_2$ = 50/50<br>4 mL $min^{-1}$ | 120 W Xe lamp,<br>2.0 W $cm^{-2}$, 250 °C | 1.18 mmol $g_{cat}^{-1}$ $h^{-1}$ | [49] |
| 8 | CuSiO/$CuO_x$ | flow | $CO_2/H_2/Ar$ = 24/72/4<br>20 mL $min^{-1}$ | 500 °C | 40.4 mmol $g_{cat}^{-1}$ $h^{-1}$ | [50] |
| 9 | $Fe_3O_4$ | batch | $CO_2/H_2/Ar$ =<br>15/60/25 | 300 W Xe lamp,<br>5.2 W $cm^{-2}$, 1.8 bars | 18.3 mmol $g_{cat}^{-1}$ $h^{-1}$ | [51] |
| 10 | $Ni_{12}P_5/SiO_2$ | flow | $CO_2/H_2$ = 5/1<br>3 mL $min^{-1}$ | 0.8 W $cm^{-2}$,<br>290 °C | 13.5 mmol $g_{cat}^{-1}$ $h^{-1}$ | [52] |
| 11 | $In_2O_{3-x}(OH)_y$ /SiNW | batch | $CO_2/H_2$ = 50/50 | 300 W Xe lamp,<br>2.0 W $cm^{-2}$, 150 °C | 0.022 mmol $g_{cat}^{-1}$ $h^{-1}$ | [53] |
| 12 | $In_2O_{3-x}$ nanosheet | batch | $CO_2/H_2$ = 50/50 | 300 W Xe lamp,<br>2.16 W $cm^{-2}$ | 103.2 mmol $g_{cat}^{-1}$ $h^{-1}$ | [54] |

### 2.3.3 Photothermocatalytic mechanism of $CO_2$ reduction

Generally, full-spectrum irradiation can provide enough thermal energy to elevate the surface temperature of catalysts, triggering catalytic reactions. In this chapter, all catalysts containing copper showed similar temperature (270 – 285 °C) under the same irradiation, while the activity for CO production ranged from 24.8 to 111.2 $mmol \cdot g^{-1} \cdot h^{-1}$, displaying totally different performance. Therefore, the mechanism of Ga-promotion and light enhancement needs to be investigated.

To this end, photo-assisted thermal $CO_2$ reduction reaction was performed on the home-made stainless-steel reactor, in which the temperatures of catalysts could be well controlled by external heating and thermocouple. An HA30 filter was utilized to exclude the influence of photothermal effect caused by IR light. CO production over both $10Cu/CeO_2$ and $10Cu5Ga/CeO_2$ under dark and light conditions were shown in Figure 2.20. In the dark condition, the activity of $10Cu5Ga/CeO_2$ was increased from 2.2 $mmol \cdot g^{-1} \cdot h^{-1}$ to 36.0 $mmol \cdot g^{-1} \cdot h^{-1}$ as the temperature increased from 240 $^oC$ to 320 $^oC$, which was higher than that of $10Cu/CeO_2$ under the same condition. After the introduction of light, the CO production was further enhanced. At 240 $^oC$, CO yield over $10Cu5Ga/CeO_2$ was increased to 6.1 $mmol \cdot g^{-1} \cdot h^{-1}$ under UV-visible light, which was 2.8 times higher than the production under dark. When the reaction temperature was increased to 320 $^oC$, the CO production under light reached 54.8 $mmol \cdot g^{-1} \cdot h^{-1}$, still higher than the yield in dark. These results indicated the obvious enhancement of UV-visible light irradiation on the activity via light-induced hot carriers.

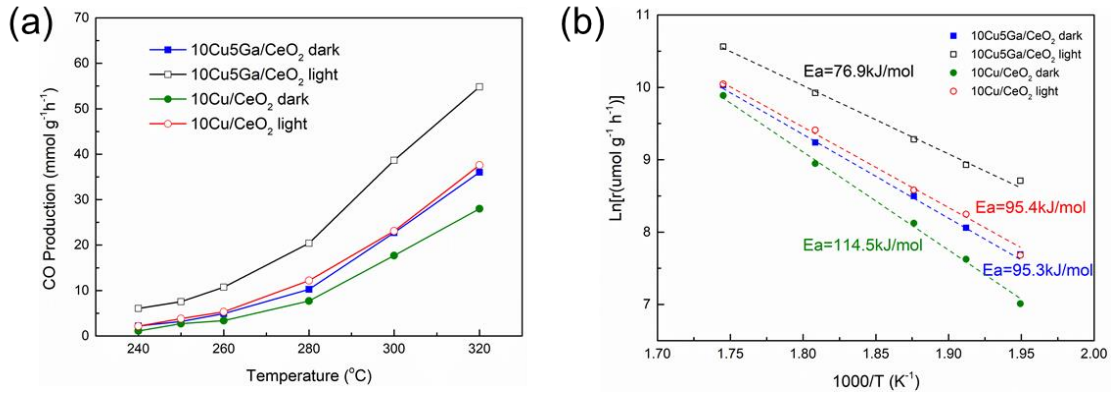


**Figure 2.20** Photo-assisted thermal $CO_2$ reduction. (a) CO production over $10Cu/CeO_2$ and $10Cu5Ga/CeO_2$ catalysts as a function of temperature under thermal heating condition (dark) and photo-assisted thermal heating condition (light), (b) corresponding Arrhenius plots for CO yield under dark and light conditions.

The reaction mechanism of the RWGS reaction under dark and light were investigated in the temperature range from 240 $^oC$ to 300 $^oC$. The apparent activation energy ($E_a$) was calculated to elucidate the reaction kinetics according to the Arrhenius equation ($\ln r = -E_a/RT + \ln A$). As shown in Figure 2.20b, the apparent activation

energy for 10Cu/$CeO_2$ in dark was 114.5 kJ·$mol^{-1}$, and was reduced to 95.4 kJ·$mol^{-1}$ with the introduction of light. This indicated that light could promote the activation of reactants, thus enhance the production. In addition, the gallium species in 10Cu5Ga/$CeO_2$ further reduced the apparent activation energy to 95.3 kJ·$mol^{-1}$ and 76.9 kJ·$mol^{-1}$ in dark and light respectively, demonstrating the Ga species could significantly promote the reaction activity.

In situ DRIFTS was utilized to investigate the possible reaction route for solar-driven RWGS reaction and the spectra were shown in Figure 2.21. After the introduction of reaction gas ($CO_2$ and $H_2$) over the reduced 10Cu/$CeO_2$ (Figure 2.21a) and 10Cu5Ga/$CeO_2$ (Figure 2.21b) at room temperature, a broad absorption band appeared between 800 to 1700 $cm^{-1}$, corresponding to surface carbonate or formate species.[55-57] As the temperature increased from 25 to 300 °C, several absorption peaks increased in the range of 2200 to 2100 $cm^{-1}$ and 3000 to 2800 $cm^{-1}$, corresponding to carbonyl species and the C-H vibration of formate species, respectively.[26, 27, 58] The detailed assignment of the IR absorption peaks was listed in Table 2.3. With the elevation of temperature, both 10Cu/$CeO_2$ and 10Cu5Ga/$CeO_2$ showed gradually increased absorption of $CO_2$ to form various carbonate species, while 10Cu5Ga/$CeO_2$ exhibited higher surface concentration of carbonate species than 10Cu/$CeO_2$, indicating that Ga species promoted the adsorption of $CO_2$, which was due to the increased surface oxygen vacancies in 10Cu5Ga/$CeO_2$ according to the XPS results. For 10Cu/$CeO_2$, the surface formate species were formed at the temperature of 200 °C as the observation of C-H stretch vibration peaks at 2945 and 2846 $cm^{-1}$, which could be assigned to bidentate formate.[27] Meanwhile, a peak at around 2110 $cm^{-1}$ appeared, corresponding to the formation of CO adsorbed on the catalyst surface.[59] The same absorption peaks of bidentate formate were observed over 10Cu5Ga/$CeO_2$ at a much lower temperature, 150 °C. The peaks at 2846 $cm^{-1}$, 1571 $cm^{-1}$ and 1370 $cm^{-1}$ increased with the temperature elevated to 250 °C and then became weaker at 300 °C. This phenomenon illustrated that bidentate formate species were active surface intermediates, and $Ga_2O_3$

enhanced the activity through promoting the formation of surface formate from adsorbed carbonates, possibly via assisting H spillover process.[34]

**Table 2.3** Assignment of absorbance peaks of in situ DRIFTS spectra[26, 27, 56-60]

| Group | Species assignment | Frequencies ($cm^{-1}$) |
|---|---|---|
| Carbonate | bidentate carbonate | 1592, 1287, 848 |
| | polydentate carbonate | 1474, 1353, 1074, 848 |
| Carbonyl | M-CO | ~2110 |
| Formate | bidentate formate | 2945, 2846, 1571, 1370 |

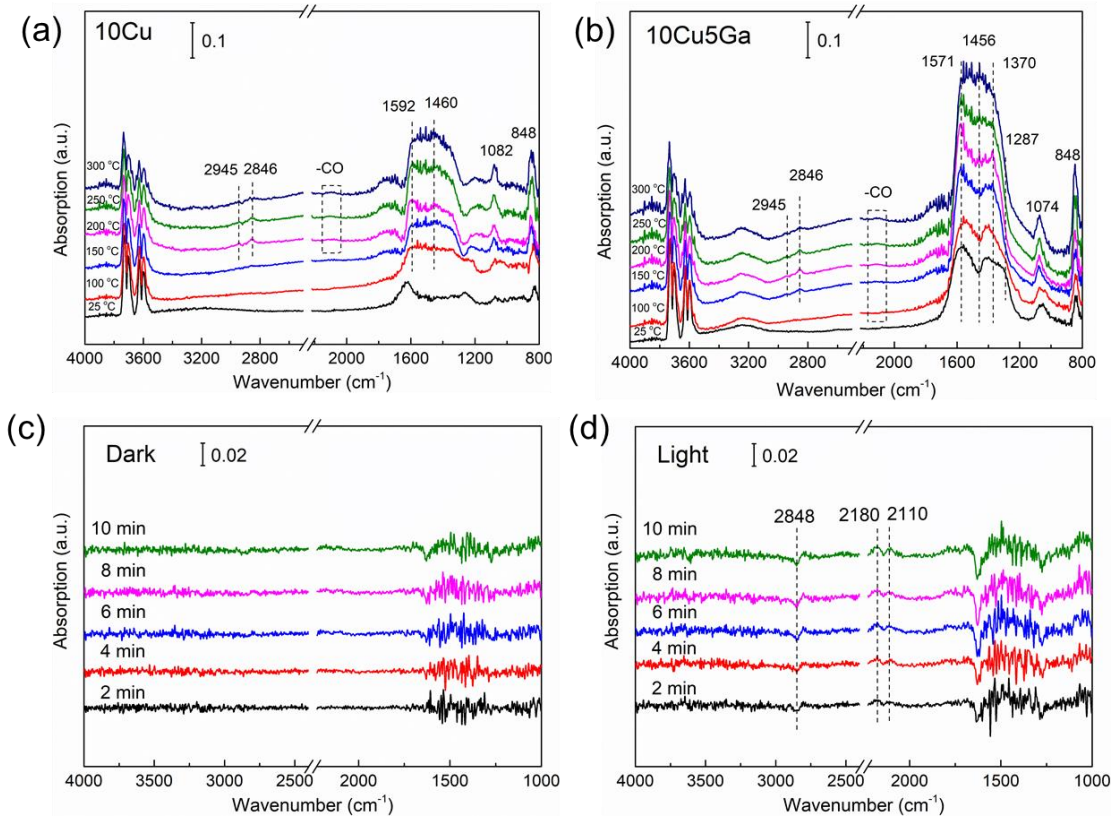


**Figure 2.21** In situ DRIFTS spectra collected over (a) 10Cu/$CeO_2$ and (b) 10Cu5Ga/$CeO_2$ catalysts during photo-assisted RWGS reaction under different temperature, in situ DRIFTS spectra over 10Cu5Ga/$CeO_2$ catalyst under (c) dark and (d) light at 250 °C for different time.

In order to study the influence of irradiation on the reaction pathway, another in situ DRIFTS test was conducted on 10Cu5Ga/$CeO_2$ with/without light irradiation and the obtained spectra were shown in Figure 2.19c and d. Accordingly, the peak at 2845 $cm^{-1}$ was attributed to bidentate formate while the two peaks centered at 2180 and 2110 $cm^{-1}$ could be ascribed to CO in the gas. Compared with the spectrum in dark, the peak related to formate decreased after the introduction of light while the intensity of CO adsorption increased. This further confirmed that CO was produced via the decomposition of formate intermediates and light irradiation promoted this reaction step via light-induced hot carriers.[59]

Based on the above discussion and previous literature[26, 27, 55], I propose a brief reaction mechanism of photothermal RWGS over CuGa/$CeO_2$ catalysts. As shown in Figure 2.22, under light irradiation, photothermal heating can trigger $CO_2$ reduction with $H_2$ by elevating the surface temperature of catalysts. $CO_2$ is easily adsorbed on oxygen vacancy sites formed on the surface of $CeO_2$ in the form of carbonates ($CO_3^{2-}$). The introduction of $Ga_2O_3$ could modulate the electronic structure of $CeO_2$ and promote the formation of oxygen vacancies to further facilitate the $CO_2$ adsorption. The adsorbed H species produced from $H_2$ dissociation on the surface of Cu nanoparticles then spill over to react with $CO_3^{2-}$ to form bidentate formates ($HCOO^-$), which eventually decompose to CO. The presence of $Ga_2O_3$ could enhance the interaction between Cu and $CeO_2$ support, possibly assisting H spillover to promote the formation of intermediate formate at the interface of Cu and $CeO_{2-x}$. More importantly, the light-excited hot carriers not only have the potential of promoting $H_2$ dissociation to H species but also accelerate the decomposition of formates into adsorbed CO and $H_2O$, thereby resulting in the lower activation energy compared with pure thermocatalytic reaction.

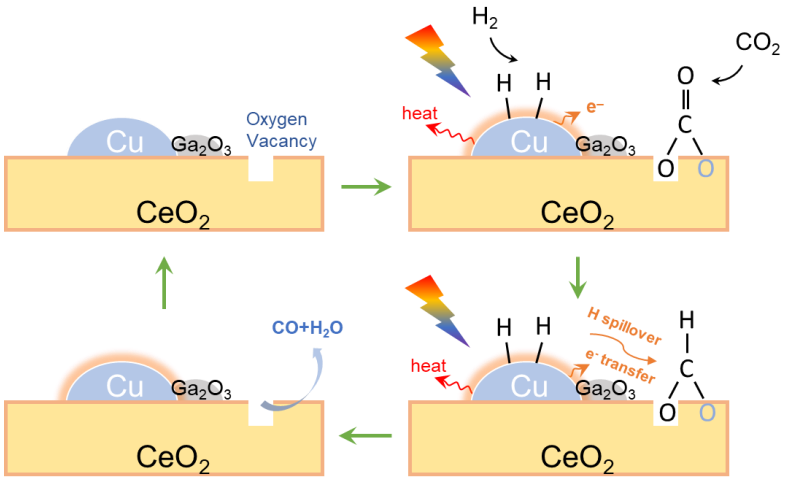


**Figure 2.22** Proposed reaction mechanism for photothermal RWGS over CuGa/$CeO_2$.

## 2.4 Conclusion

In conclusion, this chapter reports a MOF-assisted synthesis method to prepare well dispersed Ga- Cu/$CeO_2$ as a highly active catalyst for solar-driven RWGS reaction. The introduction of gallium dramatically increases the reaction activity, and 10Cu5Ga/$CeO_2$ shows the best performance with the CO yield rate of 111.2 mmol·$g^{-1}$·$h^{-1}$ under 1952 mW·$cm^{-2}$ irradiation and the solar energy conversion efficiency reaches 0.83%. Mechanism study demonstrates that the synergy of solar heating and light promotion reduce the apparent activation energy and contribute to the dramatically increased CO production. The introduction of Ga promotes the generation of oxygen vacancies on $CeO_2$ surface and increases the interaction between Cu and $CeO_2$, thus enhances $CO_2$ adsorption on catalyst surface and bidentate formate intermediates formation. The irradiation could facilitate the decomposition of formate species into carbonyl and finally into CO as product. Therefore, this study demonstrates a promising application for $CO_2$ reduction and renewable solar energy conversion.

## References

[1] E.C. Ra, K.Y. Kim, E.H. Kim, H. Lee, K. An, J.S. Lee, Recycling Carbon Dioxide through Catalytic Hydrogenation: Recent Key Developments and Perspectives, ACS Catalysis, 10 (2020) 11318-11345.

[2] X. Jiang, X. Nie, X. Guo, C. Song, J.G. Chen, Recent Advances in Carbon Dioxide Hydrogenation to Methanol via Heterogeneous Catalysis, Chem. Rev., 120 (2020) 7984-8034.

[3] A. Chatterjee, M.M. Gierach, A.J. Sutton, R.A. Feely, D. Crisp, A. Eldering, M.R. Gunson, C.W. O'Dell, B.B. Stephens, D.S. Schimel, Influence of El Niño on atmospheric $CO_2$ over the tropical Pacific Ocean: Findings from NASA's OCO-2 mission, Science, 358 (2017) eaam5776.

[4] J.W. Ager, A.A. Lapkin, Chemical storage of renewable energy, Science, 360 (2018) 707.

[5] K. Chang, H. Zhang, M.-j. Cheng, Q. Lu, Application of Ceria in $CO_2$ Conversion Catalysis, ACS Catalysis, 10 (2019) 613-631.

[6] T. Kong, Y. Jiang, Y. Xiong, Photocatalytic $CO_2$ conversion: What can we learn from conventional $CO_x$ hydrogenation?, Chem. Soc. Rev., 49 (2020) 6579-6591.

[7] X. Meng, L. Liu, S. Ouyang, H. Xu, D. Wang, N. Zhao, J. Ye, Nanometals for Solar-to-Chemical Energy Conversion: From Semiconductor-Based Photocatalysis to Plasmon-Mediated Photocatalysis and Photo-Thermocatalysis, Adv. Mater., 28 (2016) 6781-6803.

[8] J. Jia, H. Wang, Z. Lu, P.G. O'Brien, M. Ghoussoub, P. Duchesne, Z. Zheng, P. Li, Q. Qiao, L. Wang, A. Gu, A.A. Jelle, Y. Dong, Q. Wang, K.K. Ghuman, T. Wood, C. Qian, Y. Shao, C. Qiu, M. Ye, Y. Zhu, Z.H. Lu, P. Zhang, A.S. Helmy, C.V. Singh, N.P. Kherani, D.D. Perovic, G.A. Ozin, Photothermal Catalyst Engineering: Hydrogenation of Gaseous $CO_2$ with High Activity and Tailored Selectivity, Adv Sci (Weinh), 4 (2017) 1700252.

[9] R.P. Ye, J. Ding, W. Gong, M.D. Argyle, Q. Zhong, Y. Wang, C.K. Russell, Z. Xu, A.G. Russell, Q. Li, M. Fan, Y.G. Yao, $CO_2$ hydrogenation to high-value products via heterogeneous catalysis, Nat Commun, 10 (2019) 5698.

[10] L. Wan, Q. Zhou, X. Wang, T.E. Wood, L. Wang, P.N. Duchesne, J. Guo, X. Yan, M. Xia, Y.F. Li, A.A. Jelle, U. Ulmer, J. Jia, T. Li, W. Sun, G.A. Ozin, $Cu_2O$ nanocubes with mixed oxidation-state facets for (photo)catalytic hydrogenation of carbon dioxide, Nature Catalysis, 2 (2019) 889-898.

[11] N. Podrojková, V. Sans, A. Oriňak, R. Oriňaková, Recent Developments in the Modelling of Heterogeneous Catalysts for $CO_2$ Conversion to Chemicals, ChemCatChem, 12 (2020) 1802-1825.

[12] M. Ghoussoub, M. Xia, P.N. Duchesne, D. Segal, G. Ozin, Principles of photothermal gas-phase heterogeneous $CO_2$ catalysis, Energy & Environmental Science, 12 (2019) 1122-1142.

[13] C. Xu, J. Hong, P. Sui, M. Zhu, Y. Zhang, J.-L. Luo, Standalone Solar Carbon-Based Fuel Production Based on Semiconductors, Cell Reports Physical Science, 1 (2020) 100101.

[14] H. Song, X. Meng, T.D. Dao, W. Zhou, H. Liu, L. Shi, H. Zhang, T. Nagao, T. Kako, J. Ye, Light-Enhanced Carbon Dioxide Activation and Conversion by Effective Plasmonic Coupling Effect of Pt and Au Nanoparticles, ACS Appl Mater Interfaces, 10 (2018) 408-416.

[15] K.M. Choi, D. Kim, B. Rungtaweevoranit, C.A. Trickett, J.T. Barmanbek, A.S. Alshammari, P. Yang, O.M. Yaghi, Plasmon-Enhanced Photocatalytic $CO_2$ Conversion within Metal-Organic Frameworks under Visible Light, J. Am. Chem. Soc., 139 (2017) 356-362.

[16] S. Luo, H. Song, D. Philo, M. Oshikiri, T. Kako, J. Ye, Solar-driven production of hydrogen and acetaldehyde from ethanol on Ni-Cu bimetallic catalysts with solar-to-fuels conversion efficiency up to 3.8 %, Applied Catalysis B: Environmental, 272 (2020) 118965.

[17] H. Yang, Z.H. Wang, Y.Y. Zheng, L.Q. He, C. Zhan, X. Lu, Z.Q. Tian, P.P. Fang, Y. Tong, Tunable Wavelength Enhanced Photoelectrochemical Cells from Surface Plasmon Resonance, J. Am. Chem. Soc., 138 (2016) 16204-16207.

[18] J. Li, X. Yang, C. Ma, Y. Lei, Z. Cheng, Z. Rui, Selectively recombining the photoinduced charges in bandgap-broken $Ag_3PO_4/GdCrO_3$ with a plasmonic Ag bridge for efficient photothermocatalytic VOCs degradation and $CO_2$ reduction, Applied Catalysis B: Environmental, 291 (2021) 120053.

[19] D. Mateo, J.L. Cerrillo, S. Durini, J. Gascon, Fundamentals and applications of photo-thermal catalysis, Chem. Soc. Rev., 50 (2021) 2173-2210.

[20] J. Kong, C. Jiang, Z. Rui, S. Liu, F. Xian, W. Ji, H. Ji, Photothermocatalytic synergistic oxidation: An effective way to overcome the negative water effect on supported noble metal catalysts for VOCs oxidation, Chem. Eng. J., 397 (2020) 125485.

[21] L. Kang, X.Y. Liu, A. Wang, L. Li, Y. Ren, X. Li, X. Pan, Y. Li, X. Zong, H. Liu, A.I. Frenkel, T. Zhang, Photo-thermo Catalytic Oxidation over a $TiO_2$-$WO_3$ Supported Platinum Catalyst, Angew. Chem. Int. Ed. Engl., 59 (2020) 12909-12916.

[22] D. Vovchok, C. Zhang, S. Hwang, L. Jiao, F. Zhang, Z. Liu, S.D. Senanayake, J.A. Rodriguez, Deciphering Dynamic Structural and Mechanistic Complexity in $Cu/CeO_2$/ZSM-5 Catalysts for the Reverse Water-Gas Shift Reaction, ACS Catalysis, 10 (2020) 10216-10228.

[23] J. Guo, P.N. Duchesne, L. Wang, R. Song, M. Xia, U. Ulmer, W. Sun, Y. Dong, J.Y.Y. Loh, N.P. Kherani, J. Du, B. Zhu, W. Huang, S. Zhang, G.A. Ozin, High-Performance, Scalable, and Low-Cost Copper Hydroxyapatite for Photothermal $CO_2$ Reduction, ACS Catalysis, 10 (2020) 13668-13681.

[24] S. Choi, B.I. Sang, J. Hong, K.J. Yoon, J.W. Son, J.H. Lee, B.K. Kim, H. Kim, Catalytic behavior of metal catalysts in high-temperature RWGS reaction: In-situ FT-IR experiments and first-principles calculations, Sci Rep, 7 (2017) 41207.

[25] M. Zhu, P. Tian, M.E. Ford, J. Chen, J. Xu, Y.-F. Han, I.E. Wachs, Nature of Reactive Oxygen Intermediates on Copper-Promoted Iron–Chromium Oxide Catalysts during $CO_2$ Activation, ACS Catalysis, 10 (2020) 7857-7863.

[26] S.-C. Yang, S.H. Pang, T.P. Sulmonetti, W.-N. Su, J.-F. Lee, B.-J. Hwang, C.W. Jones, Synergy between Ceria Oxygen Vacancies and Cu Nanoparticles Facilitates the Catalytic Conversion of $CO_2$ to CO under Mild Conditions, ACS Catalysis, 8 (2018) 12056-12066.

[27] L. Lin, S. Yao, Z. Liu, F. Zhang, N. Li, D. Vovchok, A. Martínez-Arias, R. Castañeda, J. Lin, S.D. Senanayake, D. Su, D. Ma, J.A. Rodriguez, In Situ Characterization of $Cu/CeO_2$ Nanocatalysts for $CO_2$ Hydrogenation: Morphological Effects of Nanostructured Ceria on the Catalytic Activity, The Journal of Physical Chemistry C, 122 (2018) 12934-12943.

[28] B. An, J. Zhang, K. Cheng, P. Ji, C. Wang, W. Lin, Confinement of Ultrasmall Cu/ZnOx Nanoparticles in Metal-Organic Frameworks for Selective Methanol Synthesis from Catalytic Hydrogenation of $CO_2$, J. Am. Chem. Soc., 139 (2017) 3834-3840.

[29] G. Wang, C.T. He, R. Huang, J. Mao, D. Wang, Y. Li, Photoinduction of Cu Single Atoms Decorated on UiO-66-$NH_2$ for Enhanced Photocatalytic Reduction of $CO_2$ to Liquid Fuels, J. Am. Chem. Soc., 142 (2020) 19339-19345.

[30] W.-G. Cui, G.-Y. Zhang, T.-L. Hu, X.-H. Bu, Metal-organic framework-based heterogeneous catalysts for the conversion of C1 chemistry: CO, $CO_2$ and $CH_4$, Coord. Chem. Rev., 387 (2019) 79-120.

[31] X. Chen, Q. Li, M. Zhang, J. Li, S. Cai, J. Chen, H. Jia, MOF-Templated Preparation of Highly Dispersed $Co/Al_2O_3$ Composite as the Photothermal Catalyst with High Solar-to-Fuel Efficiency for $CO_2$ Methanation, ACS Appl Mater Interfaces, 12 (2020) 39304-39317.

[32] F. Wang, J. Tian, M. Li, W. Li, L. Chen, X. Liu, J. Li, A. Muhetaer, Q. Li, Y. Wang, L. Gu, D. Ma, D. Xu, A Photoactivated Cu-$CeO_2$ Catalyst with Cu-[O]-Ce Active Species Designed through MOF Crystal Engineering, Angew. Chem. Int. Ed. Engl., 59 (2020) 8203-8209.

[33] T. Montini, M. Melchionna, M. Monai, P. Fornasiero, Fundamentals and Catalytic Applications of $CeO_2$-Based Materials, Chem. Rev., 116 (2016) 5987-6041.

[34] J.C. Medina, M. Figueroa, R. Manrique, J. Rodríguez Pereira, P.D. Srinivasan, J.J. Bravo-Suárez, V.G. Baldovino Medrano, R. Jiménez, A. Karelovic, Catalytic consequences of Ga promotion on Cu for $CO_2$ hydrogenation to methanol, Catalysis Science & Technology, 7 (2017) 3375-3387.

[35] H. Ham, S.W. Baek, C.-H. Shin, J.W. Bae, Roles of Structural Promoters for Direct $CO_2$ Hydrogenation to Dimethyl Ether over Ordered Mesoporous Bifunctional Cu/M–$Al_2O_3$ (M = Ga or Zn), ACS Catalysis, 9 (2018) 679-690.

[36] M.M.J. Li, C. Chen, T. Ayvalı, H. Suo, J. Zheng, I.F. Teixeira, L. Ye, H. Zou, D. O'Hare, S.C.E. Tsang, $CO_2$ Hydrogenation to Methanol over Catalysts Derived from Single Cationic Layer CuZnGa LDH Precursors, ACS Catalysis, 8 (2018) 4390-4401.

[37] J. Wang, G. Li, Z. Li, C. Tang, Z. Feng, H. An, H. Liu, T. Liu, C. Li, A highly selective and stable ZnO-$ZrO_2$ solid solution catalyst for $CO_2$ hydrogenation to methanol, Science Advances, 3 (2017) e1701290.

[38] N. Pernicone, T. Fantinel, C. Baldan, P. Riello, F. Pinna, On the measurement of copper surface area by oxygen chemisorption, Applied Catalysis A: General, 240 (2003) 199-206.

[39] L. Zhou, D.F. Swearer, C. Zhang, H. Robatjazi, H. Zhao, L. Henderson, L. Dong, P. Christopher, E.A. Carter, P. Nordlander, N.J. Halas, Quantifying hot carrier and thermal contributions in plasmonic photocatalysis, Science, 362 (2018) 69.

[40] H. Li, Y. Cui, Q. Liu, W.-L. Dai, Insight into the Synergism between Copper Species and Surface Defects Influenced by Copper Content over Copper/Ceria Catalysts for the Hydrogenation of Carbonate, ChemCatChem, 10 (2018) 619-624.

[41] S. Mehla, A.E. Kandjani, R. Babarao, A.F. Lee, S. Periasamy, K. Wilson, S. Ramakrishna, S.K. Bhargava, Porous crystalline frameworks for thermocatalytic $CO_2$ reduction: an emerging paradigm, Energy & Environmental Science, 14 (2021) 320-352.

[42] P. Zimmer, A. Tschöpe, R. Birringer, Temperature-Programmed Reaction Spectroscopy of Ceria- and Cu/Ceria-Supported Oxide Catalyst, J. Catal., 205 (2002) 339-345.

[43] C. Li, Y. Yang, W. Ren, J. Wang, T. Zhu, W. Xu, Effect of Ce Doping on Catalytic Performance of $Cu/TiO_2$ for CO Oxidation, Catal. Lett., 150 (2020) 2045-2055.

[44] X. Liu, P. Ramírez de la Piscina, J. Toyir, N. Homs, $CO_2$ reduction over Cu-ZnGaMO (M = Al, Zr) catalysts prepared by a sol-gel method: Unique performance for the RWGS reaction, Catal. Today, 296 (2017) 181-186.

[45] W. Kim, G. Yuan, B.A. McClure, H. Frei, Light Induced Carbon Dioxide Reduction by Water at Binuclear ZrOCoII Unit Coupled to Ir Oxide Nanocluster Catalyst, J. Am. Chem. Soc., 136 (2014) 11034-11042.

[46] M. Mishra, S. Krishna T. C, N. Aggarwal, M. Kaur, S. Singh, G. Gupta, Pit assisted oxygen chemisorption on GaN surfaces, PCCP, 17 (2015) 15201-15208.

[47] B. Murugan, A.V. Ramaswamy, Defect-Site Promoted Surface Reorganization in Nanocrystalline Ceria for the Low-Temperature Activation of Ethylbenzene, J. Am. Chem. Soc., 129 (2007) 3062-3063.

[48] H. Robatjazi, H. Zhao, D.F. Swearer, N.J. Hogan, L. Zhou, A. Alabastri, M.J. McClain, P. Nordlander, N.J. Halas, Plasmon-induced selective carbon dioxide conversion on earth-abundant aluminum-cuprous oxide antenna-reactor nanoparticles, Nature Communications, 8 (2017) 27.

[49] Y.F. Li, W. Lu, K. Chen, P. Duchesne, A. Jelle, M. Xia, T.E. Wood, U. Ulmer, G.A. Ozin, Cu Atoms on Nanowire $Pd/H_yWO_{3-x}$ Bronzes Enhance the Solar Reverse Water Gas Shift Reaction, J. Am. Chem. Soc., 141 (2019) 14991-14996.

[50] Y. Yu, R. Jin, J. Easa, W. Lu, M. Yang, X. Liu, Y. Xing, Z. Shi, Highly active and stable copper catalysts derived from copper silicate double-shell nanofibers with strong metal–support interactions for the RWGS reaction, Chem. Commun., 55 (2019) 4178-4181.

[51] G. Chen, R. Gao, Y. Zhao, Z. Li, G.I.N. Waterhouse, R. Shi, J. Zhao, M. Zhang, L. Shang, G. Sheng, X. Zhang, X. Wen, L.Z. Wu, C.H. Tung, T. Zhang, Alumina-Supported CoFe Alloy Catalysts Derived from Layered-Double-Hydroxide Nanosheets for Efficient Photothermal $CO_2$ Hydrogenation to Hydrocarbons, Adv. Mater., 30 (2018).

[52] Y.F. Xu, P.N. Duchesne, L. Wang, A. Tavasoli, A.A. Jelle, M. Xia, J.F. Liao, D.B. Kuang, G.A. Ozin, High-performance light-driven heterogeneous $CO_2$ catalysis with near-unity selectivity on metal phosphides, Nat Commun, 11 (2020) 5149.

[53] L.B. Hoch, P.G. O'Brien, A. Jelle, A. Sandhel, D.D. Perovic, C.A. Mims, G.A. Ozin, Nanostructured Indium Oxide Coated Silicon Nanowire Arrays: A Hybrid Photothermal/Photochemical Approach to Solar Fuels, ACS Nano, 10 (2016) 9017-9025.

[54] Y. Qi, L. Song, S. Ouyang, X. Liang, S. Ning, Q. Zhang, J. Ye, Photoinduced Defect Engineering: Enhanced Photothermal Catalytic Performance of 2D Black $In_2O_{3-x}$ Nanosheets with Bifunctional Oxygen Vacancies, Adv. Mater., 32 (2020) e1903915.

[55] S. Kattel, P. Liu, J.G. Chen, Tuning Selectivity of $CO_2$ Hydrogenation Reactions at the Metal/Oxide Interface, J. Am. Chem. Soc., 139 (2017) 9739-9754.

[56] S. Collins, M. Baltanas, A. Bonivardi, An infrared study of the intermediates of methanol synthesis from carbon dioxide over Pd/β-GaO, J. Catal., 226 (2004) 410-421.

[57] G. Finos, S. Collins, G. Blanco, E. del Rio, J.M. Cíes, S. Bernal, A. Bonivardi, Infrared spectroscopic study of carbon dioxide adsorption on the surface of cerium–gallium mixed oxides, Catal. Today, 180 (2012) 9-18.

[58] N.C. Nelson, M.-T. Nguyen, V.-A. Glezakou, R. Rousseau, J. Szanyi, Carboxyl intermediate formation via an in situ-generated metastable active site during water-gas shift catalysis, Nature Catalysis, 2 (2019) 916-924.

[59] T.H. Tan, B. Xie, Y.H. Ng, S.F.B. Abdullah, H.Y.M. Tang, N. Bedford, R.A. Taylor, K.-F. Aguey-Zinsou, R. Amal, J. Scott, Unlocking the potential of the formate pathway in the photo-assisted Sabatier reaction, Nature Catalysis, 3 (2020) 1034-1043.

[60] M. Li, U. Tumuluri, Z. Wu, S. Dai, Effect of Dopants on the Adsorption of Carbon Dioxide on Ceria Surfaces, ChemSusChem, 8 (2015) 3651-3660.

# Chapter 3 Metal oxide-modified Cu/MgO-$Al_2O_3$ catalyst for efficient and stable photothermal catalytic $CO_2$ conversion

## 3.1 Introduction

Photothermal catalytic $CO_2$ conversion to valuable fuels and chemicals has attracted considerable interest due to its promising perspective for utilizing clean solar energy and alleviating global environmental problems meanwhile.[1-3] Recently, photothermal catalytic reverse water gas shift reaction (RWGS, $CO_2 + H_2 \rightarrow CO + H_2O$) has emerged as a prospective technology to provide CO as the feedstock for highly valuable chemical products.[4-8] Many efforts have been taken to develop various efficient photothermal catalysts for CO production from $CO_2$ hydrogenation under mild conditions.[9-14] Cu is recognized as a promising catalyst among the reported efficient photothermal catalysts due to its great light-harvesting ability, high selectivity to CO, and low cost for large-scale application.[8, 15, 16] However, the relatively high reaction temperature and water generation in the process could result in the aggregation of copper, thus deactivating the catalysts in long-time operation.[17, 18] Although some research has been focused on the construction of long-term stable Cu-based photothermal catalysts, the development of highly efficient RWGS catalysts with excellent stability remains challenging.[13]

One universal strategy to enhance the stability of catalysts is to fabricate metal-based catalysts with high dispersion via the modulation of the interaction between metal and oxide support, which could stabilize the nanostructures of catalysts and alleviate the aggregation of active metals.[19-21] Over the past several years, layer double hydroxide (LDH) has been reported to act as a platform to synthesize well-dispersed metal/oxide nanocomposites, due to its versatile chemical composition and orderly structural architecture.[22-26] Previous studies demonstrated that Cu-based catalysts derived from LDH exhibit enhanced metal-support interaction, promoted activity and stability in various catalytic processes.[25, 27] Recently, it is found that the hydrothermal stability of Pd/$MgAl_2O_4$ catalyst could be promoted by the addition of irreducible oxides on the

surface, which inhibits the deep oxidation of Pd and preserves the suitable active phase of Pd-$PdO_x$ in the catalyst.[19] This enlightens me that ultra-stable Cu-based photothermal catalysts might be established by the same strategy. Therefore, the elaborate design of metal oxide-modified Cu-based photothermal catalysts derived from LDH is expected to achieve the high dispersion and stable nanostructures of Cu species, while relative works are still rare, emphasizing the necessity of further investigation in this field.

In this chapter, I utilize a joint strategy to fabricate a series of metal oxide-modified Cu/MgO-$Al_2O_3$ photothermal catalysts derived from CuMgAl-LDH followed by the impregnation of metal nitrate precursors. Due to the highly dispersed Cu and stabilization by the addition of metal oxide ($ZrO_2$), the catalysts show not only efficient activity of CO production but also long-term stability during the photothermal catalytic RWGS reaction. Detailed study demonstrates that the addition of metal oxide stabilizes the architecture of Cu nanoparticles and prevents the aggregation of active Cu, thus preserving the active sites of catalysts during the reaction process. This finding provides a facile technology for the design of efficient photothermal catalysts with excellent stability.

## 3.2 Experimental section

### 3.2.1 Materials

All chemicals were utilized as received without further purification. Magnesium(II) nitrate hexahydrate ($Mg(NO_3)_2 \cdot 6H_2O$), copper(II) nitrate trihydrate ($Cu(NO_3)_2 \cdot 3H_2O$), aluminum(III) nitrate nonahydrate ($Al(NO_3)_3 \cdot 9H_2O$), cerium(III) nitrate hexahydrate ($Ce(NO_3)_3 \cdot 6H_2O$), zirconium(IV) dinitrate oxide hydrate ($ZrO(NO_3)_2 \cdot xH_2O$), sodium hydroxide (NaOH), sodium carbonate ($Na_2CO_3$), commercial MgO, commercial $Al_2O_3$ and ethylene glycol (EG) were provided by Wako Chemical Co., Ltd. Distilled water (18.2 MΩ cm) was applied in this chapter .

### 3.2.2 Catalysts preparation

***Synthesis of $Cu_xMg_yAl$-LDH.*** A series of CuMgAl-LDH with different ratios of Cu and Mg (Cu/Mg = x/y = 1/1, 1/2, 1/4, 1/9, 1/14) were synthesized by a co-deposition method according to the previous reports.[27] The ratio between $[Cu^{2+}]$ + $[Mg^{2+}]$ and $[Al^{3+}]$ was determined to be 3/1 in order to fabricate a stable LDH structure. Typically, for $Cu_{0.6}Mg_{2.4}Al$-LDH (x/y = 1/4), 1.268 g $Cu(NO_3)_2{\cdot}3H_2O$, 5.385 g $Mg(NO_3)_2{\cdot}6H_2O$ and 3.282 g $Al(NO_3)_3{\cdot}9H_2O$ was dissolved into 35 mL ultrapure water to obtain solution A, with the concentration of metal cations ($[Cu^{2+}]$ + $[Mg^{2+}]$ + $[Al^{3+}]$) to be 1 mol $L^{-1}$. Solution B was obtained by dissolving 2.24 g NaOH and 1.855 g $Na_2CO_3$ into 35 mL water with the ratio of [NaOH] = 1.6 mol $L^{-1}$ and $[CO_3^{2-}] = 2[Al^{3+}]$. Solution A and B were simultaneously added into a clean beaker with a magnetic stirrer rotating at 1000 rpm and mixed for 5 min. Then the blue slurry was moved to a 100 mL Teflon-lined stainless-steel autoclave and heated at 100 °C for 48 h. After the reaction finished, the autoclave was cooled to room temperature. The blue precipitates were collected by centrifugation and washed with distilled water until pH = 7, then dried at 70 °C in a vacuum oven overnight. The detailed amount of chemicals was listed in Table 3.1.

**Table 3.1** Detailed amount of chemicals utilized in the synthesis of LDH precursors

| Cu/Mg in LDH | Solution A | | | Solution B | |
|---|---|---|---|---|---|
| | $Cu(NO_3)_2{\cdot}3H_2O$ | $Mg(NO_3)_2{\cdot}6H_2O$ | $Al(NO_3)_3{\cdot}9H_2O$ | NaOH | $Na_2CO_3$ |
| 1/1 | 3.171 g | 3.365 g | 3.282 g | 2.24 g | 1.855 g |
| 1/2 | 2.114 g | 4.48 | 3.282 g | 2.24 g | 1.855 g |
| 1/4 | 1.268 g | 5.385 g | 3.282 g | 2.24 g | 1.855 g |
| 1/9 | 0.634 g | 5.946 g | 3.282 g | 2.24 g | 1.855 g |
| 1/14 | 0.317 g | 6.276 g | 3.282 g | 2.24 g | 1.855 g |

***Synthesis of $Cu_x/MgO$-$Al_2O_3$ (Cu/MA).*** The above precursors $Cu_xMg_yAl$-LDH were annealed at 400 °C for 4 h in air with a ramping rate of 5 °C $min^{-1}$ to obtain CuO/MgO-

$Al_2O_3$ powders, and then the samples were reduced in 10% $H_2$/Ar atmosphere at 300 $^oC$ for 1 h with a ramping rate of 5 $^oC$ $min^{-1}$ to obtain $Cu_x$/MA catalysts.

***Synthesis of $Cu_x$@MO/MgO-$Al_2O_3$ (Cu@M/MA).*** MO = $CeO_2$, $ZrO_2$ and $Al_2O_3$. The $Cu_x$@M/MA was synthesized based on the optimized $Cu_x$/MA catalyst. Typically, for $Cu_x$@Ce/MA, 1 g $Cu_x$/MA was dispersed into 20 mL ethylene glycol (EG) with Ar ventilation. Then 1.08 g $Ce(NO_3)_3 \cdot 6H_2O$ was added into the above solution. After vigorous stirring for 4 h, the solution was allowed to stand for 30 min to collect the bottom deposition. Then it was dried at 70 $^oC$ overnight in a vacuum oven. After annealing at 400 $^oC$ for 2 h in air with a ramping rate of 5 $^oC$ $min^{-1}$, the sample was reduced in 10% $H_2$/Ar atmosphere at 300 $^oC$ for 1 h to obtain Cu@Ce/MA catalyst. Cu@Zr/MA and Cu@Al/MA were synthesized by the same procedure except for the change from $Ce(NO_3)_3 \cdot 6H_2O$ to $Zr(NO_3)_4 \cdot 5H_2O$ and $Al(NO_3)_3 \cdot 9H_2O$, respectively.

***Synthesis of reference catalysts.*** $Cu_{0.6}$/MA-wet was obtained through the initial air-calcination of MgAl-LDH precursors, followed by the wet impregnation of $Cu(NO_3)_2$ solution and annealing at 400 $^oC$ in air for 2 h. The synthesis of $Cu_{0.6}$/MgO and $Cu_{0.6}/Al_2O_3$ was similar to that for $Cu_{0.6}$/MA-wet except for the support was changed to commercial MgO and $Al_2O_3$, respectively.

### 3.2.3 Characterization

A PANalytical B.V. XRD diffractometer with Cu Kα radiation (λ = 1.5406 Å) was utilized to obtain the powder X-ray diffraction (XRD) results. The Cu, Mg, Al, Ce and Zr content in catalysts were analyzed via inductively coupled plasma-optical emission spectrometry (ICP-OES, Agilent 720-ES). A JEOL JEM-F200 (HR) transmission electron microscopy operated at 200 kV was utilized to collect the transmission electron micrography (TEM) and high-resolution TEM (HRTEM) images of catalysts. The elemental distribution of samples was recorded through energy-dispersive X-ray spectroscopy (EDS) test on the above TEM equipment. The Thermo Fisher ESCALAB Xi+ system was utilized to collect X-ray photoelectron spectroscopy (XPS) of samples. A Shimadzu UV-2500 spectrometer with an integrating sphere accessory was used to

obtain the UV-Visible diffuse reflectance spectroscopy (UV-Vis DRS). $H_2$-TPR test was conducted on an AutoChem II 2920 chemisorption system. 50 mg catalyst was initially pretreated by Ar (20 mL $min^{-1}$) at 150 $^oC$ for 1 h, followed by cooling down to 50 $^oC$. Then, 10%$H_2$/Ar (20 mL $min^{-1}$) was introduced to the system and the temperature increased from 50 $^oC$ to 400 $^oC$ with the ramping rate of 5 $^oC$ $min^{-1}$. $N_2O$ chemisorption test was also conducted on the AutoChem II 2920 chemisorption system using the procedure described by previous work.[25]

### 3.2.4 Catalytic activity evaluation

Solar-driven photothermal catalytic $CO_2$ reduction experiment was carried out in a home-made quartz reactor, which has been described in chapter 2. A 300 W Xenon arc lamp was applied as the illuminant and the only energy input. A Thorlabs PM-100D optical power meter with an S401C sensor was utilized to measure the intensity of. During the experiment, 10 mg catalyst was first reduced in a flow of 10% $H_2$/Ar at 300 $^oC$ for 1 h, and then was smoothly dispersed onto an air-permeable quartz fiber filter in the reactor. A thermocouple located at the center of sample surface was utilized to monitor the temperature of catalyst. The mixed reaction gas ($CO_2$/$H_2$ = 1:1) flowed through the system with a rate of 20 mL $min^{-1}$. After purging for 0.5 h, the light was switched on to initial the solar-driven experiment. The venting gas was injected into a gas chromatography (Shimadzu GC2014) to analyze the components. The CG was equipped with two capillary columns (porapak-Q and shincarbon-A) and a flame ionization (FID) detector.

The solar energy conversion efficiency (η) was calculated by the following formula[28]:

$$\eta = \frac{r(CO) \times \Delta_f H^0_{CO} + r(H_2O) \times \Delta_f H^0_{H_2O} - r(H_2) \times \Delta_f H^0_{H_2} - r(CO_2) \times \Delta_f H^0_{CO_2}}{P_{irradiation}} \times 100\%$$

where $P_{irradiation}$ is the energy power of input light. r(x) is the reaction rate of reactant or product x, and $\Delta_f H^0$ is relevant standard enthalpy of formation. The $\Delta_f H^0$ for $CO_2$, $H_2$,

$H_2O$ and CO are -393.8, 0, -242 and -110.6 kJ $mol^{-1}$. In this chapter, the main product was CO with almost 100% selectivity. Thereby, the r(x) of $CO_2$, $H_2$, $H_2O$ and CO was considered to be the same for the calculation of η.

Photo-assisted thermocatalytic $CO_2$ hydrogenation reaction was carried out in a flow-type stainless-steel reaction system with external electric heating, which has also been described in chapter 2. The catalyst temperature was controlled by a temperature controller (TC-1000 JASCO) and a thermocouple. The visible light source was an LA-251 Xe lamp with L42 and HA30 filters. Specifically, 10 mg sample was uniformly dispersed onto the sample holder and reduced in 10% $H_2$/Ar atmosphere at 300 $^oC$ for 1 h. Then a gas mixture ($CO_2/H_2$ = 1/1) flowed through the reaction system with a rate of 20 mL $min^{-1}$. After purging for 30 min, the electrical heater was turned on to elevate the reactor temperature in a ramping rate of 5 $^oC$ $min^{-1}$. The analysis of products was the same as the above experiment.

### 3.2.5 In situ DRIFTS analysis

A JASCO FT-IR 6300 Spectrometers equipped with a liquid nitrogen-cooled mercury-cadmium-telluride (MCT) detector and an in situ diffuse reflectance cell was utilized to conduct in situ diffuse reflectance infrared Fourier transform spectroscopy (DRIFTS) test. DRTFTS spectra were recorded at 4 $cm^{-1}$ resolution with 32 scans. Before the experiment, 10 mg catalyst was in-situ reduced by 10%$H_2$/Ar at 300 $^oC$ for 1 h, and then cooled to room temperature in Ar atmosphere. The background spectrum was recorded in Ar at 30 $^oC$, and afterwards the gas flow was changed into the reaction gas ($CO_2/H_2$ = 1/1, 20 mL $min^{-1}$). Then the heating system was turned on to elevate the reaction temperature under irradiation with a ramping rate of 10 $^oC$ $min^{-1}$. Each spectrum was obtained after the reaction stage was maintained for 30 min.

The light enhancement mechanism in photothermal RWGS reaction was further investigated by analyzing the DRIFTS spectra of the process in dark and light conditions at 250 $^oC$ over the optimized catalyst. Specially, 10 mg catalyst was initially reduced and then the reaction gas mixture ($CO_2/H_2$ = 1/1) was introduced into the

reaction system. After the fully absorption of reactants on the catalyst surface, the reaction system was closed and the DRIFTS spectra were collected with or without light irradiation at 250 $^{o}$C.

## 3.3 Results and discussion

### 3.3.1 Photothermal catalytic activity measurement

In this chapter, a series of $Cu_x/MgO-Al_2O_3$ (noted as $Cu_x/MA$, x is the stoichiometric ratio of Cu in relative precursors) catalysts were synthesized for the photothermal catalytic $CO_2$ reduction with $H_2$, and the results were shown in Figure 3.1. With the light irradiation with the intensity of 1.88 W $cm^{-2}$ from a 300 W Xenon lamp, CO was the main product among all catalysts (selectivity > 99%) with only a small portion of methanol as the side product. Obviously, with the increase of Cu amount in catalysts (x from 0.15 to 0.6), the CO production was enhanced at first because of the increase of active Cu sites in catalysts and $Cu_{0.6}/MA$ showed an excellent activity with 84.8 mmol $g^{-1}$ $h^{-1}$ CO production. While further increasing the amount of copper (x from 0.6 to 1.5), the catalytic activity rapidly decreased, possibly due to the increasing size of Cu nanoparticles. For comparison, reference catalysts ($Cu_{0.6}/MA$-wet, $Cu_{0.6}/MgO$ and $Cu_{0.6}/Al_2O_3$) were synthesized by wet impregnation method and their photothermal catalytic CO production was quite lower than the optimized $Cu_{0.6}/MA$, implying the catalysts derived from LDH exhibited stronger metal-support interaction, which promoted the conversion of $CO_2$ to CO. Then the optimized catalyst $Cu_{0.6}/MA$ was utilized for the long-term photothermal RWGS reaction. As shown in Figure 3.2, after 6 h reaction process, the production of CO gradually decreased to 70.0 mmol $g^{-1}$ $h^{-1}$, with only ~80% remaining compared with the fresh catalyst. The unsatisfying stability of the catalyst propelled me to find an approach to modulate the $Cu_{0.6}/MA$ catalyst for better performance.

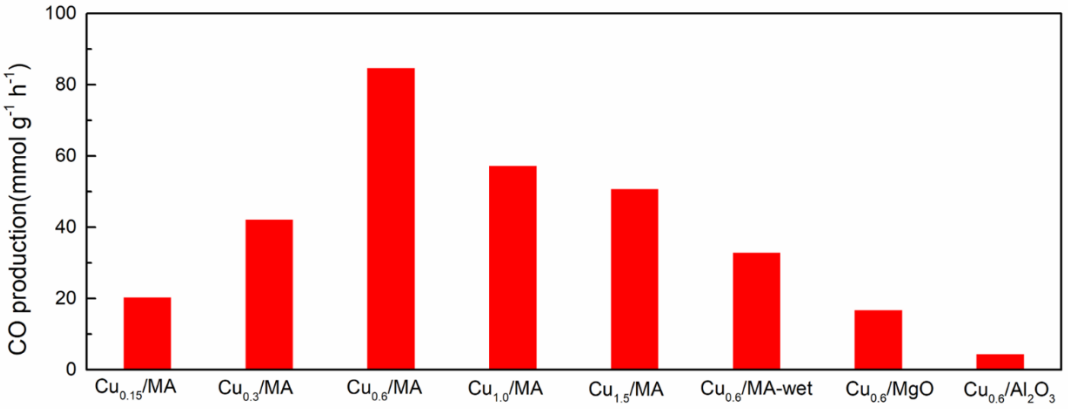


**Figure 3.1** Photothermal catalytic RWGS activity over different catalysts at 1.88 W $cm^{-2}$. $CO_2/H_2$ = 10/10 mL $min^{-1}$.

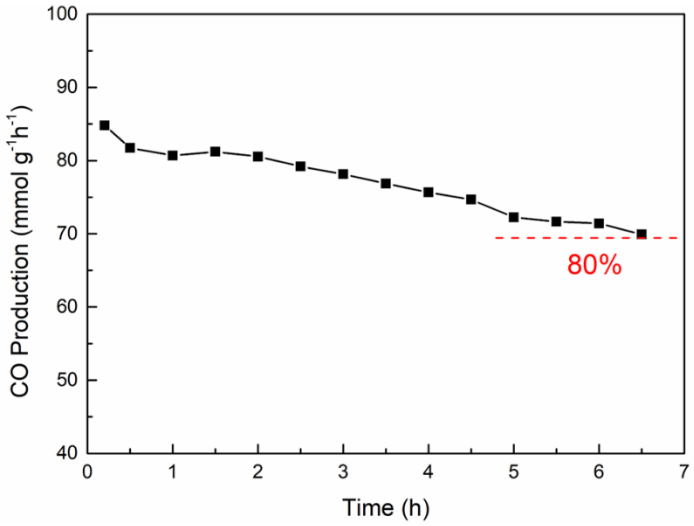


**Figure 3.2** Stability test of photothermal catalytic CO production on $Cu_{0.6}$/MA.

On the base of previous reports, I utilized an oxide-modified strategy to enhance the stability of catalysts and then fabricated a series of $Cu_{0.6}$@MO/MgO-$Al_2O_3$ (noted as $Cu_{0.6}$@M/MA, M = $CeO_2$, $ZrO_2$, $Al_2O_3$) by impregnation.[19] Photothermal catalytic $CO_2$ reduction was carried out on the above catalysts, and the results were shown in Figure 3.3. The temperatures of catalysts were recorded by a thermocouple and Figure 3.3a depicted a linear relationship between the light intensity and the equilibrium temperature of catalysts. All catalysts exhibited a similar equilibrium temperature at the same light intensity, indicating that the introduction of metal oxides did not change the light-to-heat conversion ability of catalysts. CO was still the main product among all catalysts, suggesting that the reaction selectivity of photothermal catalytic $CO_2$

hydrogenation was not altered by the addition of metal oxides. Figure 3.3b showed the CO production rates under different irradiation intensities. Compared with $Cu_{0.6}$/MA, it could be concluded that the introduction of $CeO_2$ and $ZrO_2$ promoted the RWGS reaction while additional $Al_2O_3$ inhibited the CO generation to some degree. Obviously, $Cu_{0.6}$@Zr/MA exhibited the highest CO production of 125.7 mmol $g^{-1}$ $h^{-1}$ at the light intensity of 1.88 W $cm^{-2}$, increased by ~50 % than the $Cu_{0.6}$/MA catalyst at the same condition (84.8 mmol $g^{-1}$ $h^{-1}$), while $Cu_{0.6}$@Ce/MA showed a performance of 90.7 mmol $g^{-1}$ $h^{-1}$ CO production, only a slight enhancement in reaction activity. I also calculated the conversion efficiency (η) of solar energy in RWGS reaction on catalysts, which could be defined as the efficiency of converting solar energy into chemical energy in the form of reaction enthalpy. As shown in Figure 3.3c, due to the excellent performance in reaction, the η of $Cu_{0.6}$@Zr/MA attained 0.97% with the light intensity of 1.88 W $cm^{-2}$.

Since $Cu_{0.6}$@Zr/MA catalyst could achieve superior photothermal RWGS activity, I further investigated the stability of the optimized catalyst in the long-time reaction process. As shown in Figure 3.3d, the CO production on $Cu_{0.6}$@Zr/MA was almost stable after 8 h reaction, and the activity still remained 93% compared with the fresh catalyst after 12 h continuous process. Obviously, the stability of catalyst was significantly enhanced via the oxide-modification strategy, possibly due to the stabilization of Cu nanostructure by the modulation of $ZrO_2$, and the optimized $Cu_{0.6}$@Zr/MA catalyst showed an outstanding photothermal $CO_2$ reduction performance compared with reported works (Table 3.2). The detailed origins of improved activity and stability of catalysts by $ZrO_2$ would be investigated in the following part of this chapter.

**Table 3.2** Comparison of catalytic performance for some RWGS catalysts

| Entry | Catalyst | Gas composition | Catalytic condition | CO production rate | Stability | Ref. |
|---|---|---|---|---|---|---|
| 1 | $Cu_{0.6}$@Zr/MA | $CO_2/H_2$ = 50/50<br>20 mL $min^{-1}$ | 300 W Xe lamp<br>(1.88 W $cm^{-2}$) | 125.7 mmol $g_{cat}^{-1}$ $h^{-1}$ | 93% (12 h) | This chapter |
| 2 | $Cu_{0.6}$/MA | $CO_2/H_2$ = 50/50<br>20 mL $min^{-1}$ | 300 W Xe lamp<br>(1.88 W $cm^{-2}$) | 84.8 mmol $g_{cat}^{-1}$ $h^{-1}$ | 80% (6.5h) | This chapter |
| 3 | 10Cu5Ga/$CeO_2$ | $CO_2/H_2$ = 50/50<br>20 mL $min^{-1}$ | 300 W Xe lamp<br>(1.95 W $cm^{-2}$) | 111.2 mmol $g_{cat}^{-1}$ $h^{-1}$ | 70% (10 h) | Chapter 2 |
| 4 | CF-$Cu_2O$ | $CO_2/H_2$ = 83/17<br>43 mL $min^{-1}$ | Visible light, LED light,<br>5.0 W $cm^{-2}$, 4 bars | 139.6 mmol $g_{cat}^{-1}$ $h^{-1}$ | 75% (30 h) | [7] |
| 5 | $Cu_1Ca_9(PO_4)_6(OH)_2$ | $CO_2/H_2$ = 50/50<br>2 mL $min^{-1}$ | 300 W Xe lamp<br>(2.0 W $cm^{-2}$), 300 °C | 0.84 mmol $g_{cat}^{-1}$ $h^{-1}$ | 77% (20 h) | [13] |
| 6 | Al@$Cu_2O$ | $CO_2/H_2$ = 50/50<br>10 mL $min^{-1}$ | supercontinuum fiber laser (10 W $cm^{-2}$) | 2.03 mmol $g_{cat}^{-1}$ $h^{-1}$ | - | [12] |
| 7 | Cu/Pd/$H_yWO_{3-x}$ | $CO_2/H_2$ = 50/50<br>4 mL $min^{-1}$ | 120 W Xe lamp,<br>2.0 W $cm^{-2}$, 250 °C | 1.18 mmol $g_{cat}^{-1}$ $h^{-1}$ | 83% (10 h) | [15] |
| 8 | CuSiO/$CuO_x$ | $CO_2/H_2/Ar$ = 24/72/4<br>20 mL $min^{-1}$ | 500 °C | 40.4 mmol $g_{cat}^{-1}$ $h^{-1}$ | - | [29] |
| 9 | $Ni_{12}P_5/SiO_2$ | $CO_2/H_2$ = 5/1<br>3 mL $min^{-1}$ | 0.8 W $cm^{-2}$,<br>290 °C | 13.5 mmol $g_{cat}^{-1}$ $h^{-1}$ | 89% (40 h) | [30] |

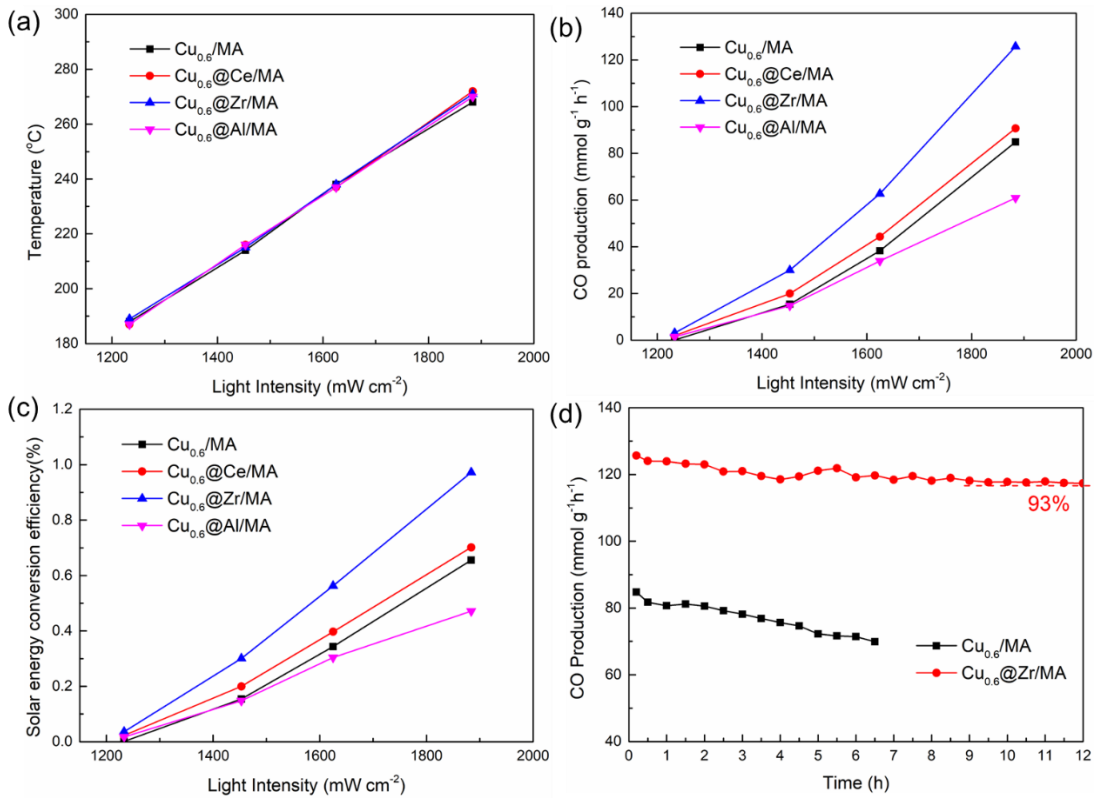


**Figure 3.3** Solar-driven photothermal catalytic RWGS reaction. (a) Catalyst temperatures with different light intensities, (b) photothermal CO production and (c) solar energy conversion efficiency over $Cu_{0.6}$@M/MA catalysts, (d) durability test of $Cu_{0.6}$/MA and $Cu_{0.6}$@Zr/MA under the irradiation of 1.88 W·cm$^{-2}$.

### 3.3.2 Characterization of catalysts

The structure and morphology of CuMgAl-LDH precursors were analyzed by SEM images, as displayed in Figure 3.4a and b. Generally, the images illustrated the disk shape of LDH materials with around 100 nm in diameter. After annealing in air and modified by $ZrO_2$, the SEM patterns suggested the morphology of $Cu_{0.6}$/MA and $Cu_{0.6}$@Zr/MA was similar, inherited from the LDH precursors, implying that the morphology was not changed by the modulation of $ZrO_2$ (Figure 3.4c and d). Figure 3.5 showed the XRD patterns of $Cu_{0.6}$@M/MA, illustrating the existence of metallic Cu (JCPDS No. 04-0836) and MgO (JCPDS No. 65-0476), while no peaks belonging to $Al_2O_3$ were detected, suggesting the amorphous phase of $Al_2O_3$ in catalysts. Furthermore, the additional metal oxide ($CeO_2$, $ZrO_2$, $Al_2O_3$) also exhibited no

diffraction peaks in XRD patterns, possibly due to their relatively low amount according to ICP-OES results (Table 3.3). High-resolution TEM (HRTEM) images depicted the nanostructure of catalyst $Cu_{0.6}$/MA and $Cu_{0.6}$@Zr/MA, as shown in Figure 3.6. In $Cu_{0.6}$/MA (Figure 3.6a), the lattice fringes of 0.21 nm could be attributed to the (200) plane of MgO and (111) plane of Cu nanoparticles, and MgO (220) facet was also observed with the lattice fringes of 0.15 nm. No lattice fringes belonging to $Al_2O_3$ could be observed in catalyst, indicating the amorphous phase of $Al_2O_3$, in correspondence with XRD data. Energy dispersive X-ray spectrometry (EDS) images in Figure 3.6b showed that Cu was well dispersed in the catalysts, mainly as nanoparticles on the MgO-$Al_2O_3$ support. After the introduction of Zr species, Figure 3.6c exhibited similar lattice fringes assigned to Cu and MgO, indicating that Zr did not change the nanoarchitecture between Cu NPs and support. Typically, the lattice fringes of 0.29 nm were observed near the Cu NPs, which could be assigned to $ZrO_2$ (111) facet, suggesting the direct interplay between Cu NPs and additional $ZrO_2$. Furthermore, the EDS patterns of $Cu_{0.6}$@Zr/MA (Figure 3.6d) showed that Cu and Zr elements were uniformly dispersed on the surface of catalyst, implying the loading of $ZrO_2$ stabilized the nanostructure of Cu nanoparticles and thereby promoted the stability of catalyst.

**Table 3.3** Element composition and physical properties of catalysts

| Catalyst | wt% of Cu[a] | wt% of Metal[a] | $D_{Cu}$ (%) [b] |
|---|---|---|---|
| $Cu_{0.6}$/MA | 15.7 | - | 78.0 |
| $Cu_{0.6}$@Ce/MA | 13.1 | 3.7 (Ce) | 18.7 |
| $Cu_{0.6}$@Zr/MA | 12.6 | 4.4 (Zr) | 61.1 |
| $Cu_{0.6}$@Al/MA | 13.8 | 14.4 (Al) | 49.7 |
| Used $Cu_{0.6}$/MA | - | - | 60.1 |
| Used $Cu_{0.6}$@Zr/MA | - | - | 58.6 |

[a] analyzed by ICP-OES, [b] calculated from $N_2O$ chemisorption results

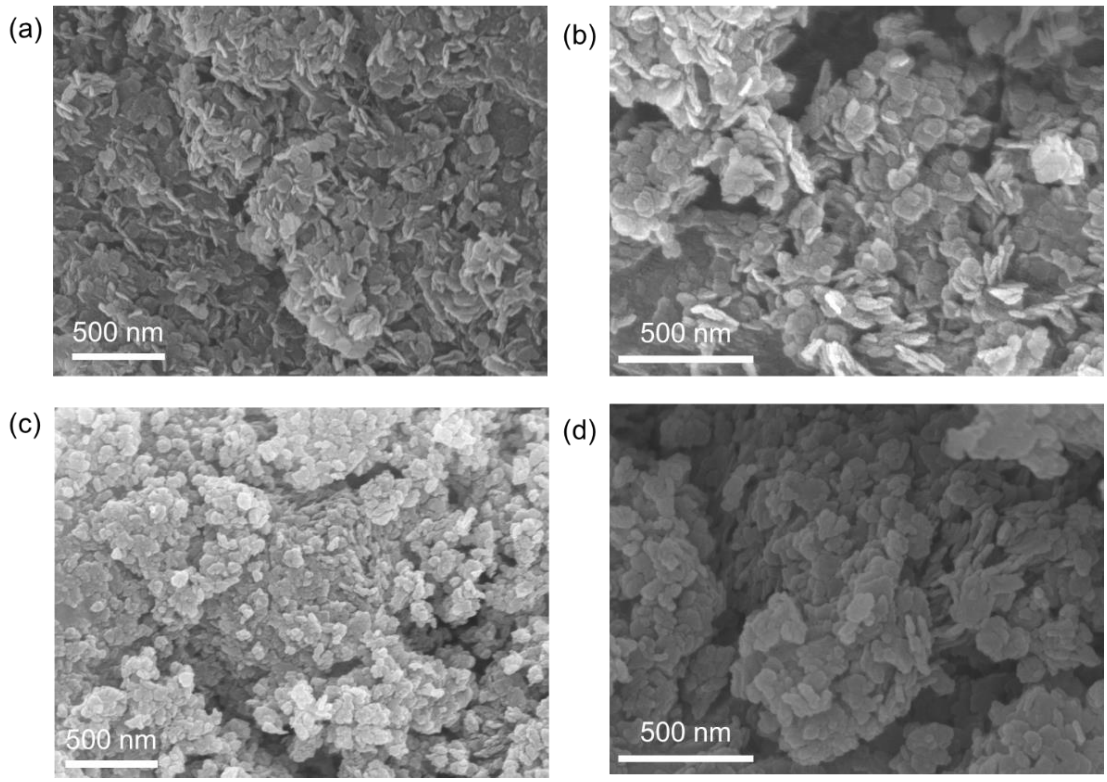


**Figure 3.4** SEM patterns of (a) and (b) CuMgAl-LDH precursors, (c) $Cu_{0.6}$/MA and (d) $Cu_{0.6}$@Zr/MA catalysts.

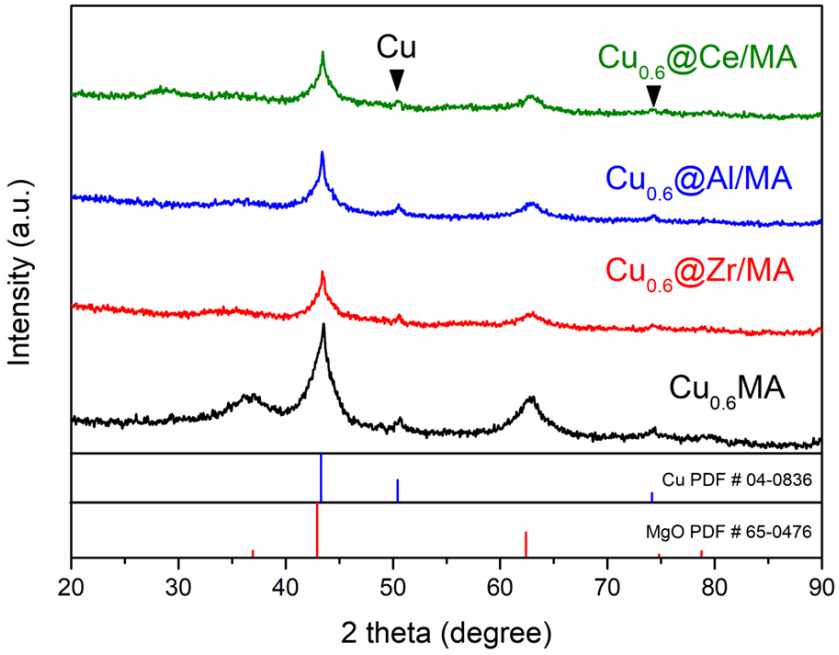


**Figure 3.5** XRD patterns of $H_2$-reduced $Cu_{0.6}$/MA and $Cu_{0.6}$@M/MA (M = Ce, Zr, Al) catalysts.

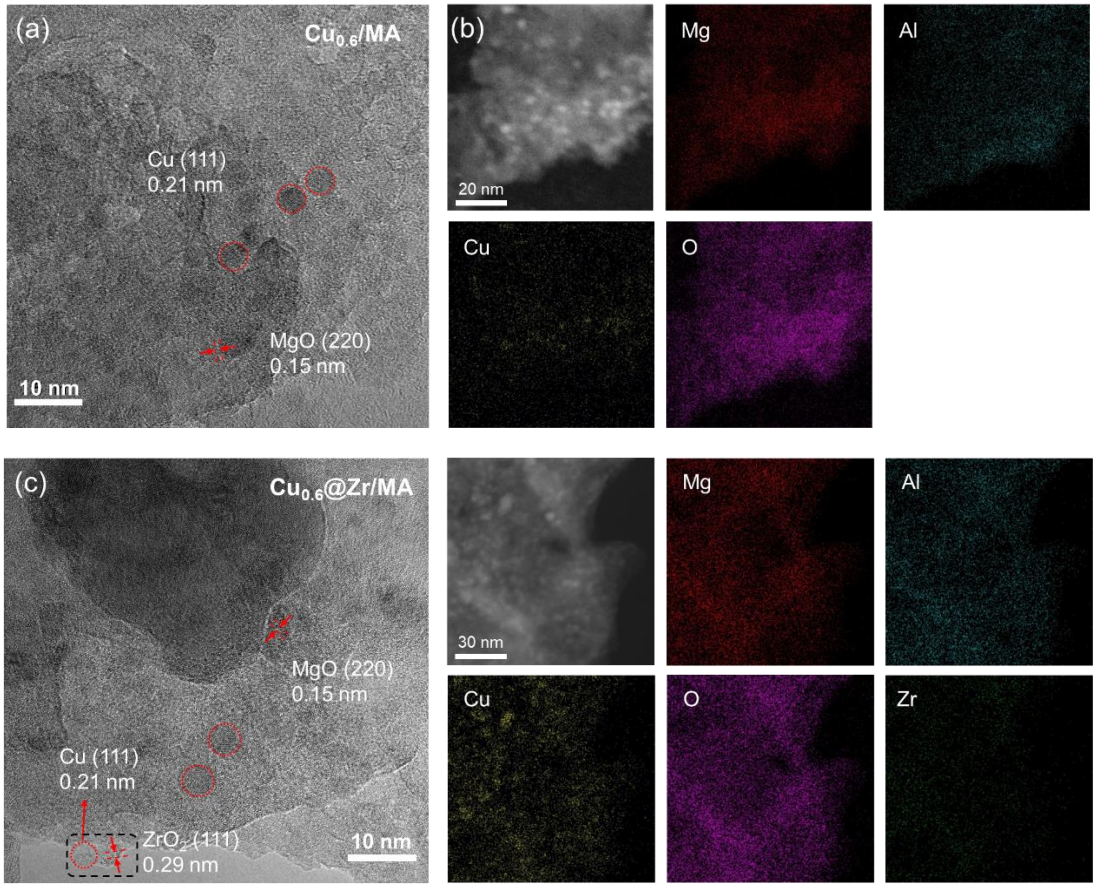


**Figure 3.6** HRTEM (a and c) and EDS (b and d) images for $Cu_{0.6}$/MA (a and b) and $Cu_{0.6}$@Zr/MA (c and d) catalyst.

The reducing behaviors of catalysts in $H_2$ atmosphere was investigated by $H_2$-temperature-programmed reduction ($H_2$-TPR) experiment, and the results were shown in Figure 3.7. The $Cu_{0.6}$/MA catalyst showed two peaks centered at 196 and 217 $^oC$, which could be attributed to the reduction of surface CuO and $Cu_2O$, respectively. After the introduction of metal oxides, the intensity of reducing peaks of Cu species in catalysts was decreased to some degree, possibly due to the cover of oxides on the catalyst surface, especially on the Cu nanoparticles. Typically, the reducing peaks in $Cu_{0.6}$@Ce/MA and $Cu_{0.6}$@Zr/MA shifted to lower temperatures, which could be attributed to the interaction between $ZrO_2$/$CeO_2$ and Cu. As for $Cu_{0.6}$@Al/MA, the reducing peaks of Cu shifted to higher temperatures (217 and 234 $^oC$), implying the addition of $Al_2O_3$ inhibited the reduction of $Cu^{2+}$ to $Cu^0$, therefore decreasing the activity of catalyst. Furthermore, the $N_2O$ chemisorption method was utilized to analyze

the dispersion of Cu ($D_{Cu}$), which was defined as the ratio of Cu atoms exposed at the surface to total Cu atoms and a higher $D_{Cu}$ suggested more active sites on Cu NPs.[25] As listed in Table 3.3, the $D_{Cu}$ of $Cu_{0.6}$/MA was 78.0%, suggesting the high dispersion of copper in the catalyst. After the introduction of metal oxides, $D_{Cu}$ of all the catalysts was decreased, especially $Cu_{0.6}$@Ce/MA (only 18.7%), which could be attributed to the strong interaction between Cu and $CeO_2$, hindering the oxidation of Cu NPs during the $N_2O$ chemisorption process. The optimized catalyst $Cu_{0.6}$@Zr/MA showed a slightly decreased $D_{Cu}$ of 61.1%, compared with $Cu_{0.6}$/MA. However, after the stability experiment, the $D_{Cu}$ of $Cu_{0.6}$/MA decreased to 60.1%, while that of $Cu_{0.6}$@Zr/MA only reduced to 58.6%, demonstrating that the introduction of $ZrO_2$ successfully alleviated the aggregation of Cu nanoparticles in the reaction process, thereby promoting the stability of catalysts.

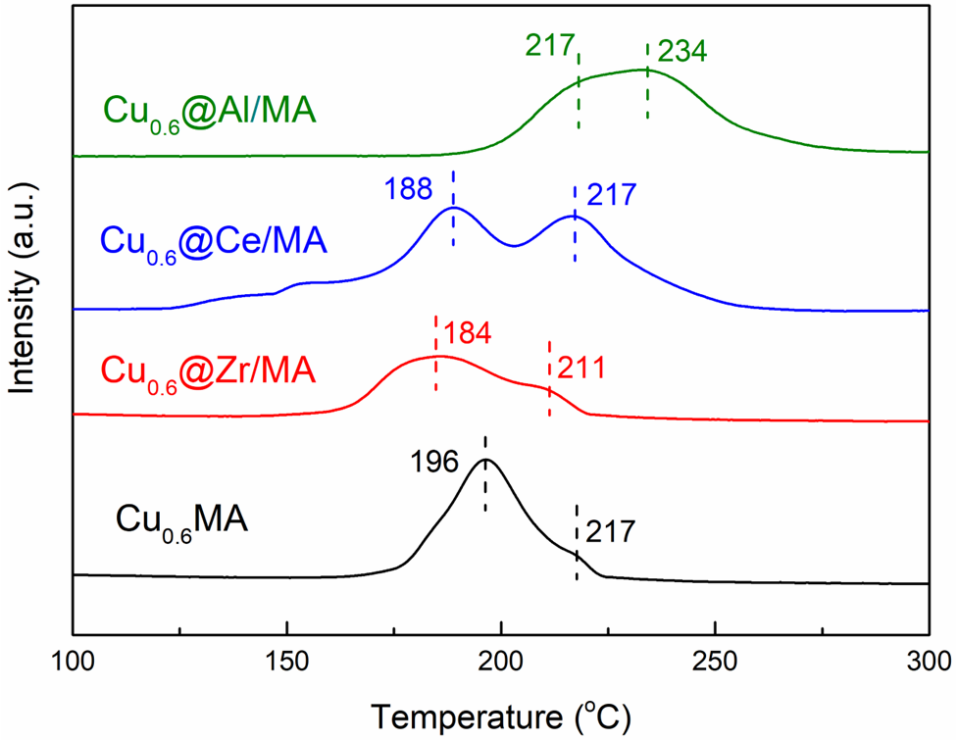


**Figure 3.7** $H_2$-TPR patterns of $Cu_{0.6}$/MA and $Cu_{0.6}$@M/MA (M = Ce, Zr, Al).

To further elucidate the influence of $ZrO_2$ on the catalyst, XPS was applied to analyze the chemical states of elements in $Cu_{0.6}$/MA and $Cu_{0.6}$@Zr/MA (Figure 3.8a-c). In the Cu 2p patterns, two peaks centered at 932.4 eV and 933.8 eV were observed, which could be assigned to $Cu^0/Cu^+$ and $Cu^{2+}$.[31] The existence of $Cu^{2+}$ was probably due to

the oxidation of $Cu^0$ by the exposure to air before XPS analysis. Both $Cu_{0.6}$/MA and $Cu_{0.6}$@Zr/MA showed similar chemical states of Cu, implying that the introduction of $ZrO_2$ did not change the electronic structure of Cu NPs. Figure 3.8c showed the XPS spectra for Zr 3d in $Cu_{0.6}$@Zr/MA, and the peak centered at 181.9 eV could be assigned to $Zr^{4+}$ in monoclinic $ZrO_2$.[32] The optical properties of $Cu_{0.6}$/MA and $Cu_{0.6}$@Zr/MA catalysts were analyzed by UV-Vis DRS. Figure 3.8 depicted a wide absorption peak centered at 590 nm in $Cu_{0.6}$/MA catalysts, which was induced by the LSPR effect of Cu NPs. As for $Cu_{0.6}$@Zr/MA, the peak position was not changed after the addition of $ZrO_2$ while the absorption spectra were flatter than $Cu_{0.6}$/MA, possibly due to the slight cover of $ZrO_2$ on the surface of Cu NPs.

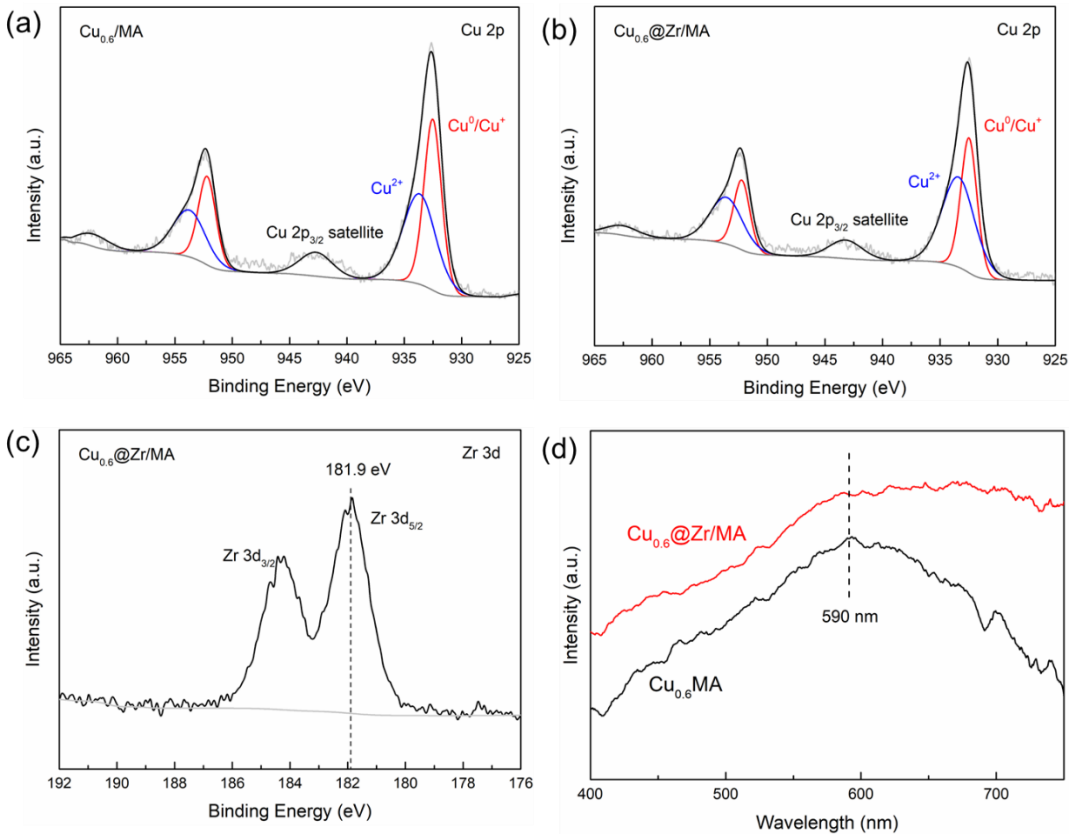


**Figure 3.8** XPS patterns of (a-c) Cu 2p and Zr 3d in $Cu_{0.6}$/MA and $Cu_{0.6}$@Zr/MA, (d) UV-Vis DRS spectra of $Cu_{0.6}$/MA and $Cu_{0.6}$@Zr/MA.

In order to further study the conditions of Cu in $Cu_{0.6}$/MA and $Cu_{0.6}$@Zr/MA catalysts, CO was utilized as a probe molecular in DRIFTS analysis. Generally, the CO absorbed on metal atoms of different chemical states showed different IR peaks due to

the tiny changes of C=O bond, which could help distinguish the physiochemical properties of metal atoms.[33-35] As shown in Figure 3.9a, three peaks centered at 2058, 2098 and 2170 $cm^{-1}$ were detected on $Cu_{0.6}$/MA. The 2170 $cm^{-1}$ could be assigned to gaseous CO, and the adsorption band at 2098 $cm^{-1}$ with a shoulder at 2058 $cm^{-1}$ was due to the CO absorbed on metallic copper $Cu^0$, indicating the different types of Cu species existed in $Cu_{0.6}$/MA. [36-40] For $Cu_{0.6}$@Zr/MA catalyst, the intensity of CO adsorption peaks was obviously diminished in comparison with $Cu_{0.6}$/MA, implying the partial cover of $ZrO_2$ on Cu NPs as suggested by chemisorption analyses. The adsorption peak at 2058 $cm^{-1}$ was not observed, illustrating the uniform dispersion of Cu NPs after the introduction of $ZrO_2$. In addition, the adsorption peak of CO-$Cu^0$ shifted to a higher wavenumber (2104 $cm^{-1}$), probably due to the interaction between Cu and $ZrO_2$, in accordance with the $H_2$-TPR results.

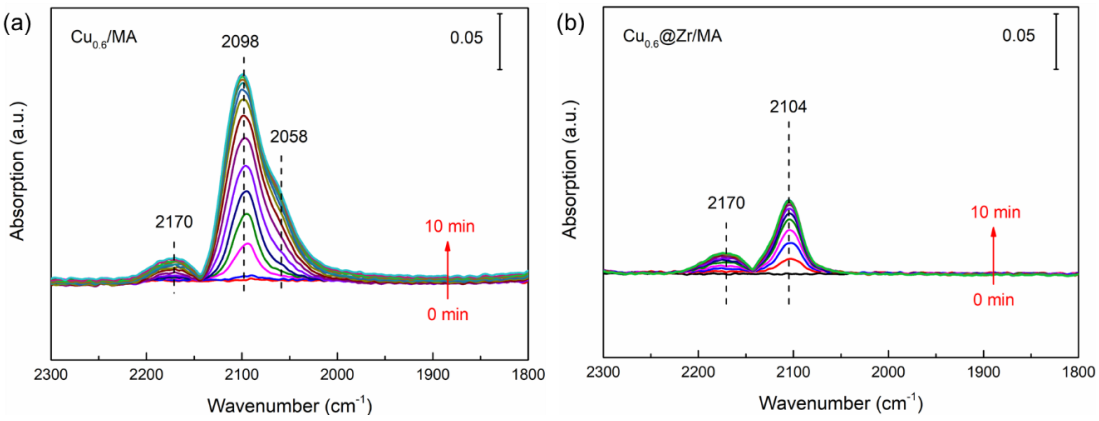


**Figure 3.9** CO-DRIFT spectra of (a) $Cu_{0.6}$/MA catalysts and (b) $Cu_{0.6}$@Zr/MA catalysts.

The reaction pathway for photothermal RWGS reaction over $Cu_{0.6}$/MA and $Cu_{0.6}$@Zr/MA catalysts was investigated by in situ DRIFTS experiment and the spectra were shown in Figure 3.10. At room temperature, both reduced $Cu_{0.6}$/MA (Figure 3.10a) and $Cu_{0.6}$@Zr/MA (Figure 3.10b) catalysts exhibited a broad absorption in the range of 1000 to 1700 $cm^{-1}$ after the introduction of reaction gas ($CO_2$ and $H_2$), corresponding to surface carboxylate (1685 $cm^{-1}$ and 1220 $cm^{-1}$) and carbonate species (1440 $cm^{-1}$ and 1294 $cm^{-1}$).[41-43] With the increase of reaction temperature from 30 to 300 $^oC$, the spectra showed several new absorption peaks related to possible intermediates,

including formate species (2846 $cm^{-1}$, 1623 $cm^{-1}$,1327$cm^{-1}$) and carbonyl species (2050 – 2200 $cm^{-1}$).[44-46] On $Cu_{0.6}$/MA, the intensity of carbonates and carboxylates was decreased as the temperature increased, and the formate species appeared at 100 °C and continued to increase until 200 °C, suggesting the conversion of absorbed $CO_2$ to formate species. As further elevating the temperature, the intensity of the formate peak started to decrease, and meanwhile the peak related to CO was observed in the range of 2050 – 2200 $cm^{-1}$, demonstrating the reaction pathway of the dissociation of formate to generate CO.[47] When comparing the DRIFTS spectra of $Cu_{0.6}$/MA and $Cu_{0.6}$@Zr/MA, it could be noted that the introduction of $ZrO_2$ did not change the reaction pathway of RWGS reaction. Furthermore, the intensity of formate peaks on $Cu_{0.6}$@Zr/MA at 250 and 300 °C was much lower than that on $Cu_{0.6}$/MA, while the intensity of CO peak seemed similar, suggesting that the decomposition of formate was facilitated on $Cu_{0.6}$@Zr/MA catalyst, possibly via modulating the Cu nanoparticles based on the above investigation, therefore enhancing the activity of CO production.

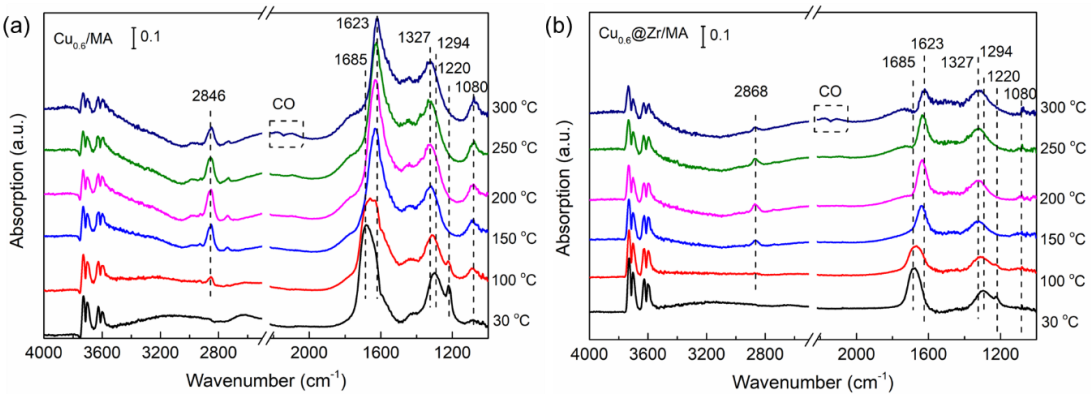


**Figure 3.10** In situ DRIFTS spectra collected over (a) $Cu_{0.6}$/MA and (b) $Cu_{0.6}$@Zr/MA catalysts during photo-assisted RWGS reaction under different temperatures.

### 3.3.3 Light-assisted catalytic activity

In the process of photothermal catalytic $CO_2$ reduction, except solar-to-heating effect, photo-induced hot carriers might also participate in the reaction via activating the absorbed reactants and intermediates. In order to elucidate the mechanism of light irradiation in this chapter, I conducted the photo-assisted thermocatalytic $CO_2$

conversion with $H_2$ on $Cu_{0.6}$/MA and $Cu_{0.6}$@Zr/MA catalysts in a stainless-steel reaction system equipped with a temperature controller and an external electrical heater to excluded the light-heating effect during the reaction. L42 and HA30 filters were applied to eliminate ultraviolet and infrared light, and the intensity of visible light (400 nm < λ < 800 nm) was measured to be 644.2 mW $cm^{-2}$. As shown in Figure 3.11a, in the dark condition, with the temperature was elevated from 200 °C to 300 °C, the CO production of $Cu_{0.6}$@Zr/MA was increased from 1.5 mmol·$g^{-1}$·$h^{-1}$ to 77.9 mmol·$g^{-1}$·$h^{-1}$, higher than that of $Cu_{0.6}$/MA at same temperatures. After the introduction of light irradiation, the production rate of CO on both catalysts was enhanced. Specially, the CO yield over $Cu_{0.6}$@Zr/MA was increased to 3.1 mmol·$g^{-1}$·$h^{-1}$ at 200 °C under visible light, 2.1 times higher than the production in dark condition. As the reaction temperature was elevated to 300 °C, the CO production reached 94.7 mmol·$g^{-1}$·$h^{-1}$, still higher than the production without light. These results revealed the obvious promoting effect of visible light on the RWGS reaction, which could be attributed to photo-induced hot carriers in Cu NPs.

To investigate the RWGS reaction kinetics under dark and light conditions, the apparent activation energy ($E_a$) was calculated based on the Arrhenius equation ($\ln r = -E_a/RT + \ln A$) in the temperature range from 200 °C to 300 °C (Figure 3.11b). The apparent activation energy for $Cu_{0.6}$/MA in dark was 107.7 kJ·$mol^{-1}$, and was reduced to 85.9 kJ·$mol^{-1}$ with the introduction of light, indicating that light could promote the reaction process, possibly due to the enhanced activation of reactants and conversion of intermediates by photo-induced hot carriers in Cu NPs. In addition, the $ZrO_2$ in $Cu_{0.6}$@Zr/MA decreased the $E_a$ to 84.0 kJ·$mol^{-1}$ and 66.6 kJ·$mol^{-1}$ in dark and light conditions respectively, suggesting the reaction activity could be promoted by the modulation by $ZrO_2$.

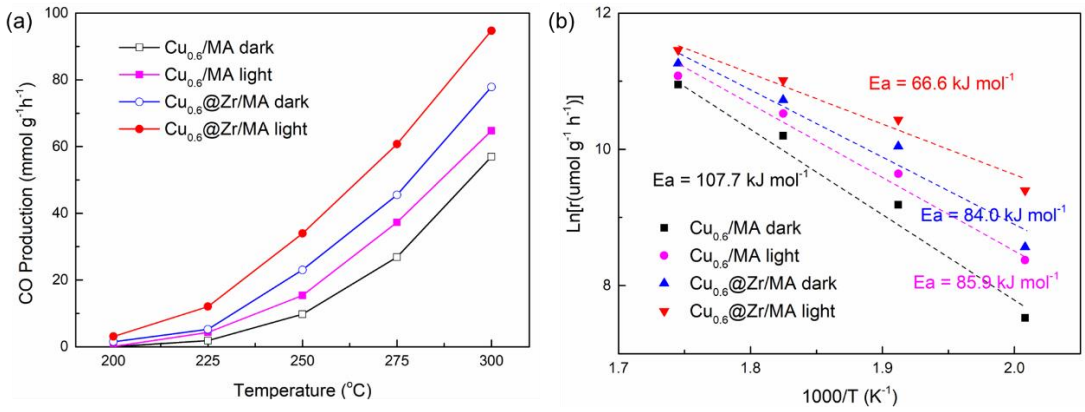


**Figure 3.11** Photo-assisted thermocatalytic RWGS reaction. (a) CO production over $Cu_{0.6}$/MA and $Cu_{0.6}$@Zr/MA catalysts at different temperatures under dark (electrical heating) and light (photo-assisted electrical heating) conditions, (b) Arrhenius plots for RWGS reaction under different reaction conditions.

In order to further investigate the effect of light irradiation on RWGS reaction process, the time-resolved DRIFTS spectra were recorded on $Cu_{0.6}$@Zr/MA in dark and light conditions with the temperature controlled at 250 °C. As displayed in Figure 3.12, almost no apparent changes in spectra were observed in dark condition during the recording time. In comparison, upon light irradiation, the peak centered at 2846 $cm^{-1}$ assigned to absorbed formate species was decreased and the two peaks at 2170 and 2100 $cm^{-1}$ belonging to CO were increased, indicating that the reaction pathway of the decomposition of formate intermediates to form CO as the final product, which could be accelerated by the light-induced hot carriers in Cu NPs.

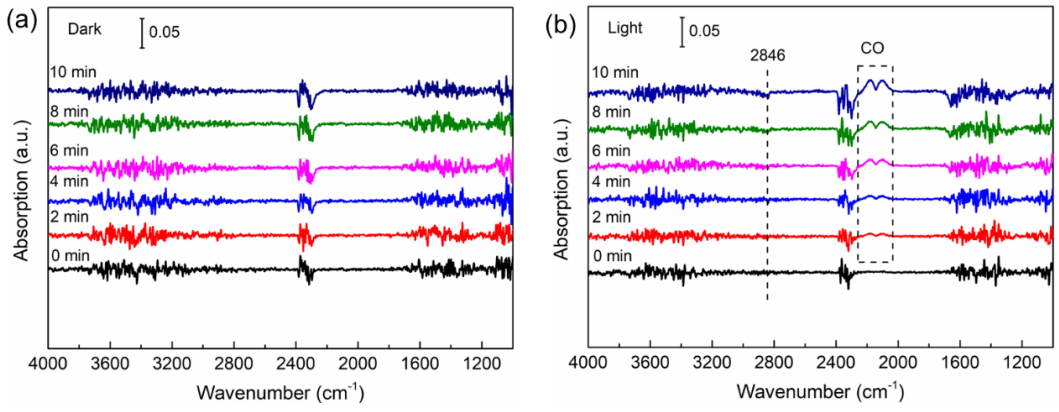


**Figure 3.12** In situ DRIFTS spectra recorded on $Cu_{0.6}$@Zr/MA catalyst under (a) dark and (b) light conditions with reaction temperature at 250 °C.

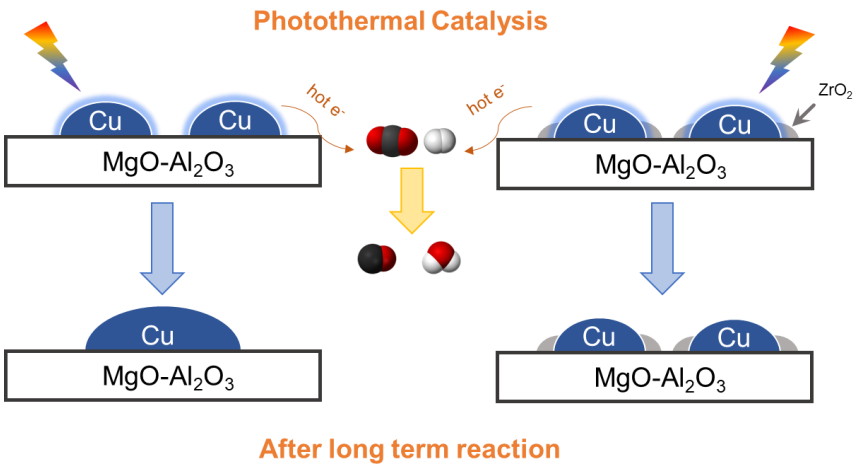


**Figure 3.13** Schematic illustration of the reaction mechanism for photothermal catalytic $CO_2$ hydrogenation over $Cu_{0.6}$/MA and $Cu_{0.6}$@Zr/MA.

## 3.4 Conclusion

In conclusion, this study demonstrates the irreducible oxide ($ZrO_2$)-modified Cu-based photothermal catalysts which are not only highly active but also extremely stable for $CO_2$ reduction to CO (Figure 3.13). The optimized catalyst $Cu_{0.6}$@Zr/MA shows an excellent CO production of 125.7 $mmol \cdot g^{-1} \cdot h^{-1}$ under light irradiation of 1.88 $W \cdot cm^{-2}$ and the conversion efficiency of solar energy reaches 0.97%. After 8 h reaction, the activity is almost stable, and still remains 93% after 12 h continuous reaction process. The detailed study illustrates that the modification of $ZrO_2$ can stabilize the nanostructures of Cu nanoparticles and alleviate the aggregation of Cu at rough conditions, such as high temperature and wet atmosphere, thereby improving the stability of catalyst. This chapter provides a universal strategy to design and fabricate highly efficient and long-time stable photothermal catalysts for $CO_2$ reduction.

## References

[1] E.C. Ra, K.Y. Kim, E.H. Kim, H. Lee, K. An, J.S. Lee, Recycling Carbon Dioxide through Catalytic Hydrogenation: Recent Key Developments and Perspectives, ACS Catalysis, 10 (2020) 11318-11345.

[2] D. Mateo, J.L. Cerrillo, S. Durini, J. Gascon, Fundamentals and applications of photo-thermal catalysis, Chem. Soc. Rev., 50 (2021) 2173-2210.

[3] S. Luo, X. Ren, H. Lin, H. Song, J. Ye, Plasmonic photothermal catalysis for solar-to-fuel conversion: current status and prospects, Chem Sci, 12 (2021) 5701-5719.

[4] X. Meng, L. Liu, S. Ouyang, H. Xu, D. Wang, N. Zhao, J. Ye, Nanometals for Solar-to-Chemical Energy Conversion: From Semiconductor-Based Photocatalysis to Plasmon-Mediated Photocatalysis and Photo-Thermocatalysis, Adv. Mater., 28 (2016) 6781-6803.

[5] J. Jia, H. Wang, Z. Lu, P.G. O'Brien, M. Ghoussoub, P. Duchesne, Z. Zheng, P. Li, Q. Qiao, L. Wang, A. Gu, A.A. Jelle, Y. Dong, Q. Wang, K.K. Ghuman, T. Wood, C. Qian, Y. Shao, C. Qiu, M. Ye, Y. Zhu, Z.H. Lu, P. Zhang, A.S. Helmy, C.V. Singh, N.P. Kherani, D.D. Perovic, G.A. Ozin, Photothermal Catalyst Engineering: Hydrogenation of Gaseous $CO_2$ with High Activity and Tailored Selectivity, Adv Sci (Weinh), 4 (2017) 1700252.

[6] R.P. Ye, J. Ding, W. Gong, M.D. Argyle, Q. Zhong, Y. Wang, C.K. Russell, Z. Xu, A.G. Russell, Q. Li, M. Fan, Y.G. Yao, $CO_2$ hydrogenation to high-value products via heterogeneous catalysis, Nat Commun, 10 (2019) 5698.

[7] L. Wan, Q. Zhou, X. Wang, T.E. Wood, L. Wang, P.N. Duchesne, J. Guo, X. Yan, M. Xia, Y.F. Li, A.A. Jelle, U. Ulmer, J. Jia, T. Li, W. Sun, G.A. Ozin, $Cu_2O$ nanocubes with mixed oxidation-state facets for (photo)catalytic hydrogenation of carbon dioxide, Nature Catalysis, 2 (2019) 889-898.

[8] N. Podrojková, V. Sans, A. Oriňak, R. Oriňaková, Recent Developments in the Modelling of Heterogeneous Catalysts for $CO_2$ Conversion to Chemicals, ChemCatChem, 12 (2020) 1802-1825.

[9] C. Kim, S. Hyeon, J. Lee, W.D. Kim, D.C. Lee, J. Kim, H. Lee, Energy-efficient $CO_2$ hydrogenation with fast response using photoexcitation of $CO_2$ adsorbed on metal catalysts, Nature Communications, 9 (2018) 3027.

[10] K.K. Ghuman, T.E. Wood, L.B. Hoch, C.A. Mims, G.A. Ozin, C.V. Singh, Illuminating $CO_2$ reduction on frustrated Lewis pair surfaces: investigating the role of surface hydroxides and oxygen vacancies on nanocrystalline $In_2O_{3-x}(OH)_y$, PCCP, 17 (2015) 14623-14635.

[11] L. He, T.E. Wood, B. Wu, Y. Dong, L.B. Hoch, L.M. Reyes, D. Wang, C. Kübel, C. Qian, J. Jia, K. Liao, P.G. O'Brien, A. Sandhel, J.Y.Y. Loh, P. Szymanski, N.P. Kherani, T.C. Sum,

C.A. Mims, G.A. Ozin, Spatial Separation of Charge Carriers in $In_2O_{3-x}(OH)_y$ Nanocrystal Superstructures for Enhanced Gas-Phase Photocatalytic Activity, ACS Nano, 10 (2016) 5578-5586.

[12] H. Robatjazi, H. Zhao, D.F. Swearer, N.J. Hogan, L. Zhou, A. Alabastri, M.J. McClain, P. Nordlander, N.J. Halas, Plasmon-induced selective carbon dioxide conversion on earth-abundant aluminum-cuprous oxide antenna-reactor nanoparticles, Nature Communications, 8 (2017) 27.

[13] J. Guo, P.N. Duchesne, L. Wang, R. Song, M. Xia, U. Ulmer, W. Sun, Y. Dong, J.Y.Y. Loh, N.P. Kherani, J. Du, B. Zhu, W. Huang, S. Zhang, G.A. Ozin, High-Performance, Scalable, and Low-Cost Copper Hydroxyapatite for Photothermal $CO_2$ Reduction, ACS Catalysis, 10 (2020) 13668-13681.

[14] L. Wang, Y. Dong, T. Yan, Z. Hu, A.A. Jelle, D.M. Meira, P.N. Duchesne, J.Y.Y. Loh, C. Qiu, E.E. Storey, Y. Xu, W. Sun, M. Ghoussoub, N.P. Kherani, A.S. Helmy, G.A. Ozin, Black indium oxide a photothermal $CO_2$ hydrogenation catalyst, Nat Commun, 11 (2020) 2432.

[15] Y.F. Li, W. Lu, K. Chen, P. Duchesne, A. Jelle, M. Xia, T.E. Wood, U. Ulmer, G.A. Ozin, Cu Atoms on Nanowire $Pd/H_yWO_{3-x}$ Bronzes Enhance the Solar Reverse Water Gas Shift Reaction, J. Am. Chem. Soc., 141 (2019) 14991-14996.

[16] Z.-j. Wang, H. Song, H. Pang, Y. Ning, T.D. Dao, Z. Wang, H. Chen, Y. Weng, Q. Fu, T. Nagao, Y. Fang, J. Ye, Photo-assisted methanol synthesis via $CO_2$ reduction under ambient pressure over plasmonic Cu/ZnO catalysts, Applied Catalysis B: Environmental, 250 (2019) 10-16.

[17] B. Deng, H. Song, K. Peng, Q. Li, J. Ye, Metal-organic framework-derived Ga-$Cu/CeO_2$ catalyst for highly efficient photothermal catalytic $CO_2$ reduction, Applied Catalysis B: Environmental, 298 (2021) 120519.

[18] D. Vovchok, C. Zhang, S. Hwang, L. Jiao, F. Zhang, Z. Liu, S.D. Senanayake, J.A. Rodriguez, Deciphering Dynamic Structural and Mechanistic Complexity in $Cu/CeO_2$/ZSM-5 Catalysts for the Reverse Water-Gas Shift Reaction, ACS Catalysis, 10 (2020) 10216-10228.

[19] J. Yang, M. Peng, G. Ren, H. Qi, X. Zhou, J. Xu, F. Deng, Z. Chen, J. Zhang, K. Liu, X. Pan, W. Liu, Y. Su, W. Li, B. Qiao, D. Ma, T. Zhang, A Hydrothermally Stable Irreducible

Oxide-Modified Pd/$MgAl_2O_4$ Catalyst for Methane Combustion, Angew. Chem. Int. Ed. Engl., 59 (2020) 18522-18526.

[20] B. An, J. Zhang, K. Cheng, P. Ji, C. Wang, W. Lin, Confinement of Ultrasmall Cu/ZnOx Nanoparticles in Metal-Organic Frameworks for Selective Methanol Synthesis from Catalytic Hydrogenation of $CO_2$, J. Am. Chem. Soc., 139 (2017) 3834-3840.

[21] H. Zhang, T. Wang, J. Wang, H. Liu, T.D. Dao, M. Li, G. Liu, X. Meng, K. Chang, L. Shi, T. Nagao, J. Ye, Surface-Plasmon-Enhanced Photodriven $CO_2$ Reduction Catalyzed by Metal–Organic-Framework-Derived Iron Nanoparticles Encapsulated by Ultrathin Carbon Layers, Adv. Mater., 28 (2016) 3703-3710.

[22] Y. Zhao, X. Jia, G.I.N. Waterhouse, L.-Z. Wu, C.-H. Tung, D. O'Hare, T. Zhang, Layered Double Hydroxide Nanostructured Photocatalysts for Renewable Energy Production, Advanced Energy Materials, 6 (2016) 1501974.

[23] G. Chen, R. Gao, Y. Zhao, Z. Li, G.I.N. Waterhouse, R. Shi, J. Zhao, M. Zhang, L. Shang, G. Sheng, X. Zhang, X. Wen, L.-Z. Wu, C.-H. Tung, T. Zhang, Alumina-Supported CoFe Alloy Catalysts Derived from Layered-Double-Hydroxide Nanosheets for Efficient Photothermal $CO_2$ Hydrogenation to Hydrocarbons, Adv. Mater., 30 (2018) 1704663.

[24] L. Deng, Z. Wang, X. Jiang, J. Xu, Z. Zhou, X. Li, Z. You, M. Ding, T. Shishido, X. Liu, M. Xu, Catalytic aqueous $CO_2$ reduction to formaldehyde at Ru surface on hydroxyl-groups-rich LDH under mild conditions, Applied Catalysis B: Environmental, 322 (2023) 122124.

[25] Z. Yuan, L. Wang, J. Wang, S. Xia, P. Chen, Z. Hou, X. Zheng, Hydrogenolysis of glycerol over homogenously dispersed copper on solid base catalysts, Applied Catalysis B: Environmental, 101 (2011) 431-440.

[26] S. Song, H. Song, L. Li, S. Wang, W. Chu, K. Peng, X. Meng, Q. Wang, B. Deng, Q. Liu, A selective Au-ZnO/$TiO_2$ hybrid photocatalyst for oxidative coupling of methane to ethane with dioxygen, Nature Catalysis, 4 (2021) 1032-1042.

[27] X. Zhang, G. Cui, H. Feng, L. Chen, H. Wang, B. Wang, X. Zhang, L. Zheng, S. Hong, M. Wei, Platinum–copper single atom alloy catalysts with high performance towards glycerol hydrogenolysis, Nature communications, 10 (2019) 1-12.

[28] L. Zhou, D.F. Swearer, C. Zhang, H. Robatjazi, H. Zhao, L. Henderson, L. Dong, P. Christopher, E.A. Carter, P. Nordlander, N.J. Halas, Quantifying hot carrier and thermal contributions in plasmonic photocatalysis, Science, 362 (2018) 69.

[29] Y. Yu, R. Jin, J. Easa, W. Lu, M. Yang, X. Liu, Y. Xing, Z. Shi, Highly active and stable copper catalysts derived from copper silicate double-shell nanofibers with strong metal–support interactions for the RWGS reaction, Chem. Commun., 55 (2019) 4178-4181.

[30] Y.F. Xu, P.N. Duchesne, L. Wang, A. Tavasoli, A.A. Jelle, M. Xia, J.F. Liao, D.B. Kuang, G.A. Ozin, High-performance light-driven heterogeneous $CO_2$ catalysis with near-unity selectivity on metal phosphides, Nat Commun, 11 (2020) 5149.

[31] M. Zhu, P. Tian, M.E. Ford, J. Chen, J. Xu, Y.-F. Han, I.E. Wachs, Nature of Reactive Oxygen Intermediates on Copper-Promoted Iron–Chromium Oxide Catalysts during $CO_2$ Activation, ACS Catalysis, 10 (2020) 7857-7863.

[32] P. Lackner, Z. Zou, S. Mayr, U. Diebold, M. Schmid, Using photoelectron spectroscopy to observe oxygen spillover to zirconia, PCCP, 21 (2019) 17613-17620.

[33] M. Manzoli, R.D. Monte, F. Boccuzzi, S. Coluccia, J. Kašpar, CO oxidation over $CuO_x$-$CeO_2$-$ZrO_2$ catalysts: Transient behaviour and role of copper clusters in contact with ceria, Applied Catalysis B: Environmental, 61 (2005) 192-205.

[34] J. Shan, G. Giannakakis, J. Liu, S. Cao, M. Ouyang, M. Li, S. Lee, M. Flytzani-Stephanopoulos, PdCu Single Atom Alloys for the Selective Oxidation of Methanol to Methyl Formate at Low Temperatures, Top. Catal., 63 (2020) 618-627.

[35] M. Ouyang, K.G. Papanikolaou, A. Boubnov, A.S. Hoffman, G. Giannakakis, S.R. Bare, M. Stamatakis, M. Flytzani-Stephanopoulos, E.C.H. Sykes, Directing reaction pathways via in situ control of active site geometries in PdAu single-atom alloy catalysts, Nat Commun, 12 (2021) 1549.

[36] N.D. Subramanian, C.S.S.R. Kumar, K. Watanabe, P. Fischer, R. Tanaka, J.J. Spivey, A DRIFTS study of CO adsorption and hydrogenation on Cu-based core–shell nanoparticles, Catalysis Science & Technology, 2 (2012) 621.

[37] L. Liu, F. Gao, H. Zhao, Y. Li, Tailoring Cu valence and oxygen vacancy in $Cu/TiO_2$ catalysts for enhanced $CO_2$ photoreduction efficiency, Applied Catalysis B: Environmental, 134-135 (2013) 349-358.

[38] Z. Qu, Y. Li, S. Huang, P. Chen, X. Ma, Clarification of copper species over Cu-SAPO-34 catalyst by DRIFTS and DFT study of CO adsorption, Science China Chemistry, 60 (2017) 912-919.

[39] C. Chen, H. Ren, Y. He, Y. Zhan, C. Au, Y. Luo, X. Lin, S. Liang, L. Jiang, Unraveling the Role of $Cu^0$ and $Cu^+$ Sites in $Cu/SiO_2$ Catalysts for Water-Gas Shift Reaction, ChemCatChem, 12 (2020) 4672-4679.

[40] J. Schumann, J. Kröhnert, E. Frei, R. Schlögl, A. Trunschke, IR-Spectroscopic Study on the Interface of Cu-Based Methanol Synthesis Catalysts: Evidence for the Formation of a ZnO Overlayer, Top. Catal., 60 (2017) 1735-1743.

[41] S. Kattel, P. Liu, J.G. Chen, Tuning Selectivity of $CO_2$ Hydrogenation Reactions at the Metal/Oxide Interface, J. Am. Chem. Soc., 139 (2017) 9739-9754.

[42] S. Collins, M. Baltanas, A. Bonivardi, An infrared study of the intermediates of methanol synthesis from carbon dioxide over Pd/β-GaO, J. Catal., 226 (2004) 410-421.

[43] G. Finos, S. Collins, G. Blanco, E. del Rio, J.M. Cíes, S. Bernal, A. Bonivardi, Infrared spectroscopic study of carbon dioxide adsorption on the surface of cerium–gallium mixed oxides, Catal. Today, 180 (2012) 9-18.

[44] L. Lin, S. Yao, Z. Liu, F. Zhang, N. Li, D. Vovchok, A. Martínez-Arias, R. Castañeda, J. Lin, S.D. Senanayake, D. Su, D. Ma, J.A. Rodriguez, In Situ Characterization of $Cu/CeO_2$ Nanocatalysts for $CO_2$ Hydrogenation: Morphological Effects of Nanostructured Ceria on the Catalytic Activity, The Journal of Physical Chemistry C, 122 (2018) 12934-12943.

[45] S.-C. Yang, S.H. Pang, T.P. Sulmonetti, W.-N. Su, J.-F. Lee, B.-J. Hwang, C.W. Jones, Synergy between Ceria Oxygen Vacancies and Cu Nanoparticles Facilitates the Catalytic Conversion of $CO_2$ to CO under Mild Conditions, ACS Catalysis, 8 (2018) 12056-12066.

[46] N.C. Nelson, M.-T. Nguyen, V.-A. Glezakou, R. Rousseau, J. Szanyi, Carboxyl intermediate formation via an in situ-generated metastable active site during water-gas shift catalysis, Nature Catalysis, 2 (2019) 916-924.

[47] T.H. Tan, B. Xie, Y.H. Ng, S.F.B. Abdullah, H.Y.M. Tang, N. Bedford, R.A. Taylor, K.-F. Aguey-Zinsou, R. Amal, J. Scott, Unlocking the potential of the formate pathway in the photo-assisted Sabatier reaction, Nature Catalysis, 3 (2020) 1034-1043.

# Chapter 4 Photothermal catalytic $CO_2$ hydrogenation to methanol over $Ru/In_2O_3$ catalysts under atmospheric pressure

## 4.1 Introduction

The development of modern society has accelerated the consumption of non-renewable fossil fuel energy, resulting in multiple energy crises and environmental problems.[1, 2] Methanol ($CH_3OH$) is an essential chemical industrial feedstock and also considered as a promising candidate for clean and renewable energy carrier due to its high volume-specific energy density.[3] George A. Olah has drawn a future prospect about "methanol economy", in which methanol acts as the medium for energy consumption and chemical industry in the near future.[4] Nowadays, fossil fuels conversion domains the process of industrial methanol production, resulting in massive energy consumption and immense $CO_2$ emission. Methanol production from $CO_2$ hydrogenation is regarded as a sustainable and environmental-friendly route and has attracted worldwide interest.[5-7]

Over the past several decades, many efforts have been taken to realize effective thermocatalytic $CO_2$ hydrogenation to methanol, mostly using Cu-based nanocomposites as catalysts.[8-12] However, due to the exothermic characteristics of methanol synthesis (eqn (1)) and the competing CO production via side reverse water-gas shift reaction (RWGS, eqn (2)), this process demands relatively harsh reaction conditions, especially an ultrahigh pressure (temperature of 200 ~300 $^oC$ and pressure of 3 ~ 10 Mpa), to simultaneously achieve high methanol selectivity and production rate, which results in excess energy input, thereby hindering the large-scale industrial application.[13, 14]

$$CO_2 + 3H_2 \Leftrightarrow CH_3OH + H_2O, \qquad \Delta H°_{298K} = -49.5 \text{ kJ mol}^{-1} \quad (1)$$

$$CO_2 + H_2 \Leftrightarrow CO + H_2O, \qquad \Delta H°_{298K} = +41.2 \text{ kJ mol}^{-1} \quad (2)$$

Recently, photothermal catalysis based on plasmonic nanometals composites has attracted great interest due to its promising prospect in the field of fuel production and fine chemical conversion, together with the utilization of clean and regenerable solar energy, which is regarded as an ideal energy source for future human society.[15-20] The light-induced hot carriers are capable to activate chemical bonds and trigger reaction processes, such as the dissociation of $H_2$ and the activation of C=O bond.[20-24] Therefore, it is expected to be a promising technology to catalyze $CO_2$ hydrogenation to methanol via photothermal process, also known as "solar methanol production", which could convert solar energy into valuable chemical energy as fuel and industrial feedstock without extra greenhouse gas generation.[25, 26] However, quite few studies have been reported on photothermal methanol production under mild conditions, especially at ambient pressure.[27-30] Among these studies, both activity and selectivity are still relatively low, inhibiting the further application of photothermal methanol production from $CO_2$ hydrogenation, and the detailed mechanism still requires thorough investigation and discussion.

$In_2O_3$ has been demonstrated to be an excellent catalyst for $CO_2$ hydrogenation to $CH_3OH$ according to recent reported works, including thermal catalysis, photocatalysis and photothermal catalysis.[28, 30-32] The oxygen vacancies ($V_o$) in $In_2O_3$ play a key role in modulating the catalytic activity of methanol production in $CO_2$ hydrogenation.[30, 33-35] Furthermore, transition metals including noble metals (Pd, Pt, Rh, Au) and non-noble metals (Ni, Co) have been utilized to modify the surface chemical architectures of $In_2O_3$ and provide active sites for $CO_2$ and $H_2$ activation, thereby contributing to enhanced catalytic performance.[31, 36-39] However, most related researches are focused on the thermal catalytic process under high pressure (usually 1.0 MPa ~ 5.0 MPa), thus rendering such composites potential candidates for solar methanol production under mild conditions.

Herein, Ru-loaded $In_2O_3$ nanorods were synthesized for photothermal methanol production from $CO_2$ hydrogenation under atmospheric pressure. Upon light irradiation, a maximum methanol production of 280.4 μmol $g^{-1}$ $h^{-1}$ was obtained over 2 wt%

$Ru/In_2O_3$, which was around 50 times higher than that of pure $In_2O_3$. Mechanism investigation demonstrated that the outstanding catalytic activity was assigned to the interfacial interaction between Ru and $In_2O_3$, the improved concentration of oxygen vacancies by loading Ru, as well as the photo-thermal synergistic effect on $CO_2$ hydrogenation. Detailed studies and DFT calculations suggested that methanol was mainly produced via the CO-hydrogenation route, in which Ru nanoparticles facilitated the activation and conversion of $H_2$ and $CO_2$ assisted by light-induced hot carriers, and afterwards the oxygen vacancies on $In_2O_3$ favored the hydrogenation process from absorbed intermediates $^*CO$ to final product methanol.

## 4.2 Experimental section

### 4.2.1 Materials

All chemicals were utilized without any treatment. Indium (III) chloride ($InCl_3$), rhodium (III) chloride ($RhCl_3$), ruthenium (III) chloride ($RuCl_3$), hexachloroplatinic acid ($H_2PtCl_6$), palladium (II) chloride ($PdCl_2$), copper (II) nitrate trihydrate ($Cu(NO_3)_2 \cdot 3H_2O$), aluminum(III) nitrate nonahydrate ($Al(NO_3)_3 \cdot 9H_2O$), zinc(II) nitrate hexahydrate ($Zn(NO_3)_2 \cdot 6H_2O$), sodium carbonate ($Na_2CO_3$), urea, Sodium borohydride ($NaBH_4$), commercial $In_2O_3$ were purchased from Wako Chemical Co., Ltd. Distilled water (18.2 MΩ cm) was utilized in this work.

### 4.2.2 Catalyst preparation

***Synthesis of $In_2O_3$.*** $In_2O_3$ was synthesized based on a reported hydrothermal method.[40] Typically, 0.29 g $InCl_3$ and 1.2 g urea were dissolved with 80 ml of deionized water. After vigorous magnetic stirring at room temperature for 1 h, the above solution was subsequently transferred into a 100 mL Teflon-lined stainless-steel autoclave and heated at 140 $^oC$ for 12 h. After the reaction finished, the autoclave was cooled to room temperature. The white precipitates were collected by centrifugation and washed with distilled water for several times, then dried at 70 $^oC$ in a vacuum oven

overnight. Afterwards, the white precursors were annealed at 250 $^{o}$C for 4 h in air with a ramping rate of 5 $^{o}$C min$^{-1}$ to obtain $In_2O_3$ powder.

***Synthesis of nanometals/$In_2O_3$.*** Metal nanoparticles (Ru, Rh, Pt, Pd, Cu) were loaded on synthesized $In_2O_3$ using $NaBH_4$ as a reducing agent. Typically, for 2 wt.% Ru/$In_2O_3$, 200 mg $In_2O_3$ and 8.2 mg $RuCl_3$ were dissolved into 100 mL deionized water under vigorous stirring. After stirring for 1 h, fresh $NaBH_4$ aqueous solution (10 mL, 100 mM) was added into the above mixture drop by drop. Afterwards, the sample was filtered and washed with water for 6 times, and then dried overnight at 70 $^{o}$C. For different loading amount (0.5 wt.%, 1.0 wt.%, 5.0 wt.%), the amount of $RuCl_3$ was changed to 2.1, 4.1 and 20.5 mg respectively. Rh/$In_2O_3$, Pt/$In_2O_3$, Pd/$In_2O_3$ and Cu/$In_2O_3$ were produced through the same procedure except using corresponding metal precursors ($RhCl_3$, $H_2PtCl_6$, $H_2PdCl_6$, $Cu(NO_3)_2{\cdot}6H_2O$).

***Synthesis of reference catalysts.*** CuZnAl was synthesized using the same method as described in chapter 2. Reference catalyst (2Ru/com-$In_2O_3$) was synthesized by the same method above except for the commercial $In_2O_3$ instead of synthesized $In_2O_3$. Another reference catalyst (2Ru/$In_2O_3$-wet) was synthesized by the wet-impregnation method. A certain amount of $RuCl_3$ solution was impregnated on synthesized $In_2O_3$ followed by calcination in air at 250 $^{o}$C for 2h.

### 4.2.3 Characterization

A PANalytical B.V. XRD diffractometer with Cu Kα radiation (λ = 1.5406 Å) was utilized to obtain the powder X-ray diffraction (XRD) results. The contents of Ru and In in samples were analyzed via inductively coupled plasma-optical emission spectrometry (ICP-OES, Agilent 720-ES). A JEOL JEM-F200 (HR) transmission electron microscopy operated at 200 kV was utilized to collect the transmission electron micrography (TEM) and high-resolution TEM (HRTEM) images of catalysts. The elemental distribution of samples was recorded through energy-dispersive X-ray spectroscopy (EDS) test on the above TEM equipment. The AutoChem II 2920 chemisorption equipment was used to carry out $H_2$-TPR test. The Thermo Fisher

ESCALAB Xi+ system was utilized to collect X-ray photoelectron spectroscopy (XPS) of samples. A Shimadzu UV-2500 spectrometer with an integrating sphere accessory was used to obtain the UV-Visible diffuse reflectance spectroscopy (UV-Vis DRS). Raman spectroscopy was collected on the Raman microscope (NRS-1000, Japan) equipped with a green laser (532 nm) as the excitation source. Indium K-edge X-ray absorption near edge structure (XANES) spectra were measured at the Photon Factory Advanced Ring in Tsukuba, Japan.

### 4.2.4 Catalytic activity evaluation

Solar-driven photothermal catalytic $CO_2$ hydrogenation experiment was carried out in a homemade quartz reactor, which has been described in chapter 2. 300 W Xenon arc lamp equipped with an L42 filter was utilized as the illuminant and the only energy input. A Thorlabs PM-100D optical power meter with an S401C sensor was utilized to measure the intensity of. During the experiment, 10 mg catalyst was smoothly dispersed onto an air-permeable quartz fiber filter in the reactor. A thermocouple located at the center of sample surface was utilized to monitor the temperature of catalyst. The mixed reaction gas ($CO_2/H_2$ = 1:3) flowed through the system with a rate of 20 mL $min^{-1}$. After purging for 0.5 h, the light was switched on to initial the solar-driven experiment. The venting gas was injected into a gas chromatography (Shimadzu GC2014) to analyze the components. The CG was equipped with two capillary columns (porapak-Q and shincarbon-A) and a flame ionization (FID) detector.

Photo-assisted thermocatalytic $CO_2$ hydrogenation reaction was carried out in a flow-type stainless-steel reaction system with external electric heating, which has also been described in chapter 2. The catalyst temperature was controlled by a temperature controller (TC-1000 JASCO) and a thermocouple. The visible light source was an LA-251 Xe lamp with L42 and HA30 filters. Specifically, 10 mg sample was uniformly dispersed onto the sample holder. Then a gas mixture ($CO_2/H_2$ = 1/3) flowed through the reaction system with a rate of 20 mL $min^{-1}$. After purging for 30 min, the electrical heater was turned on to elevate the reactor temperature in a ramping rate of 5 $^oC$ $min^{-1}$. The analysis of products was the same as the above experiment.

### 4.2.5 In situ DRIFTS analysis

A JASCO FT-IR 6300 Spectrometers equipped with a liquid nitrogen-cooled mercury-cadmium-telluride (MCT) detector and an in situ diffuse reflectance cell was utilized to conduct in situ diffuse reflectance infrared Fourier transform spectroscopy (DRIFTS) test. DRTFTS spectra were recorded at 4 $cm^{-1}$ resolution with 32 scans. Before the analyses, 10 mg catalyst was purged by Ar flow for 30 min at room temperature. Then the temperature was elevated with a ramping rate of 10 $^{o}C$ $min^{-1}$ and maintained at 200 $^{o}C$. After the background spectrum was obtained in Ar atmosphere, the gas flow was changed into the mixture of $CO_2/H_2$ (5/15 mL $min^{-1}$) and then in situ DRIFTS experiment was performed under irradiation.

### 4.2.6 Density functional theory calculations

All density functional theory (DFT) calculations were conducted on the QUANTUM ESPRESSO package. The exchange and correlation energy were described by the Perdew-Burke-Emzerhof (PBE) and the generalized gradient approximation (GGA) functional. The cutoff energy of plane-wave basis was set as 65 Ry and the Monkhorst-Pack k-point was set as 3 × 3 × 1. Energy and gradient convergences with $10^{-6}$ Ry and 0.001 Ry / Å were adopted in the calculations.

The $In_2O_3$ (111) surface was modeled with a (2 × 2) supercell from the bulk $In_2O_3$, according to XRD result. The surface slab contained 48 In atoms and 72 O atoms. In order to exclude any interaction between layers, the vacuum height was set as 12 Å. The defective surface ($In_2O_3$-$O_v$) was obtained by removing one oxygen atom from the surface. The $Ru_4/In_2O_3$-$O_v$ model was established by loading a tetrahedral $Ru_4$ cluster on the defective surface $In_2O_3$-$O_v$. After optimizing the model, the atoms in the bottom layer were fixed, and the rest of atoms were allowed to relax during the calculations of the reaction mechanism investigation. The relative energy of each reaction state was defined as the energy difference between the corresponding and initial states.

**Table 4.1** Performance of thermal catalytic $CO_2$ hydrogenation of $In_2O_3$ loaded with different metal catalysts at 250 °C. Metal loading: 2 wt%. Reaction conditions: 250 °C, 1 bar, $CO_2/H_2$ = 5/15 mL $min^{-1}$

| Catalyst | CO yield (μmol $g^{-1}$ $h^{-1}$) | $CH_3OH$ yield (μmol $g^{-1}$ $h^{-1}$) | $CH_3OH$ selectivity (%) |
|---|---|---|---|
| $In_2O_3$ | 156.2 | 29.5 | 21.3 |
| $Ru/In_2O_3$ | 337.2 | 122.8 | 35.2 |
| $Cu/In_2O_3$ | 275.0 | 26.1 | 11.1 |
| $Rh/In_2O_3$ | 2581.0 | 147.8 | 9.0 |
| $Pt/In_2O_3$ | 595.4 | 68.3 | 12.8 |
| $Pd/In_2O_3$ | 1059.1 | 120.1 | 11.2 |

## 4.3 Results and discussion

### 4.3.1 Preliminary screening of metal catalysts

$In(OH)_3$ nanorods were first synthesized by a hydrothermal method and then annealed at 250 °C for 4 h in air to obtain $In_2O_3$ nanorods[40]. After that, a variety of metals (Cu, Ru, Rh, Pd, Pt) were loaded on $In_2O_3$ nanorods via a $NaBH_4$-reducing method with the loading amount of metal designed at 2 wt%. According to X-ray diffraction (XRD) patterns (Figure 4.1), all diffraction peaks in these catalysts were ascribed to the cubic $In_2O_3$ phase (PDF #65-3170). No peaks belonging to loaded metals were observed, probably due to the high dispersion of metal nanoparticles in the catalysts.[41] $In_2O_3$ loaded with various metals and pure $In_2O_3$ were used to evaluate the thermal catalytic $CO_2$ hydrogenation at 250 °C and atmosphere pressure. As shown in Figure 4.2 and Table 4.1, pure $In_2O_3$ showed a methanol production rate of 29.5 μmol $g^{-1}$ $h^{-1}$ with a selectivity of 21.3%. The catalytic activity for methanol production was remarkably improved by loading metals (Ru, Rh, Pt and Pd), except Cu. Whereas only loading Ru can improve both the activity and selectivity of methanol, reaching 122.8

μmol $g^{-1}$ $h^{-1}$ and 35.2%, respectively, and loading other metals on $In_2O_3$ obviously reduced the selectivity of methanol. Therefore, Ru was selected as the promoter for improving the performance of $In_2O_3$ in photothermal catalytic $CO_2$ hydrogenation to methanol in the following part of this chapter.

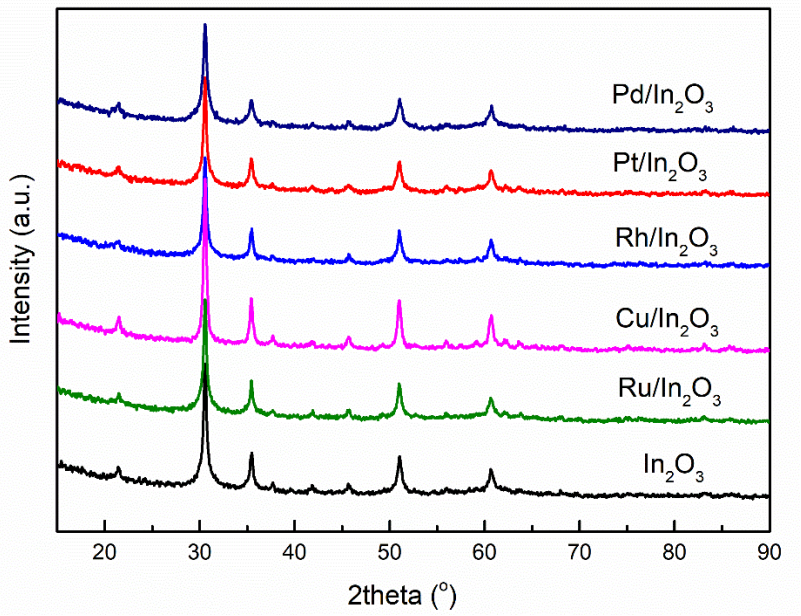


**Figure 4.1** XRD patterns for $M/In_2O_3$ (M = Ru, Cu, Rh, Pt, Pd) catalysts

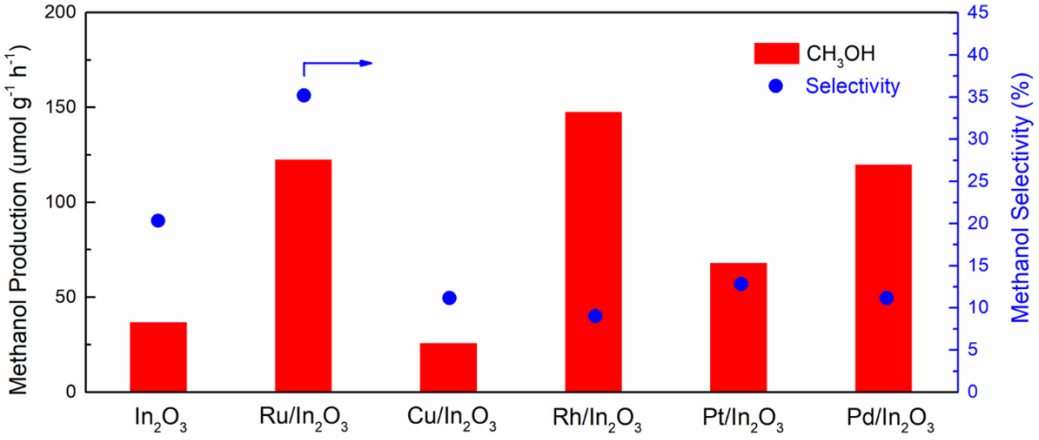


**Figure 4.2** Screening of metal catalysts for $In_2O_3$ in $CO_2$ hydrogenation to $CH_3OH$ under dark conditions: 10 mg of catalyst, 250 °C, 1bar, $CO_2/H_2$ = 5/15 mL $min^{-1}$.

### 4.3.2 Structure and morphology characterization

I then prepared a series of $Ru/In_2O_3$ catalysts with different Ru amount (denoted as $xRu/In_2O_3$, where x is the weight percent of Ru). The exact content of Ru in the catalysts

was analyzed by the inductively coupled plasma-optical emission spectrometry (ICP-OES), as shown in Table 4.2. The results demonstrated the consistency between the designed and real component of synthesized catalysts. The structure of catalysts was characterized by XRD and the results were shown in Figure 4.3. The diffraction peaks of $xRu/In_2O_3$ were all ascribed to cubic $In_2O_3$ phase with no peaks assigned to Ru species, indicating the high dispersion of Ru on the catalysts. I also calculated the size of $In_2O_3$ particles based on Debye-Scherrer equation and the results were shown in Table 4.2. The size of pure $In_2O_3$ was calculated to be ~17.5 nm, while all $Ru/In_2O_3$ particles were within ~ 20 nm, indicating that the $In_2O_3$ nanoparticles slightly grew with the introduction of Ru species. The morphology of catalysts was recorded by scanning electron microscope (SEM), as shown in Figure 4.4. Both pure $In_2O_3$ and $Ru/In_2O_3$ showed similar rod-like structures with around 1~2 μm in length and ~200 nm in width. In addition, high resolution transmission electron microscope (HRTEM) was utilized to analyze the nano structure of $2Ru/In_2O_3$ catalyst, as shown in Figure 4.5 and Figure 4.6. The images showed that the catalysts were composed of $In_2O_3$ nanoparticles with ~20 nm in diameter, in correspondence with the size calculation results from XRD. The lattice distance of 0.29 nm was attributed to the facet of $In_2O_3$ (222), and the Ru nanoparticles were also observed on the surface of $In_2O_3$ with a lattice distance of 0.21 nm, corresponding to the facet of Ru (101). The energy-dispersive X-ray spectroscopy (EDS) elemental distribution of $2Ru/In_2O_3$, as shown in Figure 4.5c-f, demonstrated that Ru was highly dispersed on the surface of $In_2O_3$ nanorod, confirming the presence of Ru in the catalyst. The high dispersion of Ru also explained the absence of Ru diffraction peaks in XRD result.

**Table 4.2** Physical and chemical properties of catalysts

| Catalysts | Ru amount (wt%)[a] | Particle size (nm)[b] | Specific surface area ($m^2\ g^{-1}$)[c] | Oxygen vacancy concentration (%)[d] |
|---|---|---|---|---|
| $In_2O_3$ | 0 | 17.5 | 82.76 | 24.9 |

| | | | | |
|---|---|---|---|---|
| 0.5Ru/$In_2O_3$ | 0.48 | 20.1 | 79.81 | 32.0 |
| 1Ru/$In_2O_3$ | 0.89 | 20.4 | 76.42 | 35.7 |
| 2Ru/$In_2O_3$ | 1.75 | 21.3 | 77.83 | 38.7 |
| 5Ru/$In_2O_3$ | 4.48 | 21.2 | 78.21 | 46.2 |

a. ICP-OES analysis, b. calculated by Scherrer equation using XRD data, c. derived from $N_2$ absorption-desorption study, d. calculated by XPS data.

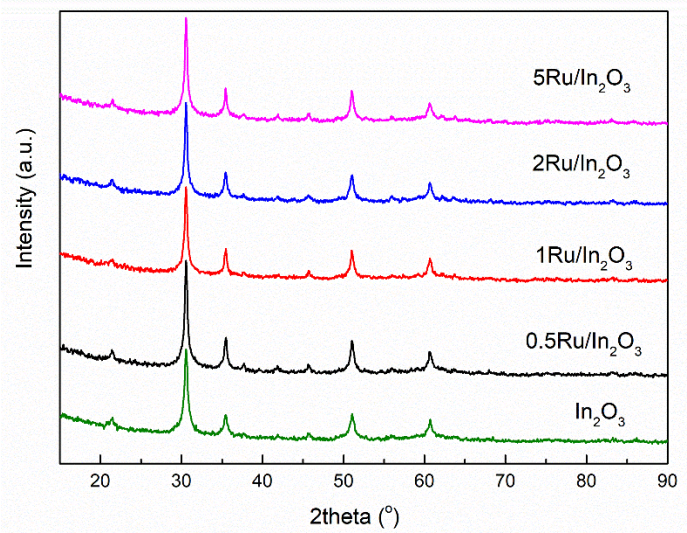


**Figure 4.3** XRD patterns for Ru/$In_2O_3$ with different Ru amount

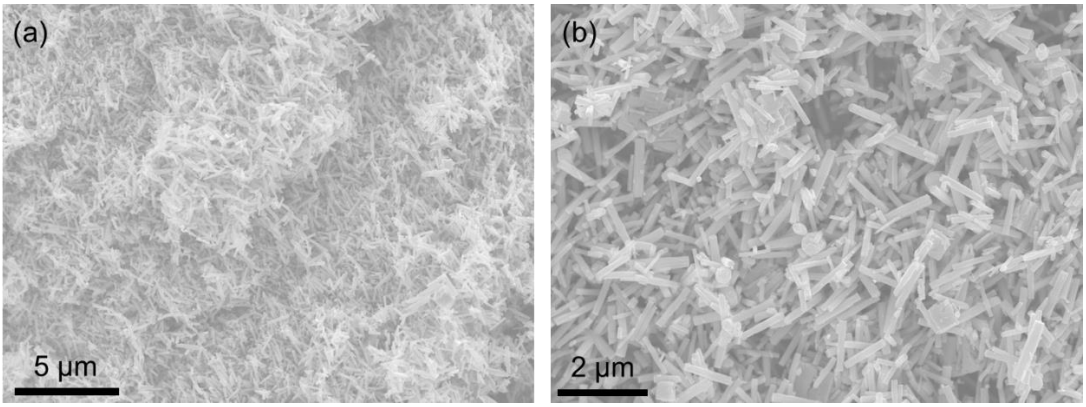


**Figure 4.4** SEM images of (a) $In_2O_3$ and (b) 2Ru/$In_2O_3$.

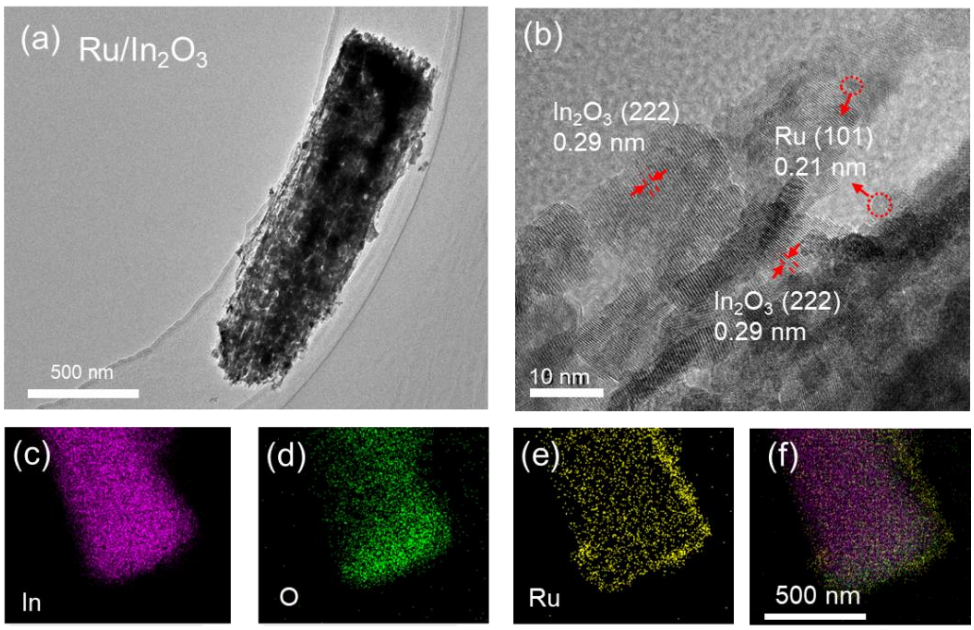


**Figure 4.5** Morphology of $Ru/In_2O_3$ catalyst. (a) and (b): TEM and HRTEM images, (c-f) elemental distribution spectra (EDS) of $Ru/In_2O_3$.

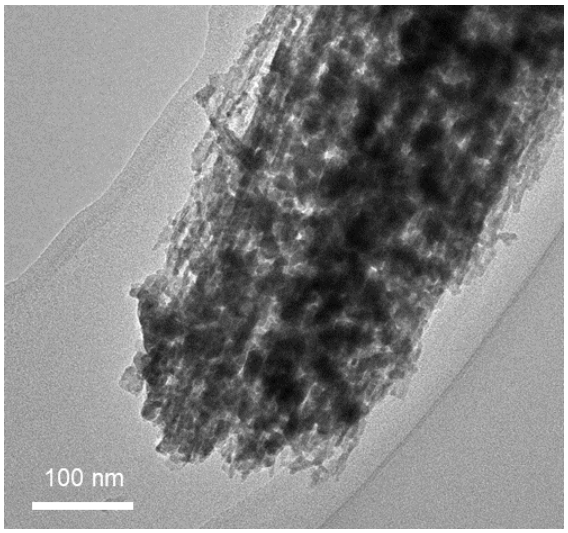


**Figure 4.6** TEM image for $2Ru/In_2O_3$

The chemical states of elements in the catalysts were identified by XPS analysis, as shown in Figure 4.7, Figure 4.8 and Figure 4.9. Figure 4.7 illustrated that the In3d spectra in both $In_2O_3$ and $2Ru/In_2O_3$ showed similar peaks, and the peak centered at 444.2 eV could be attributed to $In^{3+}$ 3d5/2, corresponding to the abundant In-O bonds in catalysts.[42] The oxygen vacancies in catalysts could be confirmed by O1s spectra in Figure 4.8b and Figure 4.9. The peaks centered at 529.7 eV, 531.3 eV and 532.4 eV

could be assigned to lattice oxygen, oxygen vacancy and absorbed OH, respectively.[43] I calculated the relative amount of oxygen vacancies on the surface of different catalysts according to references and the results were shown in Table 4.2. The concentration of oxygen vacancies was 24.9 % in bare $In_2O_3$, obviously lower than that of all $Ru/In_2O_3$ catalysts. In addition, the concentration of oxygen vacancies on the surface of $xRu/In_2O_3$ catalysts was increased as the amount of Ru was elevated from 0.5 wt.% to 5 wt.%, indicating that Ru nanoparticles facilitated the formation of oxygen vacancies in catalysts, which implied that the oxygen vacancies played a key role during the reaction process of $CO_2$ hydrogenation. The Ru3d spectra showed two peaks centered at 281.8 eV and 280.6 eV (Figure 4.8c), ascribed to $Ru^{x+}$ and $Ru^0$ respectively, implying that the Ru nanoparticles were partially oxidized in the catalysts, which could be attributed to the possible Ru-O bond at the interface between Ru nanoparticles and $In_2O_3$.[44, 45]

Furthermore, the interaction between Ru and $In_2O_3$ in $Ru/In_2O_3$ catalysts was also studied by $H_2$- temperature programmed reduction ($H_2$-TPR), and the patterns were shown in Figure 4.8d. The profile of $In_2O_3$ exhibited a single small peak at 152 $^oC$, which could be attributed to the formation of oxygen vacancy.[46] As for $2Ru/In_2O_3$, two obvious peaks at 137$^oC$ and 152 $^oC$ appeared in the pattern. The former peak was attributed to the reduction of $RuO_x$ to metallic Ru and the latter peak was attributed to the formation of oxygen vacancies.[47] Compared with pure $In_2O_3$, the obviously lower temperature of oxygen vacancy formation with larger peak area suggested that the introduction of Ru in catalysts promoted the reduction of $In_2O_3$ through $H_2$ dissipation on Ru, therefore facilitating the generation of oxygen vacancies, in agreement with the XPS analysis.[48]

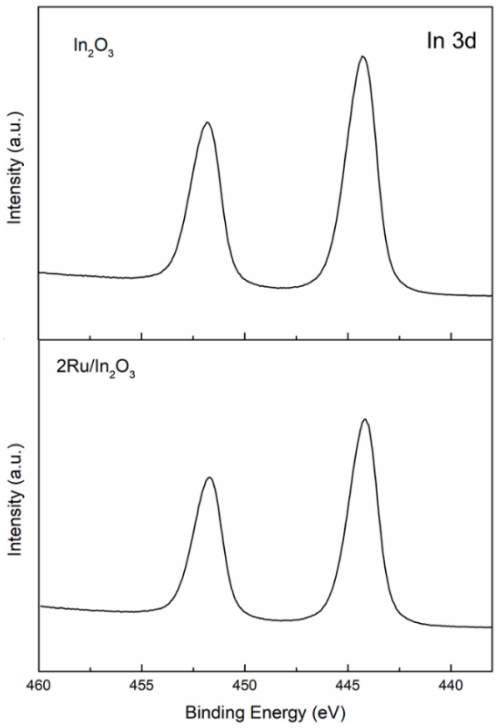


**Figure 4.7** XPS patterns for In 3d in $In_2O_3$ and $2Ru/In_2O_3$.

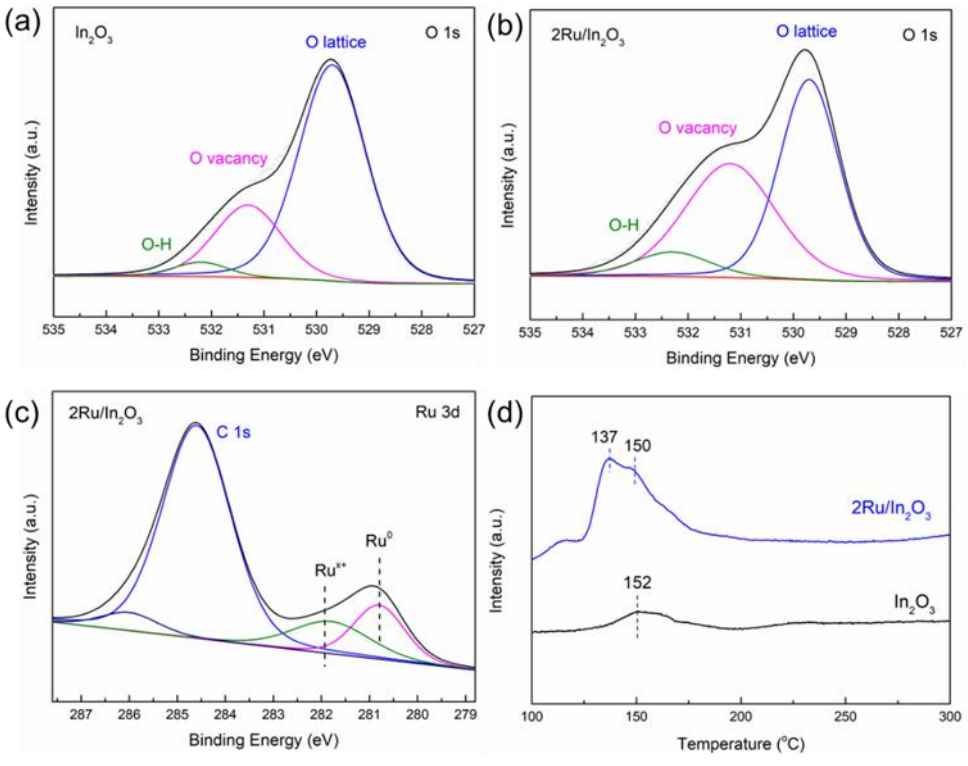


**Figure 4.8** Structural characterization of $Ru/In_2O_3$. XPS patterns for O 1s in (a) $In_2O_3$, (b) $2Ru/In_2O_3$ and for Ru 3d in (c) $2Ru/In_2O_3$. (c) $H_2$-TPR patterns for $In_2O_3$ and $2Ru/In_2O_3$.

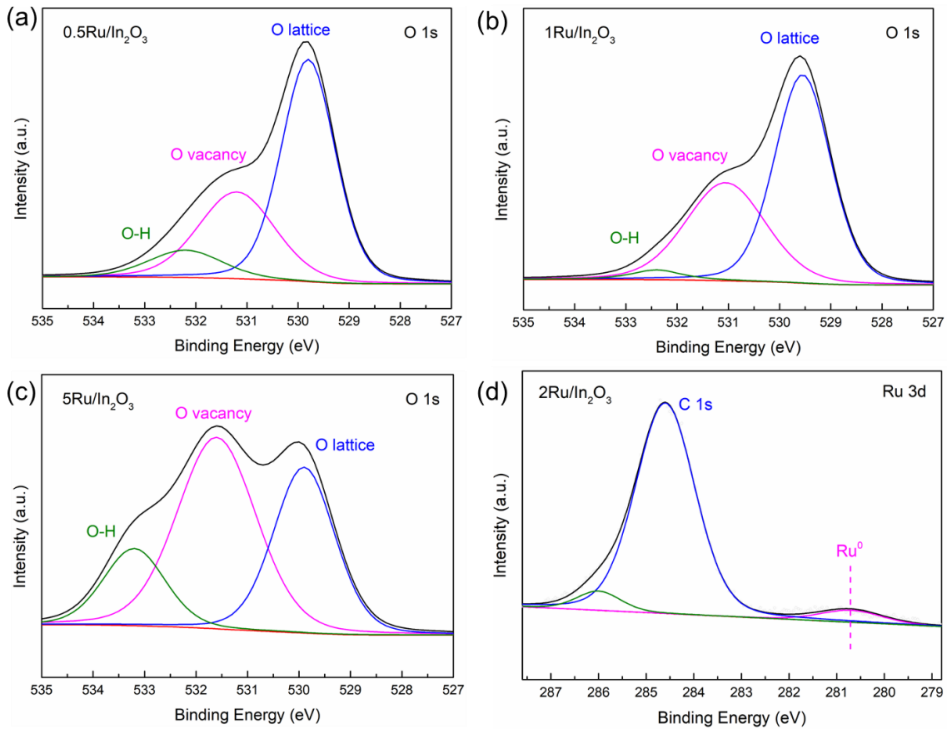


**Figure 4.9** XPS patterns of (a) O 1s for 0.5Ru/$In_2O_3$, (b) O 1s for 1Ru/$In_2O_3$, (c) O 1s for 5Ru/$In_2O_3$, and (d) Ru 3d for used 2Ru/$In_2O_3$.

X-ray absorption near edge structure (XANES) analysis was employed to investigate the chemical status of indium in $In_2O_3$ and 2Ru/$In_2O_3$ catalysts. As shown in the In K-edge XANES (Figure 4.10), the absorption edge in 2Ru/$In_2O_3$ was shifted to a lower energy compared with pure $In_2O_3$, suggesting a lower average coordination number around In atoms, which could be attributed to the more oxygen vacancies in 2Ru/$In_2O_3$.[35] In addition, the Raman spectra also demonstrated that 2Ru/$In_2O_3$ contained more oxygen vacancies than pure $In_2O_3$.[49] Figure 4.11 showed the Raman spectra of $In_2O_3$ and 2Ru/$In_2O_3$ at room temperature. The peaks centered at 303, 495 and 629 $cm^{-1}$ could be assigned to the vibration of octahedral $InO_6$ in $In_2O_3$. The former one was attributed to the bending vibration, and the latter two peaks at 495 and 629 $cm^{-1}$ were due to the stretching vibration. In addition, the small peak at 368 $cm^{-1}$ was usually interpreted as the stretching vibration of In-O-In, which could reflect the existence of oxygen vacancies in both catalysts.[50] Furthermore, the ratio of two peaks ($I_2/I_1$) at 303 $cm^{-1}$ ($I_1$) and 368 $cm^{-1}$ ($I_2$) could quantify the amount of oxygen vacancies in different

catalysts.[49] For pure $In_2O_3$, the value of $I_2/I_1$ is 0.10, while for $2Ru/In_2O_3$, the value is 0.27, suggesting more oxygen vacancies in $2Ru/In_2O_3$.

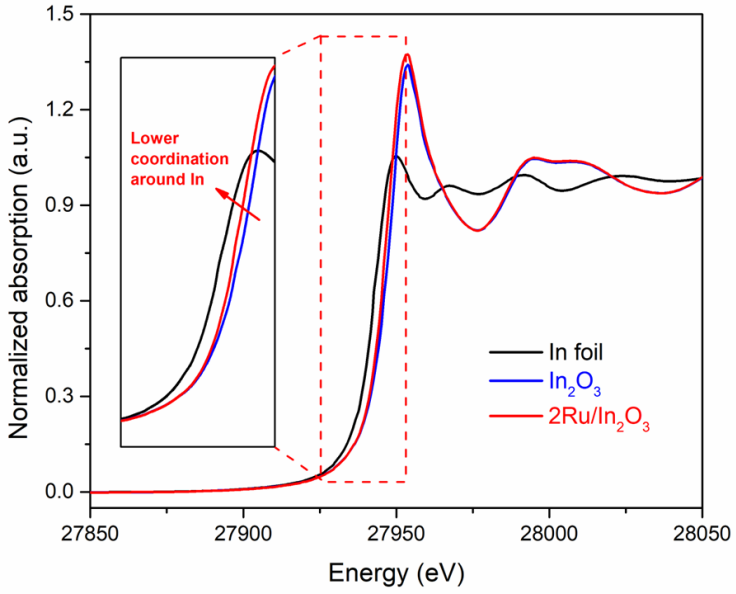


**Figure 4.10** Normalized In K-edge XANES spectra of $In_2O_3$ and $2Ru/In_2O_3$

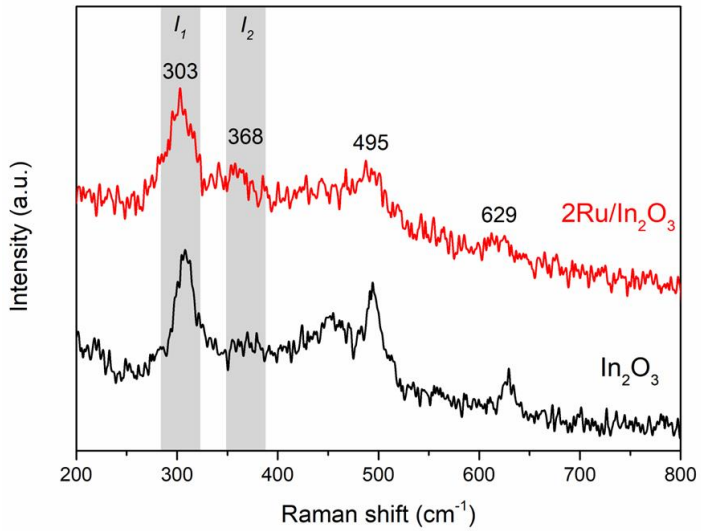


**Figure 4.11** Visible Raman spectra of $In_2O_3$ and $2Ru/In_2O_3$ at room temperature.

### 4.3.3 Photothermal catalytic activity measurement

The above synthesized $xRu/In_2O_3$ catalysts were then utilized for solar-driven photothermal catalytic $CO_2$ hydrogenation at atmosphere pressure, and the results were shown in Figure 4.12 and Figure 4.13. A 300 W Xenon arc lamp equipped with an L42 filter ($\lambda$>400 nm) was utilized as the only energy source. Upon light incidence, the

catalyst temperature was monitored to increase rapidly to the equilibrium temperature within 10 min (Figure 4.12). As depicted in Figure 4.13a, the equilibrium temperature of catalysts exhibited a linear dependence on irradiation intensity. All $xRu/In_2O_3$ catalysts showed much higher temperatures than that on pure $In_2O_3$ under the same condition, suggesting that Ru nanoparticles could absorb and convert more photon energy into phonon energy, therefore increasing the catalyst temperature. In general, only CO and methanol were detected over all catalysts in the output gas. With the introduction of Ru on $In_2O_3$ support, both CO and $CH_3OH$ production increased obviously, compared with pure $In_2O_3$ (Figure 4.14). Under the light irradiation intensity of 1413 mW $cm^{-2}$, the optimized catalyst $2Ru/In_2O_3$, exhibited the highest methanol production (280.4 μmol $g^{-1}$ $h^{-1}$), ~50 times higher than that on pure $In_2O_3$ catalyst (5.2 μmol $g^{-1}$ $h^{-1}$). Figure 4.13c showed that the methanol selectivity over $xRu/In_2O_3$ catalysts declined with increasing light intensity, due to the competitive endothermic RWGS reaction. It is worth noting that with the increase of Ru amount, the activity and selectivity of methanol rose at first (from 0.5 wt% Ru to 2.0 wt% Ru) and then declined (from 2.0 wt% Ru to 5.0 wt% Ru), implying that $2Ru/In_2O_3$ enhanced $CH_3OH$ production while inhibited CO yield to some extent in comparison with other $Ru/In_2O_3$ catalysts, probably because of the excessive Ru covered on the surface blocking some active sites. Moreover, for comparison, I also prepared commercial methanol synthesis catalyst Cu/Zn/Al and Ru/commercial $In_2O_3$ ($2Ru/com\text{-}In_2O_3$), as well as $Ru/In_2O_3$ by wet impregnation method ($2Ru/In_2O_3$-wet). As shown in Figure 4.13d, the yield and selectivity of methanol over $2Ru/In_2O_3$ were much higher than those of other control catalysts. Compared with the previous works[27-29, 51, 52], $2Ru/In_2O_3$ exhibited an impressive solar methanol yield at atmospheric pressure (Table 4.3).

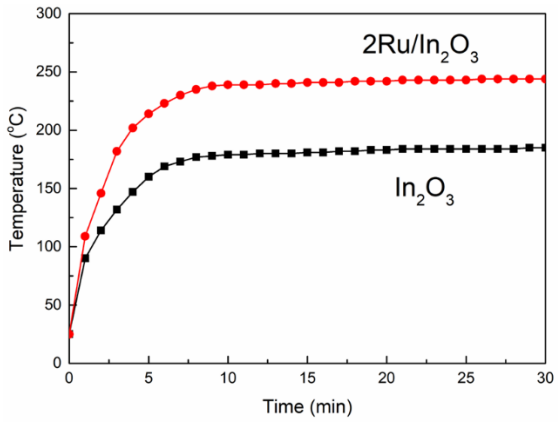


**Figure 4.12** Temporal temperature evolution over the catalysts under irradiation (1.41 W $cm^{-2}$)

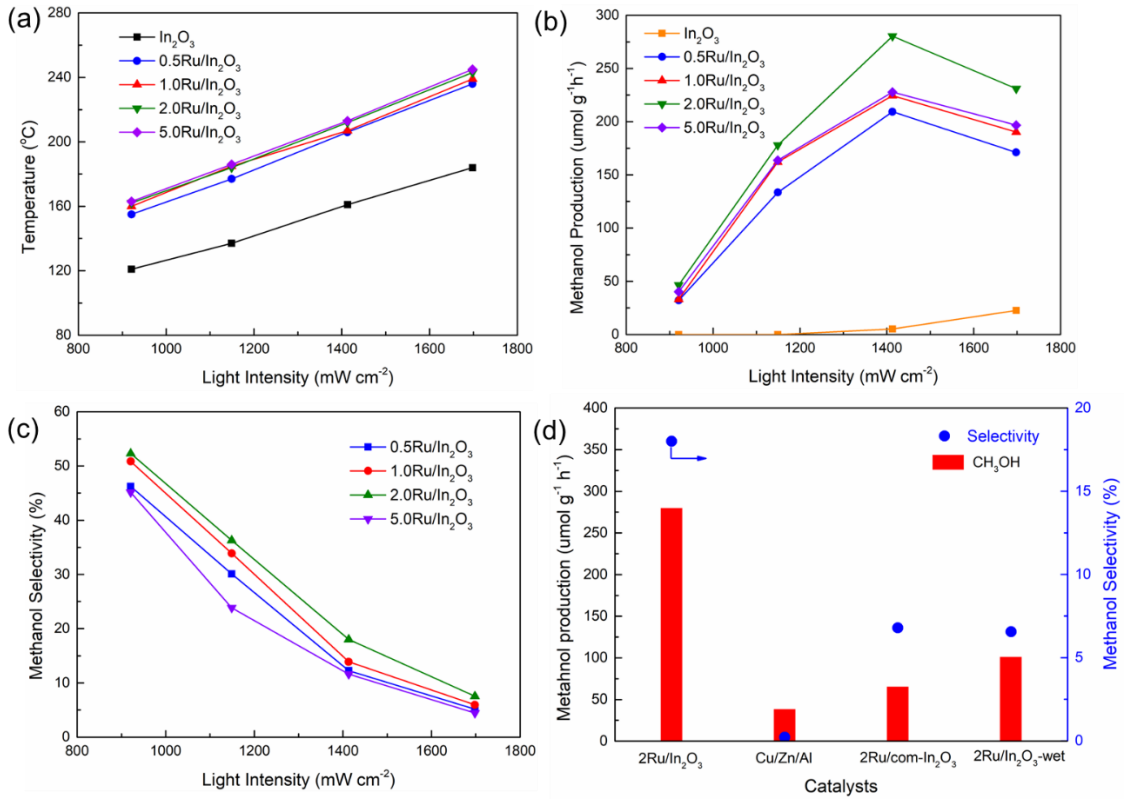


**Figure 4.13** Solar-driven photothermal catalytic $CO_2$ hydrogenation. (a) Monitored catalyst temperatures with different light intensities, (b) solar methanol generation rate and (c) selectivity over x$Ru/In_2O_3$ catalysts, (d) comparison of methanol activity over different catalysts.

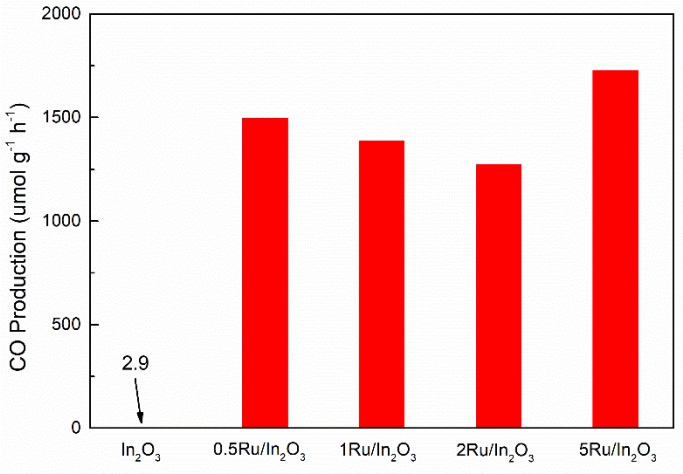


**Figure 4.14** CO production over $xRu/In_2O_3$ catalysts in photothermal $CO_2$ hydrogenation (under the irradiation of 1413 W $cm^{-2}$)

**Table 4.3** Comparison of methanol production and selectivity for $CO_2$ hydrogenation catalysts at atmospheric pressure.

| Catalyst | Reactor | Gas composition | Catalytic condition | $CH_3OH$ production rate | Selectivity | Ref. |
|---|---|---|---|---|---|---|
| $2Ru/In_2O_3$ | flow | $CO_2/H_2$ = 1/3<br>20 mL $min^{-1}$ | 300 W Xe lamp<br>(1.41 W $cm^{-2}$) | 280.4 μmol $g_{cat}^{-1}$ $h^{-1}$ | 18.0% | This work |
| $In_2O_3$ | flow | $CO_2/H_2$ = 1/3<br>20 mL $min^{-1}$ | 300 W Xe lamp<br>(1.41 W $cm^{-2}$) | 5.2 μmol $g_{cat}^{-1}$ $h^{-1}$ | 53.5% | This work |
| $2Ru/In_2O_3$-wet | flow | $CO_2/H_2$ = 1/3<br>20 mL $min^{-1}$ | 300 W Xe lamp<br>(1.41 W $cm^{-2}$) | 101.8 μmol $g_{cat}^{-1}$ $h^{-1}$ | 6.55% | This work |
| $In_2O_{3-x}(OH)_y$ | flow | $CO_2/H_2$ = 1/3<br>8 mL $min^{-1}$ | 130 W Xe arc lamp,<br>(5.0 W $cm^{-2}$) | 63.73 μmol $g_{cat}^{-1}$ $h^{-1}$ | 53.03% | [27] |
| $Bi_xIn_{2-x}O_3$ | Flow | $CO_2/H_2$ = 1/3<br>4 mL $min^{-1}$ | 300 W Xe lamp<br>(2.0 W $cm^{-2}$) | 158 μmol $g_{cat}^{-1}$ $h^{-1}$ | 14.7% | [28] |

| | | | | | | |
|---|---|---|---|---|---|---|
| Cu/ZnO | flow | $CO_2/H_2$ = 1/3<br>20 mL $min^{-1}$ | Visible light (0.58 W $cm^{-2}$),<br>220 °C | 127.8 μmol $g_{cat}^{-1}$ $h^{-1}$ | 7.1% | [51] |
| $[Zn_{1.5}Cu_{1.5}Ga(OH)_8]^{+}{}_2[Cu(OH)_4]^{2-}$ | Batch | $H_2$ (1.67 mmol)<br>$CO_2$ (0.177 mmol) | 500 W Xe lamp,<br>150 °C | 0.49 μmol $g_{cat}^{-1}$ $h^{-1}$ | 87.50% | [29] |
| 37.5PdCuZn/SiC | Flow | $CO_2/H_2$ = 1/9<br>100 mL $min^{-1}$ | 200 °C | 110 μmol $g_{cat}^{-1}$ $h^{-1}$ | 80.9% | [52] |

### 4.3.4 Light enhancement effect and reaction mechanism

Light irradiation can not only increase the surface temperature of catalysts by photothermal heating effect to promote the $CO_2$ hydrogenation but also potentially induces the energetic hot carriers-mediated activation of reactants to enhance the catalytic activity.[53] In order to investigate the mechanism of this photothermal process, I carried out a series of photo-assisted thermal catalytic $CO_2$ hydrogenation at different reaction temperatures and with or without the irradiation of light ($400 < \lambda < 800$ nm, 644.2 mW $cm^{-2}$). In this reaction process, an electrical heater with a temperature controller was equipped to alleviate the photo-induced heating effect on the catalysts. Figure 4.15a and 4.15b illustrated the production rate and selectivity of methanol over catalysts at 250 °C with and without light irradiation. In the dark condition, the optimized $2Ru/In_2O_3$ exhibited a methanol production much higher than that on pure $In_2O_3$. Upon light irradiation, the methanol yield over $2Ru/In_2O_3$ was increased from 122.8 μmol $g^{-1}$ $h^{-1}$ to 178.0 μmol $g^{-1}$ $h^{-1}$, promoted by nearly 50% than dark condition. Notably, there was almost no change in the methanol production over pure $In_2O_3$ between dark and light conditions, revealing that the visible light exhibited no effect on $In_2O_3$ and the light-induced enhancement in $2Ru/In_2O_3$ was mainly attributed to the Ru nanoparticles, possibly due to the coupling of light-to-heat and photo-induced hot carrier activation of reactants in Ru. Meanwhile, the selectivity of methanol remained

almost no change under light irradiation, suggesting that the irradiation promoted the production of both CO and methanol.

To further study the mechanism of light-enhanced methanol production, I carried out a series of experiments on $2Ru/In_2O_3$ at different temperatures under dark and illumination. As shown in Figure 4.15c, due to the exothermic property of $CO_2$ hydrogenation to methanol, there was a maximum production rate of methanol under dark or illumination, and the value of the maximum production rate of methanol and the corresponding reaction temperature were obviously different in these two conditions. Specifically, under dark condition, the maximum production rate of methanol obtained at 290 $^oC$ was 254.9 μmol $g^{-1}$ $h^{-1}$, whereas, under light irradiation, the methanol production rate reached a maximum of 290.4 μmol $g^{-1}$ $h^{-1}$ at 280 $^oC$, ~20% higher than that under dark. This result demonstrated that the enhancement in the maximum methanol production rate induced by light irradiation was not caused by the temperature elevation via light heating, since, if so, the maximum methanol production rates under dark and illumination should be the same, but by the hot carriers-promoted methanol production over $2Ru/In_2O_3$ catalyst. In addition, when I focused on the methanol generation over pure $In_2O_3$ at different temperatures under dark and irradiation (Figure 4.15c), the relationship between methanol activity and temperature on $In_2O_3$ was similar to that on $2Ru/In_2O_3$. However, there was almost no difference in production at the same temperature between dark and light conditions, indicating that the light-enhancement effect on activity over $2Ru/In_2O_3$ was mainly due to the hot carriers excited from Ru nanoparticles.

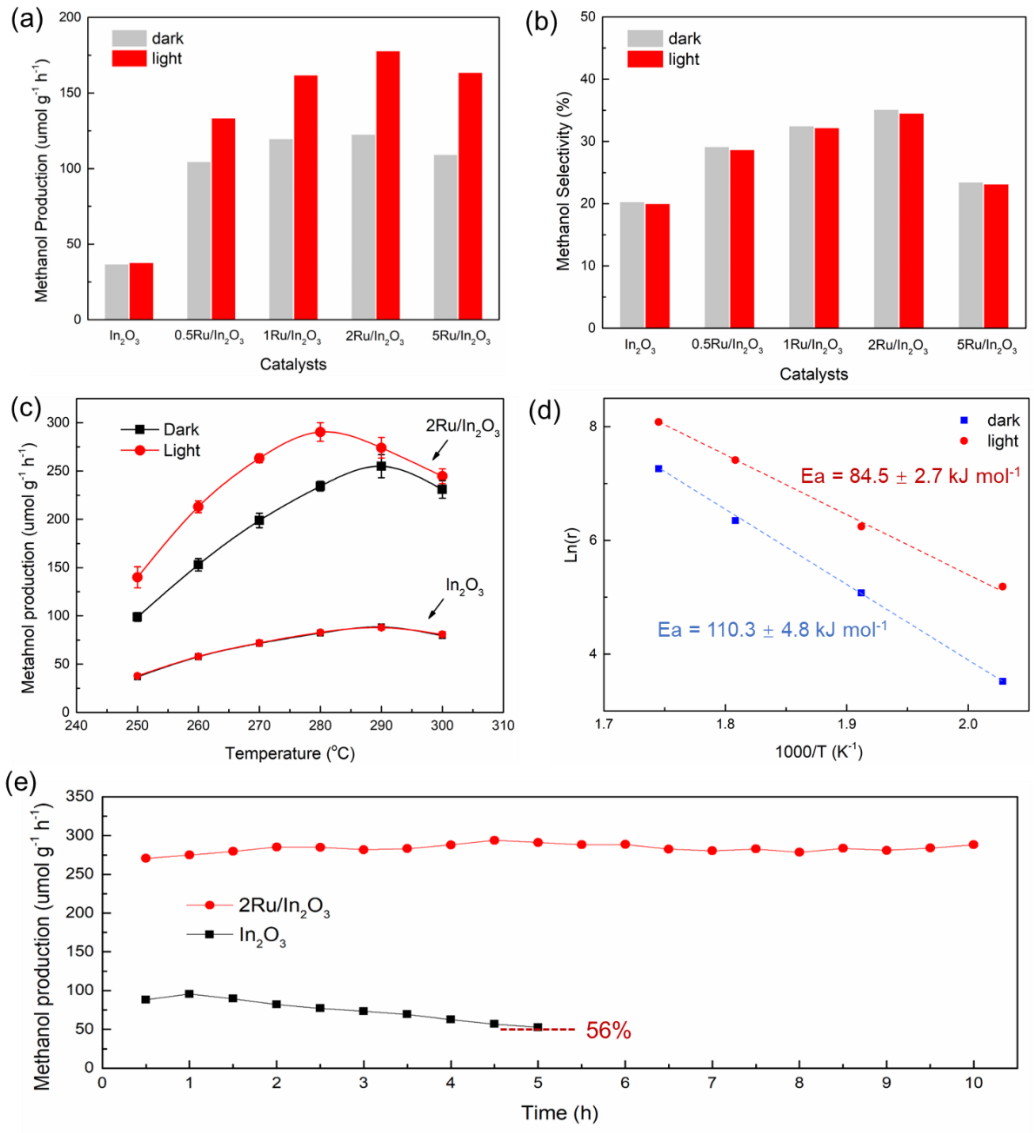


**Figure 4.15** Photo-assisted thermal catalytic $CO_2$ hydrogenation. (a) Methanol production and (b) selectivity over $In_2O_3$ and $xRu/In_2O_3$ catalysts in thermocatalytic process (dark) and photo-assisted thermocatalytic process (light) at 250 °C, (c) methanol production over $In_2O_3$ and $2Ru/In_2O_3$ as a function of temperature in dark and light, (d) Arrhenius plots for $CO_2$ conversion over $2Ru/In_2O_3$ in dark and light, (e) stability test of $In_2O_3$ and $2Ru/In_2O_3$ at 280 °C under the visible light irradiation. Irradiation condition: $400 < \lambda < 800$ nm, 644.2 mW $cm^{-2}$.

I calculated the apparent activation energy ($E_a$) of $CO_2$ conversion on $2Ru/In_2O_3$ under dark and light conditions, as shown in Figure 4.15d. With the assistance of light irradiation, the $E_a$ of $CO_2$ conversion on $Ru/In_2O_3$ decreased from 110.3 ± 4.8 kJ $mol^{-1}$

in dark to 84.5 ± 2.7 kJ $mol^{-1}$ under irradiation, indicating that light irradiation facilitated the reaction kinetics of $CO_2$ hydrogenation. In addition, the time-on-steam (TOS) photothermal catalytic performances of $In_2O_3$ and $2Ru/In_2O_3$ were carried out at 280 $^oC$ with visible light irradiation to investigate the stability of catalysts, and the results were shown in Figure 4.15e and Figure 4.16. Obviously, after 10 h reaction process, the production rate of methanol of $Ru/In_2O_3$ remained almost unchanged, while the methanol selectivity gradually increased owing to the gradually decreased CO yield. After 10 h reaction, the selectivity of methanol was increased up to 23.0 % over $2Ru/In_2O_3$. By contrast, the methanol production rate of $In_2O_3$ was decreased to only ~56% after 5 h of irradiation, indicating that the introduction of Ru significantly enhanced the stability of catalysts. Furthermore, the structure of the used catalysts showed almost no change after the long-time reaction (Figure 4.17).

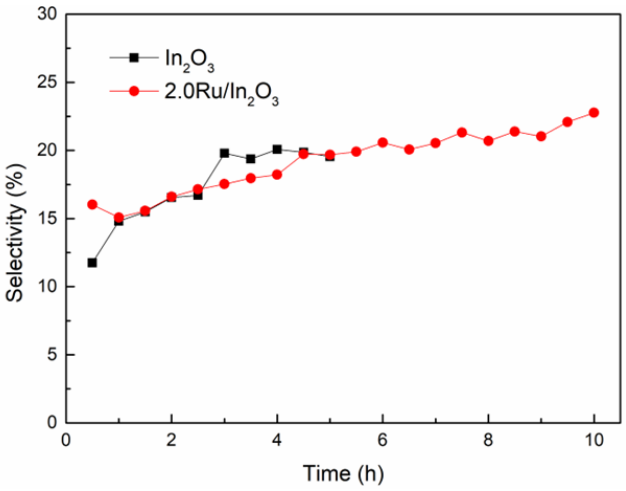


**Figure 4.16** Methanol selectivity on $In_2O_3$ and $2Ru/In_2O_3$ during the stability test

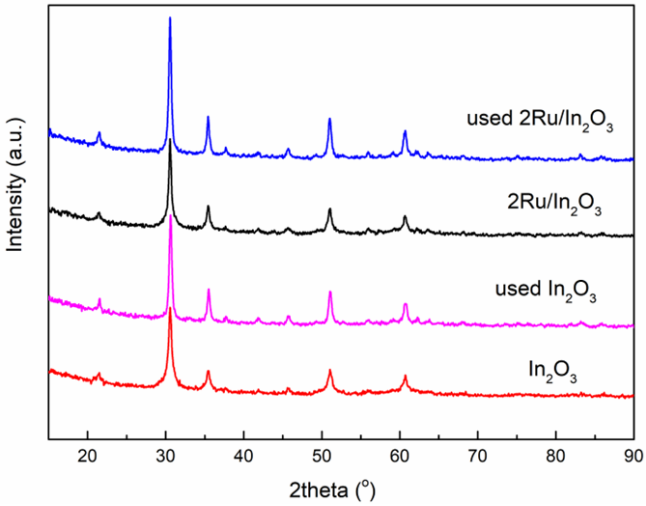


**Figure 4.17** XRD patterns for fresh and used catalysts after the stability test

The dependence of methanol production rate on light irradiation intensity over $2Ru/In_2O_3$ showed a linear relationship, as shown in Figure 4.18. This suggested that the enhancement of reaction activity was driven by hot carriers induced by light irradiation.[54] In addition, the optical absorption properties of catalysts were studied by ultraviolet-visible diffuse reflectance spectroscopy (UV-vis DRS) and the result was shown in Figure 4.19. Pure $In_2O_3$ mainly exhibited absorption in UV range, while all catalysts containing Ru nanoparticles showed much higher absorption in visible light range, which could be mainly attributed to the intra- and/or inter-band excitations of Ru nanoparticles.[54, 55] This phenomenon indicated that the hot carriers in Ru nanoparticles were initially excited by incident photons. Then part of them dissipated rapidly to elevate the surface temperature of catalyst, while others transferred to the absorbed reactants to promote the activation of reactants $CO_2$ and $H_2$, thus enhancing the activity of methanol production, which explains the extra activity increase between thermal and photothermal methanol production in Figure 4.15c.

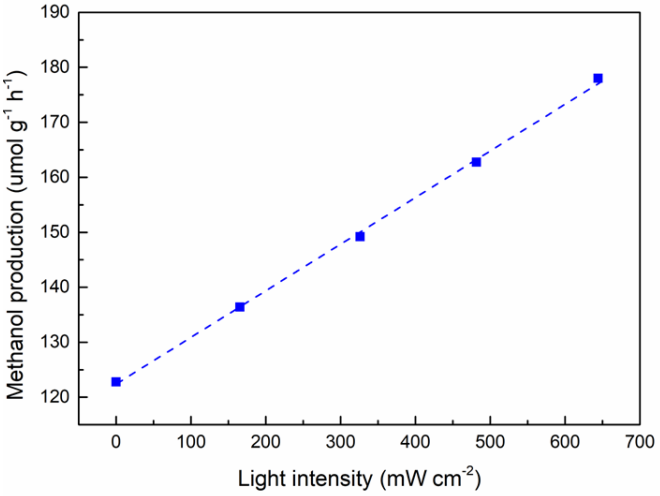


**Figure 4.18** Relationship between methanol production and light intensity on 2Ru/$In_2O_3$ at 250 °C

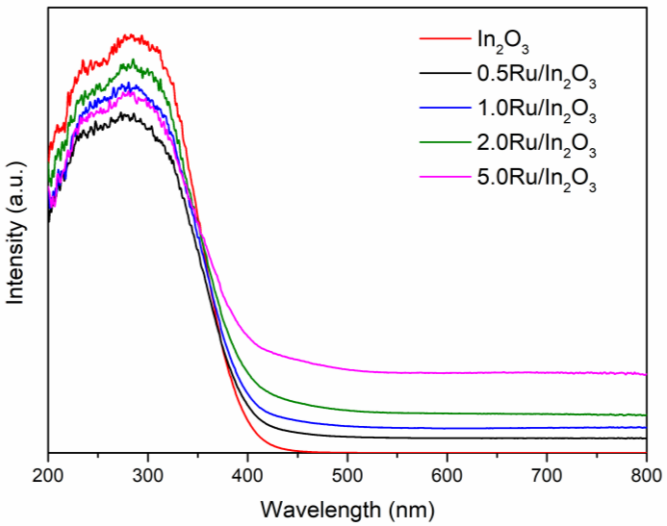


**Figure 4.19** UV-Vis DRS of $In_2O_3$ and x Ru/$In_2O_3$ ctalaysts

Based on the previous reports about methanol synthesis, it has been concluded that there are mainly two pathways for $CO_2$ hydrogenation to methanol reaction, one is hydrocarboxyl (*COOH) intermediate for the CO hydrogenation route and the other is formate (*HCOO) intermediate for the direct $CO_2$ hydrogenation route.[1, 5, 13] In order to clarify the reaction pathway on Ru/$In_2O_3$, I carried out in situ diffuse reflectance infrared fourier transform spectroscopy (DRIFTS) experiment at 200 °C and the results were shown in Figure 4.20. The broad absorption area in the range from 1200 $cm^{-1}$ to 1700 $cm^{-1}$ was assigned to the absorption of $CO_2$ on catalyst surface, including $CO_2^-$

and carbonate species.[46, 56] When I concentrated on the intermediate components in the reaction, the FTIR spectrum showed a peak centered at 2070 $cm^{-1}$, which could be attributed to CO-Ru vibration.[38] Besides, the peak centered at 1848 $cm^{-1}$ corresponded to the stretch vibration of C=O bond in *COOH species.[56-59] This indicated that the reaction process on $Ru/In_2O_3$ followed the route of RWGS-CO hydrogenation pathway, in agreement with previous reports.[49]

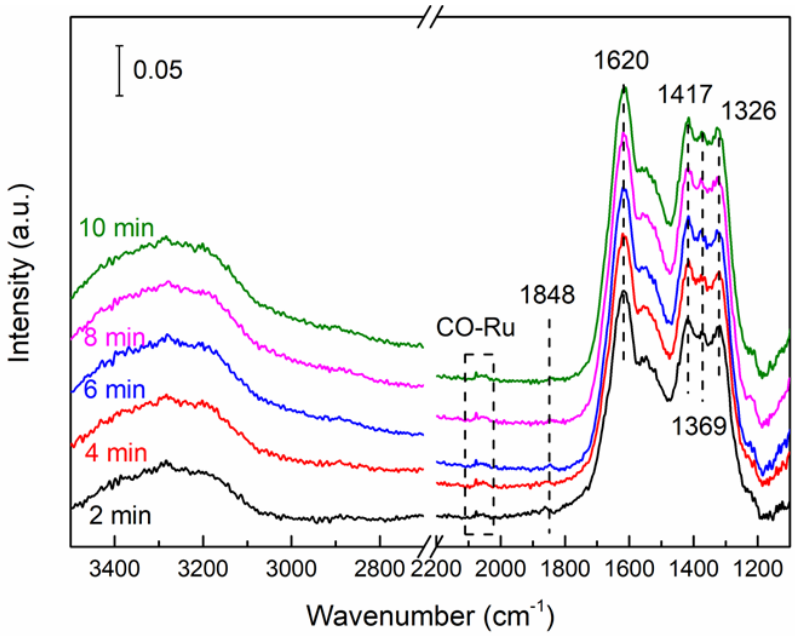


**Figure 4.20** In situ DRIFTS for $CO_2$ hydrogenation process over $2Ru/In_2O_3$ at 200 °C.

In order to further investigate the reaction mechanism of $CO_2$ hydrogenation, I conducted density functional theory (DFT) calculations about the reaction process of $CO_2$ hydrogenation to $CH_3OH$ via *CO on both $In_2O_3$ and $Ru/In_2O_3$ surface, based on the result of in situ DRIFTS and reported studies.[49] As demonstrated in Figure 4.21 and Figure 4.22, the pathway of $CO_2$ hydrogenation on $In_2O_3$ and $Ru/In_2O_3$ could be divided into two continuous processes: (1) the dissociation of $CO_2$ with the assistance of spillover *H to form adsorbed *CO via a *COOH pathway; (2) the consequent hydrogenation of *CO on catalyst surface to form methanol as final product. As shown in Figure 4.22, the overall process over $Ru/In_2O_3$ exhibited an obvious decrease in reaction state energy compared with that over pure $In_2O_3$, suggesting that the reaction process was more favorable on $Ru/In_2O_3$ surface. For process (1), the detailed

calculation results about $CO_2$ and $H_2$ dissociation showed that on $In_2O_3$-$O_v$ catalyst, the formation of *COOH was thermodynamically unfavorable due to the high reaction energy ($\Delta E$ = 1.78 eV). In contrast, the introduction of Ru nanoparticles significantly decreased this reaction energy to 0.46 eV, therefore improving *CO generation, the important intermediate for $CO_2$ conversion. As for process (2), the hydrogenation process also showed a decreased energy with the assistance of Ru. As analyzed above, the oxygen vacancies ($O_v$) on $In_2O_3$ surface also participated in the reaction process of $CO_2$ hydrogenation to methanol, usually as the absorption sites of oxygenate species. In this case, the reaction intermediate $H_xCO$ was absorbed at the surface oxygen vacancy site in the hydrogenation process to finally form methanol. For comparison, I also calculated the reaction energy of process (2) on Ru site instead of oxygen vacancy site (Figure 4.23). Obviously, the reaction process from *HCO to $CH_3OH$ on Ru site required $\Delta E$ = 0.28 eV, much higher than that on oxygen vacancy site ($\Delta E$ = - 2.96 eV), suggesting that oxygen vacancy played an important role in the hydrogenation process.

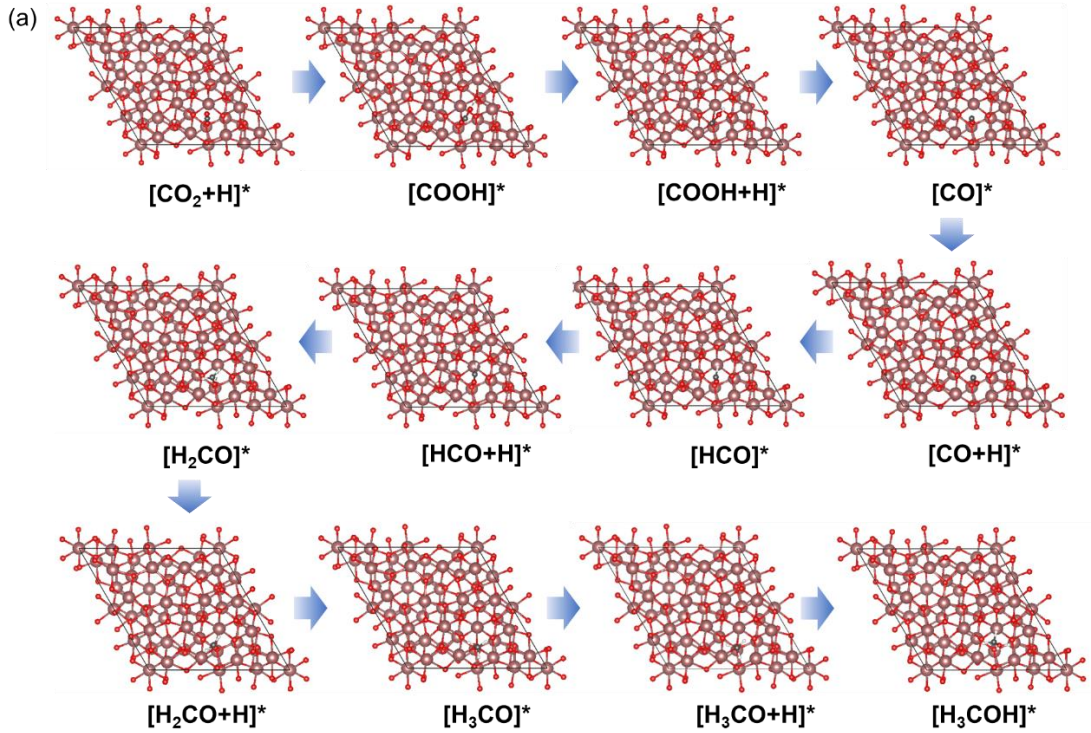

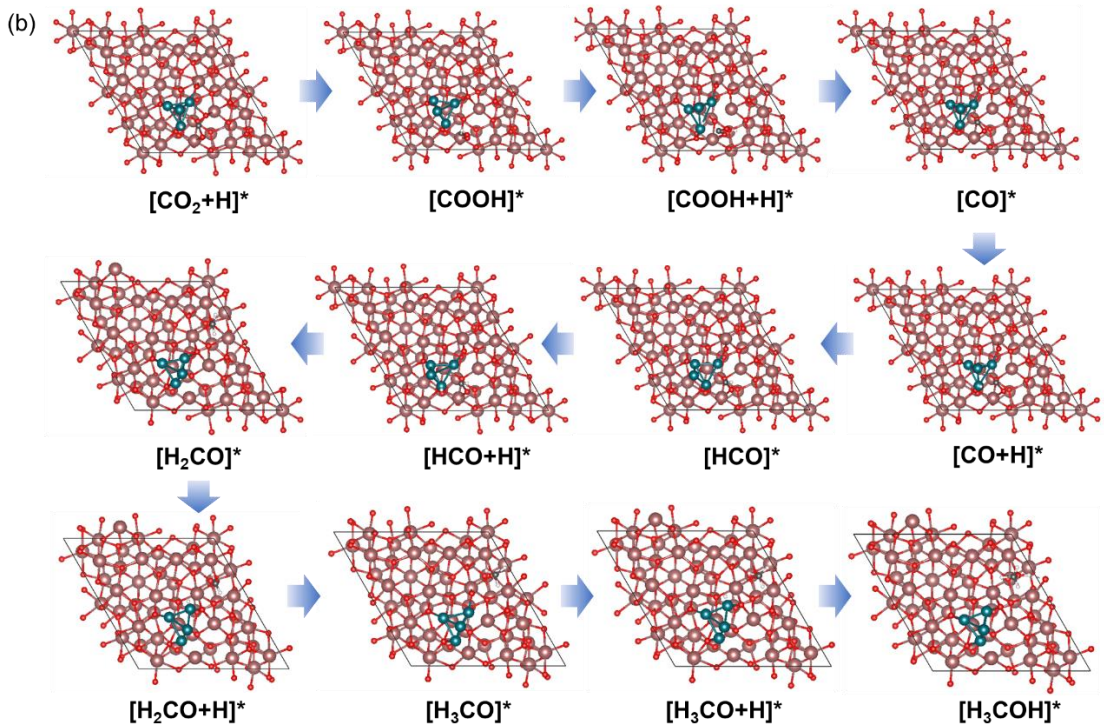


**Figure 4.21** The configurations of all reaction intermediates involved in $CO_2$ hydrogenation process to methanol on (a) $In_2O_3$-$O_v$ (111) and (b) $Ru_4/In_2O_3$-$O_v$ (111).

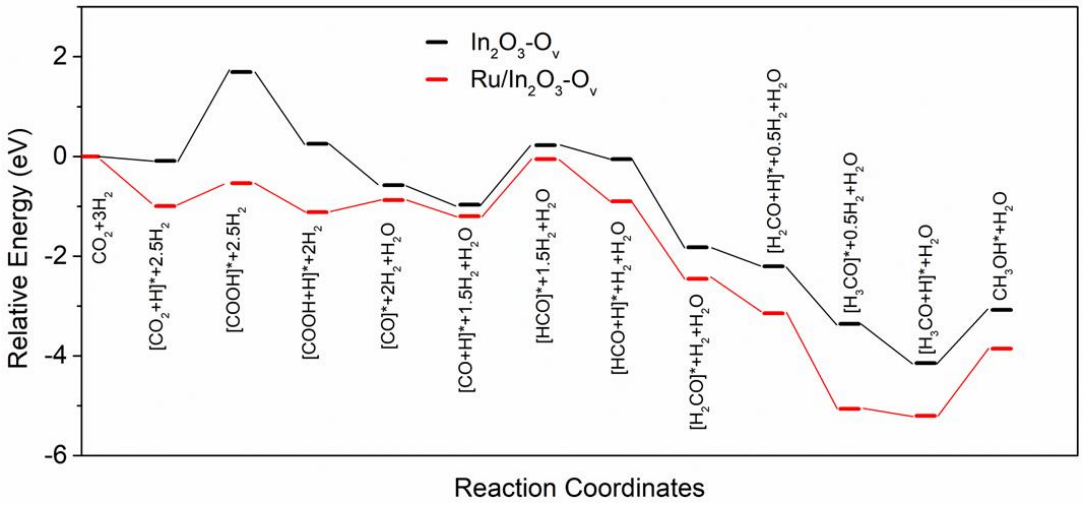


**Figure 4.22** Energy profiles for $CO_2$ hydrogenation to methanol over $In_2O_3$-$O_v$ (111) and $Ru_4/In_2O_3$-$O_v$ (111) models.

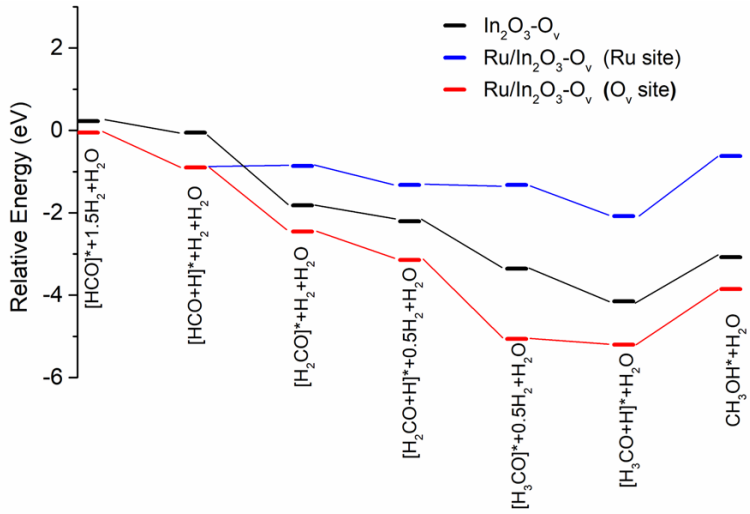


**Figure 4.23** Energy profiles for process (2) *CO hydrogenation to methanol over $In_2O_3$-Ov (111), $Ru_4/In_2O_3$-Ov (111) (Ru site) and $Ru_4/In_2O_3$-Ov (111) ($O_v$ site) models

On the base of the above analysis and discussion, I proposed the reaction mechanism of photothermal $CH_3OH$ synthesis from $CO_2$ hydrogenation over $Ru/In_2O_3$, as depicted in Figure 4.24. The interaction between Ru and $In_2O_3$ increased the generation of surface oxygen vacancies ($O_v$), which provided more absorption sites for $CO_2$. Initially, hydrogen and $CO_2$ were adsorbed on the Ru surface and $O_v$ of $In_2O_3$, respectively. The activation and conversion of reactants were facilitated by the interaction between Ru metal and $In_2O_3$ support and then formed adsorbed intermediate *CO via *COOH. Moreover, with the introduction of light, the excited hot carriers in Ru nanoparticles not only increased the surface temperature by dissipation to accelerate the reaction rate, but also directly enhanced the activation of $H_2$ and $CO_2$ and the conversion of intermediates to form adsorbed *CO. On one hand, CO was prone to be adsorbed on Ru site, leading to the decrease of CO generation as product to some extent. On the other hand, the oxygen vacancies facilitated the hydrogenation of *CO to $CH_3OH$, increasing the formation of methanol as final product. Therefore, the process of methanol generation was promoted on $Ru/In_2O_3$ catalyst.

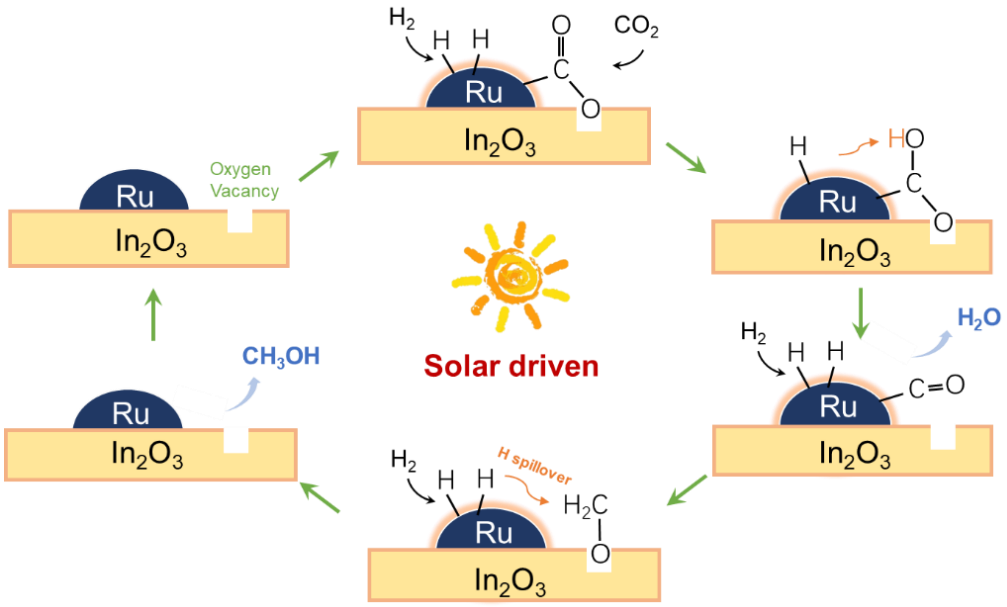


**Figure 4.24** Proposed mechanism for photothermal $CH_3OH$ synthesis from $CO_2$ hydrogenation on $Ru/In_2O_3$ catalysts

## 4.4 Conclusion

In summary, $Ru/In_2O_3$ catalyst was synthesized for highly efficient and stable photothermal $CH_3OH$ production from $CO_2$ hydrogenation under atmospheric pressure. Under light irradiation, Ru nanoparticles not only efficiently convert solar energy into thermal energy to elevate the catalyst temperature, but also generate considerable hot carriers, which could synergistically promote the activation of adsorbed $H_2$ and $CO_2$ to form the essential intermediate *CO via *COOH. Furthermore, the generation of surface oxygen vacancies in $In_2O_3$ is promoted by Ru nanoparticles, which favors the consequent hydrogenation process of *CO to form final product methanol. As a result, a remarkable solar methanol production rate of 280.4 μmol $g^{-1}$ $h^{-1}$ was obtained over the optimized $Ru/In_2O_3$ catalyst. This chapter provides a promising strategy for photothermal methanol production via $CO_2$ hydrogenation under mild conditions.

## References

[1] E.C. Ra, K.Y. Kim, E.H. Kim, H. Lee, K. An, J.S. Lee, Recycling Carbon Dioxide through Catalytic Hydrogenation: Recent Key Developments and Perspectives, ACS Catalysis, 10 (2020) 11318-11345.

[2] A. Chatterjee, M.M. Gierach, A.J. Sutton, R.A. Feely, D. Crisp, A. Eldering, M.R. Gunson, C.W. O'Dell, B.B. Stephens, D.S. Schimel, Influence of El Niño on atmospheric $CO_2$ over the tropical Pacific Ocean: Findings from NASA's OCO-2 mission, Science, 358 (2017) eaam5776.

[3] A. Dhabi., Innovation Outlook: Renewable Methanol, IRENA AND METHANOL INSTITUTE, (2021).

[4] G.A. Olah, Beyond Oil and Gas: The Methanol Economy, Angew. Chem. Int. Ed., 44 (2005) 2636-2639.

[5] X. Jiang, X. Nie, X. Guo, C. Song, J.G. Chen, Recent Advances in Carbon Dioxide Hydrogenation to Methanol via Heterogeneous Catalysis, Chem. Rev., 120 (2020) 7984-8034.

[6] N. Podrojková, V. Sans, A. Oriňak, R. Oriňaková, Recent Developments in the Modelling of Heterogeneous Catalysts for $CO_2$ Conversion to Chemicals, ChemCatChem, 12 (2020) 1802-1825.

[7] J.W. Ager, A.A. Lapkin, Chemical storage of renewable energy, Science, 360 (2018) 707.

[8] M. Behrens, F. Studt, I. Kasatkin, S. Kühl, M. Hävecker, F. Abild-Pedersen, S. Zander, F. Girgsdies, P. Kurr, B.-L. Kniep, M. Tovar, R.W. Fischer, J.K. Nørskov, R. Schlögl, The Active Site of Methanol Synthesis over $Cu/ZnO/Al_2O_3$ Industrial Catalysts, Science, 336 (2012) 893-897.

[9] J. Graciani, K. Mudiyanselage, F. Xu, A.E. Baber, J. Evans, S.D. Senanayake, D.J. Stacchiola, P. Liu, J. Hrbek, J. Fernandez Sanz, J.A. Rodriguez, Highly active copper-ceria and copper-ceria-titania catalysts for methanol synthesis from $CO_2$, Science, 345 (2014) 546-550.

[10] G. Bozzano, F. Manenti, Efficient methanol synthesis: Perspectives, technologies and optimization strategies, Prog. Energy Combust. Sci., 56 (2016) 71-105.

[11] A. García-Trenco, A. Regoutz, E.R. White, D.J. Payne, M.S.P. Shaffer, C.K. Williams, PdIn intermetallic nanoparticles for the Hydrogenation of $CO_2$ to Methanol, Applied Catalysis B: Environmental, 220 (2018) 9-18.

[12] L. Wang, E. Guan, Y. Wang, L. Wang, Z. Gong, Y. Cui, X. Meng, B.C. Gates, F.S. Xiao, Silica accelerates the selective hydrogenation of $CO_2$ to methanol on cobalt catalysts, Nat Commun, 11 (2020) 1033.

[13] J. Zhong, X. Yang, Z. Wu, B. Liang, Y. Huang, T. Zhang, State of the art and perspectives in heterogeneous catalysis of $CO_2$ hydrogenation to methanol, Chem. Soc. Rev., 49 (2020) 1385-1413.

[14] A. George, B. Shen, M. Craven, Y. Wang, D. Kang, C. Wu, X. Tu, A Review of Non-Thermal Plasma Technology: A novel solution for $CO_2$ conversion and utilization, Renewable and Sustainable Energy Reviews, 135 (2021) 109702.

[15] M. Ghoussoub, M. Xia, P.N. Duchesne, D. Segal, G. Ozin, Principles of photothermal gas-phase heterogeneous $CO_2$ catalysis, Energy & Environmental Science, 12 (2019) 1122-1142.

[16] C. Xu, J. Hong, P. Sui, M. Zhu, Y. Zhang, J.-L. Luo, Standalone Solar Carbon-Based Fuel Production Based on Semiconductors, Cell Reports Physical Science, 1 (2020) 100101.

[17] Z.J. Wang, H. Song, H. Liu, J. Ye, Coupling of Solar Energy and Thermal Energy for Carbon Dioxide Reduction: Status and Prospects, Angew. Chem. Int. Ed. Engl., 59 (2020) 8016-8035.

[18] B. Deng, H. Song, K. Peng, Q. Li, J. Ye, Metal-organic framework-derived Ga-Cu/$CeO_2$ catalyst for highly efficient photothermal catalytic $CO_2$ reduction, Applied Catalysis B: Environmental, 298 (2021) 120519.

[19] H. Song, X. Meng, Z.-j. Wang, Z. Wang, H. Chen, Y. Weng, F. Ichihara, M. Oshikiri, T. Kako, J. Ye, Visible-Light-Mediated Methane Activation for Steam Methane Reforming under Mild Conditions: A Case Study of Rh/$TiO_2$ Catalysts, ACS Catalysis, 8 (2018) 7556-7565.

[20] C. Xu, X. Zhang, M.-N. Zhu, L. Zhang, P.-F. Sui, R. Feng, Y. Zhang, J.-L. Luo, Accelerating photoelectric $CO_2$ conversion with a photothermal wavelength-dependent plasmonic local field, Applied Catalysis B: Environmental, 298 (2021) 120533.

[21] X. Zhang, H. Liu, Y. Wang, S. Yang, Q. Chen, Z. Zhao, Y. Yang, Q. Kuang, Z. Xie, Hot-electron-induced $CO_2$ hydrogenation on Au@AuRu/g-$C_3N_4$ plasmonic bimetal–semiconductor heterostructure, Chem. Eng. J., 443 (2022) 136482.

[22] H. Song, X. Meng, T.D. Dao, W. Zhou, H. Liu, L. Shi, H. Zhang, T. Nagao, T. Kako, J. Ye, Light-Enhanced Carbon Dioxide Activation and Conversion by Effective Plasmonic Coupling Effect of Pt and Au Nanoparticles, ACS Appl Mater Interfaces, 10 (2018) 408-416.

[23] H. Robatjazi, H. Zhao, D.F. Swearer, N.J. Hogan, L. Zhou, A. Alabastri, M.J. McClain, P. Nordlander, N.J. Halas, Plasmon-induced selective carbon dioxide conversion on earth-abundant aluminum-cuprous oxide antenna-reactor nanoparticles, Nature Communications, 8 (2017) 27.

[24] G. Fu, M. Jiang, J. Liu, K. Zhang, Y. Hu, Y. Xiong, A. Tao, Z. Tie, Z. Jin, Rh/Al Nanoantenna Photothermal Catalyst for Wide-Spectrum Solar-Driven $CO_2$ Methanation with Nearly 100% Selectivity, Nano Lett., 21 (2021) 8824-8830.

[25] A.A. Tountas, G.A. Ozin, M.M. Sain, Solar methanol energy storage, Nature Catalysis, 4 (2021) 934-942.

[26] J. Hong, C. Xu, B. Deng, Y. Gao, X. Zhu, X. Zhang, Y. Zhang, Photothermal Chemistry Based on Solar Energy: From Synergistic Effects to Practical Applications, Adv Sci (Weinh), 9 (2022) e2103926.

[27] L. Wang, M. Ghoussoub, H. Wang, Y. Shao, W. Sun, A.A. Tountas, T.E. Wood, H. Li, J.Y.Y. Loh, Y. Dong, M. Xia, Y. Li, S. Wang, J. Jia, C. Qiu, C. Qian, N.P. Kherani, L. He, X. Zhang, G.A. Ozin, Photocatalytic Hydrogenation of Carbon Dioxide with High Selectivity to Methanol at Atmospheric Pressure, Joule, 2 (2018) 1369-1381.

[28] T. Yan, N. Li, L. Wang, W. Ran, P.N. Duchesne, L. Wan, N.T. Nguyen, L. Wang, M. Xia, G.A. Ozin, Bismuth atom tailoring of indium oxide surface frustrated Lewis pairs boosts heterogeneous $CO_2$ photocatalytic hydrogenation, Nat Commun, 11 (2020) 6095.

[29] Y. Zhao, X. Jia, G.I.N. Waterhouse, L.-Z. Wu, C.-H. Tung, D. O'Hare, T. Zhang, Layered Double Hydroxide Nanostructured Photocatalysts for Renewable Energy Production, Advanced Energy Materials, 6 (2016) 1501974.

[30] Z. Zhang, C. Mao, D.M. Meira, P.N. Duchesne, A.A. Tountas, Z. Li, C. Qiu, S. Tang, R. Song, X. Ding, J. Sun, J. Yu, J.Y. Howe, W. Tu, L. Wang, G.A. Ozin, New black indium oxide-tandem photothermal $CO_2$-$H_2$ methanol selective catalyst, Nat Commun, 13 (2022) 1512.

[31] J. Zhu, F. Cannizzaro, L. Liu, H. Zhang, N. Kosinov, I.A.W. Filot, J. Rabeah, A. Bruckner, E.J.M. Hensen, Ni-In Synergy in $CO_2$ Hydrogenation to Methanol, ACS Catal, 11 (2021) 11371-11384.

[32] P. Chang, Y. Wang, Y. Wang, Y. Zhu, Current trends on $In_2O_3$ based heterojunction photocatalytic systems in photocatalytic application, Chem. Eng. J., 450 (2022) 137804.

[33] Y. Qi, L. Song, S. Ouyang, X. Liang, S. Ning, Q. Zhang, J. Ye, Photoinduced Defect Engineering: Enhanced Photothermal Catalytic Performance of 2D Black $In_2O_{3-x}$ Nanosheets with Bifunctional Oxygen Vacancies, Adv. Mater., 32 (2020) e1903915.

[34] L. Wang, Y. Dong, T. Yan, Z. Hu, A.A. Jelle, D.M. Meira, P.N. Duchesne, J.Y.Y. Loh, C. Qiu, E.E. Storey, Y. Xu, W. Sun, M. Ghoussoub, N.P. Kherani, A.S. Helmy, G.A. Ozin, Black indium oxide a photothermal $CO_2$ hydrogenation catalyst, Nat Commun, 11 (2020) 2432.

[35] W. Wei, Z. Wei, R. Li, Z. Li, R. Shi, S. Ouyang, Y. Qi, D.L. Philips, H. Yuan, Subsurface oxygen defects electronically interacting with active sites on $In_2O_3$ for enhanced photothermocatalytic $CO_2$ reduction, Nat Commun, 13 (2022) 3199.

[36] A. Bavykina, I. Yarulina, A.J. Al Abdulghani, L. Gevers, M.N. Hedhili, X. Miao, A.R. Galilea, A. Pustovarenko, A. Dikhtiarenko, A. Cadiau, A. Aguilar-Tapia, J.-L. Hazemann, S.M. Kozlov, S. Oud-Chikh, L. Cavallo, J. Gascon, Turning a Methanation Co Catalyst into an In–Co Methanol Producer, ACS Catalysis, 9 (2019) 6910-6918.

[37] Z. Cai, J. Dai, W. Li, K.B. Tan, Z. Huang, G. Zhan, J. Huang, Q. Li, Pd Supported on MIL-68(In)-Derived $In_2O_3$ Nanotubes as Superior Catalysts to Boost $CO_2$ Hydrogenation to Methanol, ACS Catalysis, 10 (2020) 13275-13289.

[38] M.M. Li, H. Zou, J. Zheng, T.S. Wu, T.S. Chan, Y.L. Soo, X.P. Wu, X.Q. Gong, T. Chen, K. Roy, G. Held, S.C.E. Tsang, Methanol Synthesis at a Wide Range of $H_2/CO_2$ Ratios over a Rh-In Bimetallic Catalyst, Angew. Chem. Int. Ed. Engl., 59 (2020) 16039-16046.

[39] K. Sun, N. Rui, Z. Zhang, Z. Sun, Q. Ge, C.-J. Liu, A highly active $Pt/In_2O_3$ catalyst for $CO_2$ hydrogenation to methanol with enhanced stability, Green Chemistry, 22 (2020) 5059-5066.

[40] J. Zhao, M. Zheng, X. Lai, H. Lu, N. Li, Z. Ling, J. Cao, Preparation of mesoporous $In_2O_3$ nanorods via a hydrothermal-annealing method and their gas sensing properties, Mater. Lett., 75 (2012) 126-129.

[41] J. Wang, K. Sun, X. Jia, C.-j. Liu, $CO_2$ hydrogenation to methanol over $Rh/In_2O_3$ catalyst, Catal. Today, 365 (2021) 341-347.

[42] N. Rui, F. Zhang, K. Sun, Z. Liu, W. Xu, E. Stavitski, S.D. Senanayake, J.A. Rodriguez, C.-J. Liu, Hydrogenation of $CO_2$ to Methanol on a $Au^{\delta+}$–$In_2O_{3-x}$ Catalyst, ACS Catalysis, 10 (2020) 11307-11317.

[43] L. Wan, Q. Zhou, X. Wang, T.E. Wood, L. Wang, P.N. Duchesne, J. Guo, X. Yan, M. Xia, Y.F. Li, A.A. Jelle, U. Ulmer, J. Jia, T. Li, W. Sun, G.A. Ozin, $Cu_2O$ nanocubes with mixed oxidation-state facets for (photo)catalytic hydrogenation of carbon dioxide, Nature Catalysis, 2 (2019) 889-898.

[44] J. Balcerzak, W. Redzynia, J. Tyczkowski, In-situ XPS analysis of oxidized and reduced plasma deposited ruthenium-based thin catalytic films, Appl. Surf. Sci., 426 (2017) 852-855.

[45] S. López-Rodríguez, A. Davó-Quiñonero, E. Bailón-García, D. Lozano-Castelló, F.C. Herrera, E. Pellegrin, C. Escudero, M. García-Melchor, A. Bueno-López, Elucidating the Role of the Metal Catalyst and Oxide Support in the $Ru/CeO_2$-Catalyzed $CO_2$ Methanation Mechanism, The Journal of Physical Chemistry C, 125 (2021) 25533-25544.

[46] X. Ye, C. Yang, X. Pan, J. Ma, Y. Zhang, Y. Ren, X. Liu, L. Li, Y. Huang, Highly Selective Hydrogenation of $CO_2$ to Ethanol via Designed Bifunctional $Ir_1$-$In_2O_3$ Single-Atom Catalyst, J. Am. Chem. Soc., 142 (2020) 19001-19005.

[47] T.R. Garrick, W. Diao, J.M. Tengco, E.A. Stach, S.D. Senanayake, D.A. Chen, J.R. Monnier, J.W. Weidner, The Effect of the Surface Composition of Ru-Pt Bimetallic Catalysts for Methanol Oxidation, Electrochim. Acta, 195 (2016) 106-111.

[48] K. Shun, K. Mori, S. Masuda, N. Hashimoto, Y. Hinuma, H. Kobayashi, H. Yamashita, Revealing hydrogen spillover pathways in reducible metal oxides, Chemical Science, 13 (2022) 8137-8147.

[49] C. Shen, K. Sun, Z. Zhang, N. Rui, X. Jia, D. Mei, C.-j. Liu, Highly Active Ir/$In_2O_3$ Catalysts for Selective Hydrogenation of $CO_2$ to Methanol: Experimental and Theoretical Studies, ACS Catalysis, 11 (2021) 4036-4046.

[50] A. Baszczuk, M. Jasiorski, M. Nyk, J. Hanuza, M. Mączka, W. Stręk, Luminescence properties of europium activated $SrIn_2O_4$, Journal of Alloys and Compounds, 394 (2005) 88–92.

[51] Z.-j. Wang, H. Song, H. Pang, Y. Ning, T.D. Dao, Z. Wang, H. Chen, Y. Weng, Q. Fu, T. Nagao, Y. Fang, J. Ye, Photo-assisted methanol synthesis via $CO_2$ reduction under ambient pressure over plasmonic Cu/ZnO catalysts, Applied Catalysis B: Environmental, 250 (2019) 10-16.

[52] J. Díez-Ramírez, J.A. Díaz, P. Sánchez, F. Dorado, Optimization of the Pd/Cu ratio in Pd-Cu-Zn/SiC catalysts for the $CO_2$ hydrogenation to methanol at atmospheric pressure, Journal of $CO_2$ Utilization, 22 (2017) 71-80.

[53] M.L. Brongersma, N.J. Halas, P. Nordlander, Plasmon-induced hot carrier science and technology, Nat Nanotechnol, 10 (2015) 25-34.

[54] U. Aslam, V.G. Rao, S. Chavez, S. Linic, Catalytic conversion of solar to chemical energy on plasmonic metal nanostructures, Nature Catalysis, 1 (2018) 656-665.

[55] A. Politano, I. Radović, D. Borka, Z.L. Mišković, G. Chiarello, Interband plasmons in supported graphene on metal substrates: Theory and experiments, Carbon, 96 (2016) 91-97.

[56] N.C. Nelson, M.-T. Nguyen, V.-A. Glezakou, R. Rousseau, J. Szanyi, Carboxyl intermediate formation via an in situ-generated metastable active site during water-gas shift catalysis, Nature Catalysis, 2 (2019) 916-924.

[57] B. Moore, S.Y. Toh, Y.T.A. Wong, T. Bashiri, A. McKinnon, Y. Wai, K.W. Alethea Lee, P. Ovchinnikov, C.Y. Chiang, P. Djuricanin, T. Momose, Hydrocarboxyl Radical as a Product of alpha-Alanine Ultraviolet Photolysis, J Phys Chem Lett, 12 (2021) 11992-11997.

[58] D. Forney, M.E. Jacox, W.E. Thompson, Infrared spectra of trans-HOCO, $HCOOH^+$, and $HCO_2^-$ trapped in solid neon, The Journal of Chemical Physics, 119 (2003) 10814-10823.

[59] L.O. Paulson, F.M. Mutunga, S.E. Follett, D.T. Anderson, Reactions of atomic hydrogen with formic acid and carbon monoxide in solid parahydrogen I: Anomalous effect of temperature, J. Phys. Chem. A, 118 (2014) 7640-7652.

# Chapter 5 General Conclusion and Future Prospects

## 5.1 General conclusion

In this thesis, the main object is to develop nanometals/oxides catalysts for highly efficient and long-term stable photothermal catalytic $CO_2$ hydrogenation to CO via RWGS reaction at mild conditions by coupling light-to-heat effect and photo-induced hot carrier-mediated activation of reactants, as well as selectively generating highly value-added solar methanol under ambient pressure. The detailed study could be concluded in the following parts.

1. Metal-organic framework-derived Ga-Cu/$CeO_2$ catalyst for highly efficient photothermal catalytic $CO_2$ reduction

Ga-Cu/$CeO_2$ catalyst is synthesized by direct pyrolysis of the Ga and Cu-containing Ce-metal-organic frameworks for efficient photothermal catalytic $CO_2$ hydrogenation. Because of the highly dispersed Ga and Cu species in $CeO_2$, the optimized catalyst 10Cu5Ga/$CeO_2$ (10 wt% Cu and 5 wt% Ga) achieves a CO production rate of 111.2 $mmol \cdot g^{-1} \cdot h^{-1}$ with nearly 100% selectivity under full solar spectrum irradiation, which is superior to most reported Cu and other earth-abundant metals-based photothermal catalysts. Mechanism study demonstrates that the synergy of solar heating and light promotion reduces the apparent activation energy and contributes to the dramatically increased CO production. The introduction of Ga promotes the generation of oxygen vacancies on $CeO_2$ surface and increases the interaction between Cu and $CeO_2$, thus enhances $CO_2$ adsorption on catalyst surface and bidentate formate intermediates formation. The irradiation could facilitate the decomposition of formate species into carbonyl and finally into CO as product.

2. Metal oxide-modified Cu/MgO-$Al_2O_3$ catalyst for efficient and stable photothermal catalytic $CO_2$ conversion

In this part, I utilize a facile strategy to synthesize a series of metal oxide modified Cu/MgO-$Al_2O_3$ photothermal catalysts derived from the calcination of CuMgAl-LDH followed by impregnation of metal nitrate. Due to the highly dispersed Cu and stabilization by the addition of metal oxide ($ZrO_2$), the catalysts show not only highly efficient activity of CO production (125.7 mmol·$g^{-1}$·$h^{-1}$ under 1.88 W·$cm^{-2}$ irradiation), but also a long-term stability during the photothermal catalytic RWGS reaction. After 8 h reaction, the activity is almost stable, and still remains 93% after 12 h continuous reaction process on the optimized catalyst $Cu_{0.6}$@Zr/MA, while only 80% of activity left after 6.5 h on the catalyst without $ZrO_2$. Detailed study demonstrates that the addition of metal oxide stabilizes the architecture of Cu nanoparticles and prevents the aggregation of active Cu in rough conditions, such as high temperature and wet atmosphere, thus preserving the active sites of catalysts during the reaction process. The mechanism investigation indicates that the reaction pathway is not changed by the introduction of $ZrO_2$, and the light-induced hot carriers facilitated the decomposition of formate intermediates to final product CO.

3. Photothermal catalytic $CO_2$ hydrogenation to methanol over Ru/$In_2O_3$ catalysts under atmospheric pressure

In this part, solar methanol is effectively generated from the photothermal $CO_2$ hydrogenation process over Ru/$In_2O_3$ catalyst with a yield of 280.4 μmol $g^{-1}$ $h^{-1}$ under 1413 mW $cm^{-2}$ irradiation without additional thermal energy input, much higher than the reported works at ambient pressure. Mechanism studies demonstrate that the introduction of Ru promotes the formation of oxygen vacancies in $In_2O_3$ and the interaction between Ru and oxygen vacancies on $In_2O_3$ enhances the activation and conversion of $CO_2$ and $H_2$ on the catalyst surface. Detailed investigations illustrate that the synergy of photothermal heating and light-induced hot carriers on Ru nanoparticles contributes to the effective solar methanol production. DFT calculations further elaborate that Ru promotes the activation of $CO_2$ and $H_2$ to form intermediate *CO via *COOH, and oxygen vacancies on $In_2O_3$ surface favor the consequent hydrogenation process to form methanol.

## 5.2 Future prospects

Although some progresses have been made in photothermal catalytic $CO_2$ hydrogenation to valuable fuels and chemicals over nanometals/oxides composites, there are still multiple challenges for the development of efficient and stable catalysts for $CO_2$ conversion with desired selectivity towards valuable products, as well as the investigation of reaction mechanism of photo-enhancement on the activation and conversion of reactants. As listed are some important issues demanding special attention and further study:

First, the efficiency and long-term stability of photothermal catalysts are important aspects to be investigated for practical applications. (1) Most of the reported works are conducted with a relatively low $CO_2$ conversion (< 10%), which is far from the requirement for large-scale application. (2) Additionally, most durability evaluations in the reported works are carried out within two days, and the consequent studies about deactivation are generally insufficient. In order to push forward the photothermal catalytic $CO_2$ hydrogenation process towards industrial application, it is necessary to modify the catalysts and optimize the systems and reaction conditions to inhibit the deactivation of the catalysts, possibly resulted by the collapse, sintering, reduction of active sites, and carbon deposition during the reaction process. Furthermore, conducting in situ and in operando test studies is essential to systematically elucidate the reaction mechanisms of various photothermal $CO_2$ reduction processes. This will aid in identifying the source of deactivation and developing design strategies for actively regenerating catalysts.

Second, the selectivity of photothermal catalytic $CO_2$ hydrogenation still needs to be improved. At current stage, the dominate products from photothermal $CO_2$ reduction in research works are $CH_4$ and CO. It will be more appealing if we could obtain more value-added products from direct $CO_2$ hydrogenation process, such as methanol, ethanol, and hydrocarbons. Although several works have shown that feasibility of such perspectives, in which alcohols and $C_{2+}$ hydrocarbons are produced in the photothermal

$CO_2$ reduction systems, there is still a significant disparity between the current progress and the actual demand. The regulation of selectivity towards desired products in photothermal $CO_2$ hydrogenation process remains a great challenge for the future research on the coupling of light-to-heat conversion and photo-induced hot carrier-mediated activation of reactants. In order to develop photothermal catalytic $CO_2$ reduction systems that can produce value-added chemicals with adjustable selectivity, more works should be devoted to on the design of highly efficient catalysts, the optimization of reaction conditions (including temperature, light intensity, reaction pressure/time, $CO_2/H_2$ ratio) and the improvement of reaction devices.

Finally, at current stage, the chemical and physical mechanisms of photothermal catalytic $CO_2$ hydrogenation process still remain to be further explored. The synergetic effect of photo-heating and photo-induced hot carrier-mediated activation of reactants has been proposed and widely accepted, but some following critical issues should be carefully addressed to thoroughly comprehend the mechanism of the complicated photothermal catalysis. (1) The detailed mechanism of hot carrier activation demands further investigation, due to the ultrafast process of the transfer or dissipation of hot electrons (usually < 100 ps). In order to understand the process of hot carrier activation, some advanced technologies, such as in situ transient surface analysis, are expected to help the research on the activation process of reactants on the plasmonic nanostructures. (2) The contribution of photo-heating effect and photo-induced hot carrier effect should be distinguished clearly. To this end, the localized monitor of nanoscale temperatures and transient intermediate species of catalysts is in demand to clarify the thermal and non-thermal effect in the photothermal catalysis.

# Acknowledgement

First of all, I would like to express my sincere gratitude to my supervisor Prof. Jinhua Ye for her continuous support and valuable suggestions both in my Ph.D. study and in my personal life. Thank you for giving me the opportunity to conduct my Ph.D. study at Hokkaido University. Your academic insights and great passions will benefit me through my whole life. It is my great pleasure and honor to study and conduct research work under the supervision of Prof. Ye.

I am also grateful to my sub-supervisors, Prof. Naoto Shirahata and Prof. Naoto Tsubouchi. Thank you for your suggestions and kind help during mu Ph.D. study. Many thanks to Prof. Kei Murakoshi and Prof. Hidenori Noguchi for their valuable comments and suggestions on my thesis and presentation.

Thirdly, I would like to thank Dr. Hui Song, who helped me a lot in my research. He gave me useful opinions and suggestions in my research work. I also want to thank all the members in the Photocatalytic Materials Group in NIMS and the persons who have helped me. I would like to express my thanks to Dr. Shunqin Luo, Dr. Xiaohui Ren, Mr. Qi Wang, Dr. Gaoliang Yang, Dr. Sijie Li, Mr. Davin Philo, Dr. Yunxiang Li, Dr. Li Shi, Dr. Shuang Song, Dr. Huiwen Lin, Dr. Kang Peng, Dr. Hong Pang, Dr. Fumihiko Ichihara, Dr. Xusheng Wang, Dr. Lan Li, Dr. Yu He, Dr. Yiming Zhang, Dr. Ningdong Feng, Dr. Dekang Huang, Dr. Hengming Huang, Dr. Minmin Han, Dr. Mengli Li, Dr. Yao Xie, Dr. Xuelian Yu, Dr. Shengyao Wang, Dr. Tetsuya Kako, and Dr. Mitsutake Oshikiri for their kind helps in both experiments and daily life. I want to thank our secretaries Ms. Kanae Hasegawa and Ms. Haruna Kurokawa, who helped me a lot in my daily life.

At last, I would like to express my deepest gratitude to my parents and other family members. Your selfish love and guidance are my lifelong treasure. Thank you for your continuous support and understanding all the time.